MINIATURIZED ULTRA-WIDEBAND UAV RADARS AND ANTENNAS FOR REMOTE SENSING APPLICATIONS

by

FERAS ABUSHAKRA

NATHAN JEONG, COMMITTEE CHAIR
PRASAD GOGINENI, COMMITTEE CO-CHAIR
DREW TAYLOR
MARGARET KIM
SAMEER MULANI

A DISSERTATION

Submitted in partial fulfillment of the requirements
for the degree of Doctor of Philosophy
in the Department of Electrical and Computer Engineering
in the Graduate School of
The University of Alabama

TUSCALOOSA, ALABAMA

2023

ABSTRACT

In the last few years, ultra-wideband (UWB) radars have shown great potential for remote sensing of the earth, such as measuring snow thickness, soil moisture, and the bathymetry of rivers. Unmanned Aerial Vehicles (UAVs) are an attractive alternative to manned aircraft due to their low cost and flexibility in installation and operation of ultra-wideband radars. The development of drone-based radar systems for remote sensing has been a topic of significant research over the last few years.

Ultra-wideband Frequency Modulated Continuous Wave (FMCW) radars are developed in this dissertation for fine-resolution snow and soil moisture measurements. The mm-wave transmitted signal is down-converted from 77-81 GHz into 2-6 GHz and the received signal is up-converted back to the mm-wave range for digitization and processing. This approach enabled us to develop a very lightweight (<1.5 kg) and compact UWB microwave radar. The radar can be operated up to 100 m altitude for estimated flight time of more than 25 minutes in Tuscaloosa, AL to scan wide areas. The proposed radar has two different versions. The first version used a radar transmitter and receiver chains with waveguide components. This design weighs 5.5 lb (2.5 kg) while the second version is developed with printed circuit board (PCB) up-down converters to reduce the weight and size by approximately 40%. In addition, different antenna arrays are designed to support the radar.

The UWB radars including the antenna arrays are tested in the lab and anechoic chamber. Also, the whole system was operated in the field at different altitudes, wind speeds, and weather conditions to measure soil moisture and snow depth in 2021, 2022, and 2023. The antenna arrays

were steered with certain angles and mounted to collect data at nadir and off-nadir-incidence angles. Both focused and unfocused Synthetic Radar Aperture (SAR) processors are used to process the collected raw data from the radar system. A snow thickness map is generated for the flight area in Colorado using an automated snow tracker. The radar results and in-situ measurements are compared and they are in good agreement.

ACKNOWLEDGEMENTS

I would like to thank my advisor Dr. Nathan Jeong for his guidance, suggestions, and encouragement during my Ph.D. studies and for giving me the chance to work on multiple projects with my colleagues in the Advanced Antenna and Sensors Lab (A2SL) to improve my research skills.

I would like also to thank Prof. Prasad Gogineni for his guidance, suggestions, and support during my Ph.D. including building the radar systems, signal processing, and antenna designs. Prof. Gogineni has a significant contribution in extending my research areas and improving my technical writing during my work at the Remote Sensing Center (RSC) at the University of Alabama.

I would like to thank my dissertation committee Dr. Drew Taylor, Dr. Sameer Mulani, and Dr. Margaret Kim for giving me nice advice on my proposal and final dissertation. I would also like to thank all the faculty, staff, and students at the RSC at the University of Alabama for their valuable help in my research. This dissertation is a result of teamwork and collaboration.

I also want to thank Dr. David Brateen from Kansas University for his valuable help in the In-situ measurements of snow in Colorado-2022 and 2023.

Finally, I want to thank my family for their support during my Ph.D. study and my entire life.

LIST OF ABBREVIATIONS AND SYMBOLS

AVA Antipodal Vivaldi Antenna

BAVA Balanced Antipodal Vivaldi Antenna

CI Coherent integration

COTS Commercial-Off-The-Shelf

CPWG Coplanar Waveguide

CVA Coplanar Vivaldi Antenna

DDS Direct Digital Synthesizer

DPA Dielectric Patch Antenna

DRA Dielectric Resonator Antenna

EM Electromagnetic Wave

FAA Federal Aviation Administration

F/B Front-to-Back Ratio

FMCW Frequency Modulation Continuous Wave

GPR Ground Penetrating Radar

HFSS High-Frequency Structure Simulator

HPBW Half Power Beam Width

LOS Line-of-Sight

MIMO Multi-Input-Multi-Output

MMIC Monolithic Microwave Integrated Circuit

PCB Printed Circuit Board

PLL Phase-Lock Loop

RDRA Rectangular Dielectric Resonator Antenna

SAR Synthetic Aperture Radar

SLL Side Lobe Level

SNR Signal-to-Noise Ratio

SWE Snow Water Equivalent

sUAV small Unmanned Aerial Vehicle

TE Transverse Electric

TI Texas Instruments

UAV Unmanned Aerial Vehicle

UWB Ultra-Wideband

VCO Voltage Control Oscillator

VNA Vector Network Analyzer

CONTENTS

LIST OF TABLES

LIST OF FIGURES

INTRODUCTION

Water is the main source for supporting all the organisms on the earth. Even though 70% of the earth's surface is covered by water, but only 2.5% of this water is fresh [1]. Most of the freshwater is stored in glaciers in Antarctica, Greenland, or other parts of the world and it is not accessible easily. Also, some of the freshwater is stored as groundwater with slow recharge rates relative to fast discharge rates [2].

The world climate change resulting from global warming requires wise management of the planet's resources. For example, approximately 80% of the agricultural lands in the world suffer moderate to severe soil erosion, while 10% experience mild erosion [2], [3]. In addition, overall warming has directly affected about 36 million square kilometers of snow cover around the globe, rapidly changing snow accumulation and melt patterns.

Extensive winter and early spring snow cover in high-elevation regions, like Grand Mesa, Colorado, is a critical water source (surface and groundwater) once seasonal melting commences [4]. For effective water resource management, it is important to accurately predict the changes in runoff during the seasonal snow melt period, which requires an accurate understanding of the snowpack conditions (mainly snow depth and density) around the start of the snow melt season. Thus, both fine-scale and large-scale measurements of snow are needed.

CHAPTER 1

UAV HISTORY REVIEW AND DISSERTATION STRUCTURE

This chapter details a historical review of UAV history as well as the dissertation structure.

1.1 History of Earth Remote Sensing

Measuring the soil moisture and snow depth can be performed manually. However, it requires a lot of time and labor to cover wide areas. Also, it is very difficult to do these types of measurements in heavily vegetated areas or high elevations. Hence, the need for smart technological solutions to perform such measurements has been highlighted in the last two decades. Theoretically, the radar signal in the microwave region has the capability of penetrating through heavy-vegetation and dry snow reaching to the ground surface. The information obtained from the radar reflected signal, backscatter, can be used to estimate the soil moisture or snow depth as it is varying with different dielectric mediums [5, 6]. Different types of radars installed on platforms have been devolved in the last decades to support earth's resources management as well as other applications. Among these platforms, UAVs have recently received more attention due to their low cost, ease of installation, and capability to reach inaccessible areas by man.

1.2 Background on UAV

The idea of demonstrating unmanned flights was discussed early in the 20th century when Elmer Sperry received the first military contract for an unmanned flight system to develop an aerial torpedo for the US Navy in 1917 [7]. During World War II and the cold war, different countries and agencies were involved in a race to develop these platforms mainly for military

applications. However, in the last decade, the UAV's attractive features involve them heavily in a wide range of civilian applications, ex., road traffic, remote sensing, smart agriculture, and surveillance which have been studied [8]. In addition, UAVs can be used to operate both active as well as passive sensors for detection and monitoring. In 2018, the United State Federal Aviation Administration (FAA) has more than one million registered UAVs in its record [9]. Such huge number of these platforms indicates the growing importance of using them for many purposes. In addition, the expectations indicate that the UAV field will offer more than 100,000 jobs by 2025 [10]. Nevertheless, to control the crowded zones with multiple UAVs, many regulations and restrictions have been made by each country's authorities to avoid any sort of accidents. For example, the FAA requires that the maximum UAV flight height is 122 m (400 ft) above the ground surface [11] which is the case in the United States, while it may reach to 300 m in other countries [12]. Also, the UAV should stay within the line of sight (LOS) with the pilot. Many other restrictions on the weight, flying time, areas, and type of equipment it carries are also established. Among different types of UAVs, the small UAV (sUAV) which has a total payload of 25 kg (55 lb) or less is the most common type used for radar remote sensing applications due to its installation flexibility and cost-effectiveness.

1.3 Motivation and Objectives

Despite a decent amount of literature described different UAV radar systems for different applications, there are still plenty of opportunities that can be used to demonstrate new concepts for UAV radars. This dissertation focuses on the development of the UWB, lightweight and compact sUAV ultra-wideband (UWB) radar with lightweight antenna arrays for remote sensing applications. There are four main objectives in this dissertation:

1- Design a novel UWB radar for UAVs with a weight of less than 1.5 kg. The radar needs to

be a stand-alone system including the digitization, recording units, and power supply.

2- Design a novel UWB antenna arrays with a gain of 12-15 dBi at the lower frequency band with a stable radiation pattern over the entire frequency of interest.

3- Develop signal processing algorithms to process the radar data including a fully focused SAR and chirp non-linearity correction.

4- Map the air-snow and snow-ground interfaces in Grand Mesa, Colorado, and produce high-quality echograms as well as a snow thickness map.

For a UAV radar to effectively measure snow depth or monitor vegetation, three main challenges need to be addressed. First, the overall payload of the system needs to be as low as possible; this is crucial to extend the flight time of the UAV and reduce power consumption. In Fig. 1.1, the flight time of the UAV as a function of the total payload is plotted. The plot does not take into consideration other factors such as temperature, altitude, and wind speed. However, it could be seen that weight is a critical factor to extend the flight time. However, the flight time can be extended for more than 2 hours with a hybrid system being developed at The University of Alabama, while the UWB radar still has to be compact and lightweight.

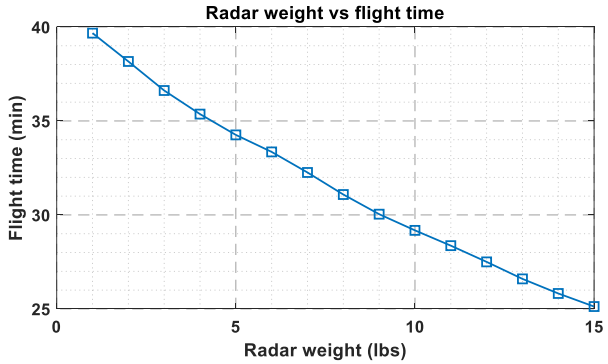

Figure. 1.1 UAV flight time vs. total payload.

Secondly, the maximum flight altitude- called the ambiguous range- should be higher than the natural obstacles in the field. Typically, in heavily-vegetated areas, trees can reach up to

40 m in height. For example, approximately 70 % of Alabama's land area is forested [13] with trees' height varying between 8 to 47 meters [14]. Thus, to secure safe and easy access for the UAV, the radar should have the capability to operate at a sufficient altitude. Finally, the radar range resolution depends on its operating bandwidth [15]. Thus, UWB radars with 20% bandwidth or more are desirable. Recently, the mm-wave frequency range is heavily used for automotive applications. Many manufacturers produced different mm-wave radar evaluation boards with different properties for the frequency ranges of 60-64, 62-69, and 77-81 GHz [16], [17]. These radars are usually used for short ranges due to the high free space loss associated with their small wavelengths. However, they have many attractive features that can be used to develop a compact UWB radar if the free space losses are compensated. Thus, this dissertation describes a novel method to build UWB FMCW radars using a mm-wave evaluation board to obtain a compact, lightweight, and efficient radar for UAV earth remote sensing applications. The proposed radar is supported by its own data capture board and PC unit to record the raw data directly from the mm-wave sensor. The proposed radar aims to operate at a 100-meter altitude and obtain a sufficient signal-to-noise (SNR) ratio.

On the other hand, UAV radars require special types of antennas to accomplish an accurate measurement. The antenna bandwidth needs to cover the radar operating band while the gain value should meet the link budget requirements. Furthermore, the radiation patterns should be symmetric with low side lobe level (SLL) and grating lobes. To cover these requirements, multiple novel antenna designs will be presented in this dissertation. In addition, a comprehensive study of the previous antenna designs will also be presented and compared with the proposed ones. Finally, the raw data will be processed to produce the radar echograms and snow thickness map.

1.4 Proposed Methodology

To fulfill the UAV radar requirements mentioned in the previous section, our approach depends on building a compact FMCW radar system with approximately 3.3 lb (1.5 kg) overall weight. This will be achieved by using a mm-wave automotive radar evaluation board with its data capture board as at these high frequencies these sensors are compact in size with lightweight. Radar operating in the 1-6 GHz frequency range has been shown to be very effective for snow and soil moisture measurements as will be discussed in detail in Chapter 2. Thus, an up and down-conversion systems are developed to down-convert the mm-wave frequency to the microwave region and then up-convert it again to be processed by the data capture board. UWB antenna array designs will be presented for the UWB radar system in Chapter 3. Three different design structures that have impedance bandwidths of 50%, 83%, and 132% will be introduced. The proposed designs achieved a high gain value of 25 dBi. In addition, the 3D geometry antennas are used to reduce the antenna footprint. On the other hand, the proposed Vivaldi antenna array has a total weight of 50 g only for the four-element array. This is achieved by integrating the array's power divider and antennas on a single board.

1.5 Structure of Dissertation

This dissertation details a new approach to build UAV-based radars for remote sensing applications and focuses on snow depth measurements. The dissertation is organized as follows: the introduction of UAV radars and the motivation for the dissertation is discussed in Chapter 1. The Principle of FMCW radar and the development of the two radar generation prototypes are presented in Chapter 2.

Chapter 3 presents different antenna arrays used for UAV radars including the 8×8 DRA array, the Vivaldi antenna array, and the ceramic-based DRA array. A dual-band Ku-band patch

array and a T-shaped Vivaldi antenna configuration for manned aircraft radar are also presented.

Chapter 4 details the signal processing algorithms used to process the radar data and generate the radar echograms and snow maps for snow depth measurements. Chapter 5 describes three field deployments in Tuscaloosa Alabama, and Grand Mesa, Colorado during 2021-2023. The conclusion and suggestions for future work are discussed in Chapter 6.

CHAPTER 2

FMCW RADAR DESIGN AND CHARACTERIZATION

This chapter starts with providing a review of the recent UAV radar applications and the fundamentals of FMCW radar. Then, a description of the technical approach used to develop the UAV radars is presented.

2.1 UAV Radars Literature Review

As the UAV-based UWB radars exhibit great potential for remote sensing applications and provide attractive alternatives to airborne radars, many researchers proposed different radars mounted on UAVs for a wide range of applications. Tan et al. [18] designed a UWB radar that operates at the frequency range of 1-6 GHz using a one-port Vector Network Analyzer (VNA). Their radar output power is 0 dBm and operates at 5-15 m above the surface. An antenna array with dimensions of 360 × 480 × 200 mm^3 mounted on the UAV is used to support radar measurements in Antarctica. A total payload of 3 kg is also reported. Jessen et al. [19] proposed lightweight UAV radar systems for snow depth measurements using a Pseudo noise signal generator to generate a 5.05 GHz bandwidth signal (0.95 to 6) GHz to be used for snow measurements, and the total payload was around 4 kg. The radar is supported by a circularly polarized antenna at the transmitter side with a dual-polarized antenna at the receiver side to improve the SNR. Similarly, Jenssen et al. [20] presented a scheme for measuring snow water equivalent (SWE) using 0.7 to 4.5 GHz UWB signal on a UAV. Also, Wu et al. [21] presented another lightweight ground penetrating radar (GPR) for soil moisture measurements based on a VNA with a total weight of 1.5 kg and a narrow bandwidth of 200 MHz. In addition, Noviello et

al. [22] installed a UWB pulse radar with 1.7 GHz bandwidth on a UAV for radar imaging with a flight height up to 10 m. As can be noticed, all of the above references had a limited flight altitude (range) that varied between 1 and 15 m. This limitation prevents such systems from operating in forested areas.

Lort et al. [23], alternatively, described a UAV radar operating at 100 m altitude and showed a stable ascending velocity for the UAV relative to the nominal track, with a transmitter output power of 30 dBm over a 100 MHz bandwidth. In addition, Prager et al. [24] proposed a 600-2100 MHz frequency range UAV radar for seasonal snow depth measurement in Colorado. It showed that with 1.5 GHz bandwidth, the air-snow and snow-surface interfaces could be detected with 10 dBm of output power over a meadow and forested areas. The radar's total weight is 1.25 kg and can be operated at 60 m altitude. Also, it needs to fly with a UAV speed of 1 m/s to enable measurements with sufficient SNR. In addition, Simpson et al. [25] presented a UWB, FMCW radar that operates at the frequency range of 2 -6 GHz. It is integrated on a UAV for soil moisture measurements and operated at 100 m altitude. The chirp is generated using a direct digital synthesizer (DDS), and voltage control oscillator (VCO) with the phase-lock loop (PLL). The radar has a high linearity output signal. However, with an overall weight of 5 kg, which limited range of operation. On the other hand, LiDARs were used for vegetation measurements on UAVs as they have lightweight and compact sizes [26, 27]. However, due to their short wavelength, snow measurements with LiDARs need two flights to estimate snow thickness, one before and another after snow accumulation.

2.2 Principle of FMCW Radar

Radar in general can be classified into two main classes: continuous wave (CW) and Pulse radars. The CW is transmitting continually a signal, usually without interruption, while the

receiver is continuously receiving the reflected signal from the target. The pulse transmitter, on the other hand, emits a sequence of limited-duration pulses, separated by the off-times. While the transmitter is off, the receiver is on so that target signals can be detected. Continuous wave radars usually use a circulator or a coupler or two antennas to achieve sufficient isolation between the transmitter and receiver. Traditional continuous wave radar has a very limited unambiguous range of half of a wavelength and it cannot determine the target range because it lacks the timing mark necessary to allow the system to time accurately the transmit and receive cycle and to convert this into range. Such a time reference for measuring the distance of stationary objects, but can be generated using frequency modulation of the transmitted signal. In a FMCW radar, the transmitter frequency is changed as a function of time to enable range measurements. The transmitted signal is modulated in frequency as shown in Fig. 2.1 and equation 2.1.

$$f(t) = f_o + B\frac{t}{\tau} \quad \text{where} \quad 0 \le t \le \tau \tag{2.1}$$

Herein, (f_o) is the start frequency, (τ) is chirp duration, and (B) is the transmit signal bandwidth.

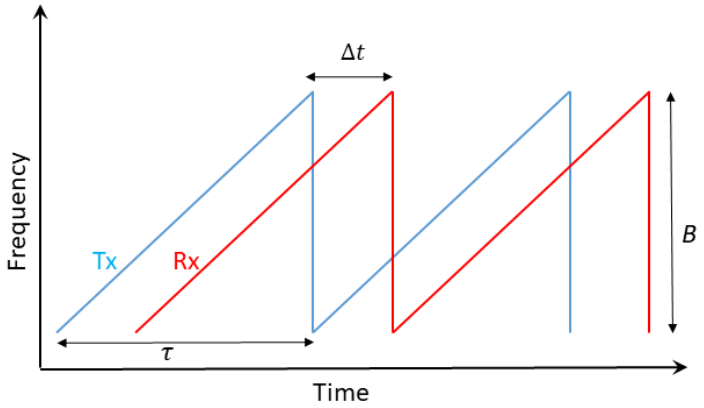

Figure. 2.1. Typical FMCW radar frequency-time plot.

In a FMCW radar, the transmit signal increases or decreases in frequency as a function of time while the received signal is a time-delayed and attenuated replica of the transmit signal

shown in red in Fig. 2.1. The time delay between the transmission and reception can be also converted into a beat frequency, f_b, signal. The time-delay is given by:

$$\Delta t = \frac{2R}{c} \tag{2.2}$$

Where R is the range to the target in meters and c is the velocity of propagation in m/s. The beat frequency depends on the chirp duration, the transmit signal bandwidth, and range (R) as in equation 2.3.

$$f_b = \left(\frac{2R}{c}\right)\left(\frac{B}{\tau}\right) \tag{2.3}$$

Where c is the speed of light in free space. In FMCW radar, time is measuring the differences in frequency between the transmitted and the received signals. The radar range (distance between the radar and target) is then given by.

$$R = \frac{c\Delta t}{2} \tag{2.4}$$

The range resolution (δ_R) is the distance between two adjacent samples in the range direction of the data matrix, and it depends on the propagation speed and the radar bandwidth. For a 4 GHz bandwidth signal, the range resolution is 3.75 cm.

$$\delta_R = \frac{c}{2B} \tag{2.5}$$

2.3 Chirp Generation

In the last few years, the mm-wave frequencies have garnered more attention due to the ability to design compact systems at this high-frequency range. Many radar systems have been reported at these frequencies [28]-[32]. However, the limited capability of penetrating through different objects limited their applications to automotive applications or range detection. On the other hand, the low cost of the mm-wave automotive sensors and the wide operating band of 77-81 GHz offer new solutions for radar development [33]. Fig. 2.2 shows the simplified system

block diagram. A mm-wave radar evaluation board from Texas Instruments (AWR1843) is used to generate the wideband chirp signal [16]. To process the collected data from the mm-wave sensor, a data capture board (DCA1000) is connected to the system. In this dissertation, two different radar prototypes are presented. The first version is a connectorized version while the second one is a PCB version. On the other hand, the main reasons to select the automotive radar evaluation board to generate the chirp for the proposed radar over the traditional PLL and VCOs are:

1- The fast sweep time. The PLL and VCOs have an average sweep time of 1 ms. This result was shown by Simpson et al. [25]. In general, if the sweep time is reduced for the PLL and VCOs, the chirp linearity degrades. Automotive applications require fast chirp to sample Doppler frequency properly at mm-wave frequencies. Basically, most of the automotive radars have a sweep time of 60-200 μs [33], [34]. We have exploited this attribute to develop a system that can operate both slow and fast-moving platforms.

2- Compact size. The compact size of automotive radar boards gives the advantage of building a lightweight radar, as briefly mentioned in the introduction. The described system in this proposal is to demonstrate the concept of using a mm-wave radar chip to develop a compact size and lightweight microwave radar to measure soil moisture and snow measurements.

3- Low power consumption. Typically, the mm-wave board is tested in the labs and it draws 1 A current with a 5 V supply. This is still considered low relative to the PLL and VCOs.

4- The data capture board. This mm-wave automotive radar provides a DSP processor to record data from the sensor. This results in an efficient way to record the data for further processing without using additional digitization hardware. In other radar designs, a wireless Ethernet connection is usually used to transfer the data. However, this can be only used if the flight

altitude is very close to the ground and the data rate is low. If high-altitude flights are needed to cover wide areas, then such approach is not sufficient. However, this is not a major limitation as a very fast, compact, and lightweight digitizer is available now.

5- Novelty. This proposal is proposing and validating a new concept. The use of PLL and VCO was proposed since 2003 and extensively investigated as several airborne systems were developed and successfully flown on many aircraft [35]-[37].

2.3.1 First-Generation Radar Prototype with Connectorized Components

This is a proof-of-concept version of the radar. Herein, E-band waveguide mixers and power divider with WR-12 ports are used to interface the mm-wave sensor. Also, a local oscillator is used to down-convert the mm-wave signal to the desired IF frequency range. After the signal is down-converted, it is amplified, filtered, and supplied to the transmit antenna through a 3-dB attenuator. The attenuator is used to reduce the multiple reflections between the antenna and the next RF component in the chain.

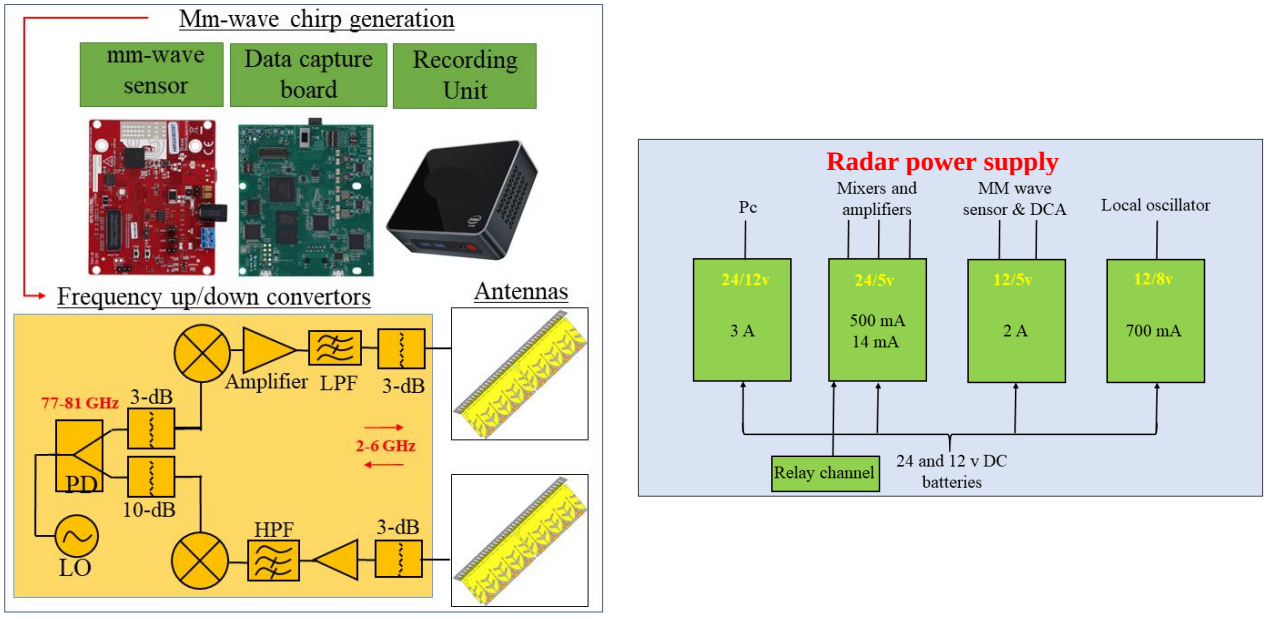

Figure. 2.2 Block diagram of the proposed radar system.

The interface between the mm-wave board and the designed system is performed by cutting the trace of the transmitter and receiver antenna arrays and inserting a 50 Ω coplanar waveguide (CPWG) on top of the evaluation board as illustrated in Fig. 2.3. The connection is then performed using wire bonding and attached on the side of the board to supply the signal to the mixer for down-conversion into the microwave range. There are several reasons for using the E-band waveguide components to build this radar. First, at the mm-wave frequencies, the corresponding physical size of the waveguide is very small. For example, the mixer is 1×2×1 cm^3 with (0.8 oz= 22.7 g) weight only (part no. SFB-12-E2). The heaviest waveguide component in this radar is the LO with (3 oz= 85 g). These weights do not affect the UAV performance, especially the X6 drone that can fly with a total payload of 55 lb.

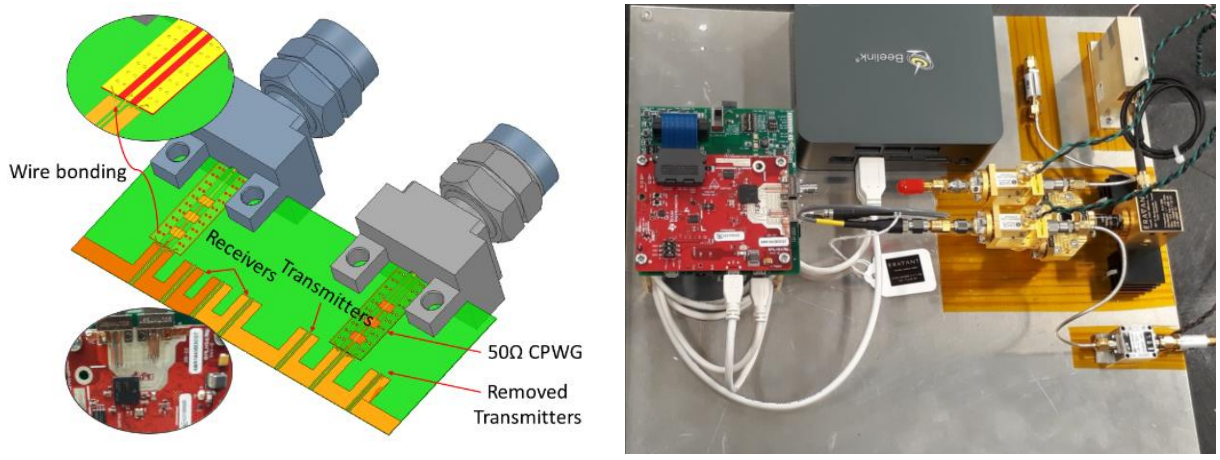

(a) (b)

Figure. 2.3 (a) mm-wave evaluation board with the Tx and Rx interfaces (b) radar prototype and connections.

Secondly, the losses in the mm-wave waveguides are negligible, unlike the other available PCB components. Third, the impedance matching between the waveguide components is better as all of them have WR-12 RF port, which is an efficient port at this high-frequency range. Finally, the waveguide version of the mixer has high IP3 point with high shielding and

isolation. Four different voltages- 3.3, 5, 8, and 12 V- are required to power the electronic components. To prevent the receiver saturation with high received power from short ranges, a relay channel is added to turn on/off the radar amplifiers. The relay channel is connected to a trigger with +3.3 V installed on the UAV and will be activated remotely from the remote controlling unit of the UAV after it reaches 40 m height from the ground level. The radar has its own independent Li-ion batteries (3 and 6 cells) to supply 24 and 12 V. The radar box is shown in Fig. 2.4. The total box dimensions are 35 × 15 × 15 cm^3. The power supply and RF system are housed in a metal box and separated with a metal sheet to mitigate potential interference, as illustrated in Fig. 2.4.

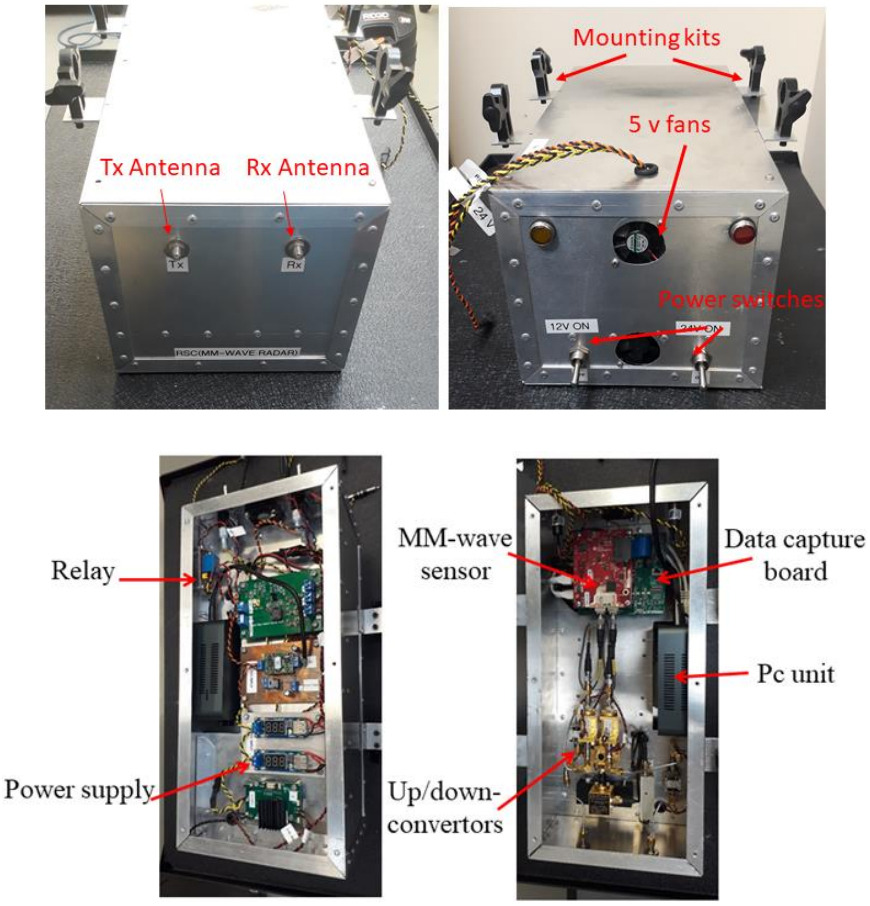

Figure. 2.4 UAV Radar installation in a radar box.

2.3.2 First-Generation Radar Prototype Lab Test

Fig. 2.5 shows the radar chirp characterization results for the frequency range 3.25-5.15 GHz. The 1.9 GHz bandwidth was initially selected as it shows the best linearity performance. The frequency spectrum shows an output power level of 10 dBm over the operating band, as shown in Fig. 2.5(a). The time-domain transmit signal has on and off sweep times of 150 and 5 μs, respectively as illustrated in Fig. 2.5(b). The mm-wave evaluation board has the ability to generate a fast chirp with on-sweep time of 60 μs. However, the selected sweep time was chosen based on the chirp linearity level and to allow for more samples to be included. The integrated radar's overall performance is evaluated using a 100 m optical delay line connected between the transmitter and receiver after adding 62 dB total attenuation (32 dB from the optical delay line and 30 dB external attenuation). This attenuation is equivalent to the free space loss at approximately 100 m distance from the target without considering the antenna's gain. The optical delay line length is 100 m and the shift in the received signal to 107-110 m is due to adding extra cables either at the RF or IF bands during each test. In the FMCW radar, the beat frequency signal obtained a sample of the transmit signal with the received signal (which is accomplished in the mm-wave radar chip) that is directly proportional to the target range. The beat frequency signal from the radar chip is digitized and processed to obtain target range and reflectivity characteristics. The time-domain signal containing beat frequencies proportional to the range is weighted with a Hanning window before Fourier transformation to reduce range sidelobes. The Hanning window degrades the resolution by a factor of approximately 1.4, however, it reduces the sidelobes to -31 dB for the ideal signal instead of -13.5 dB for the rectangular window [38]. The resulting frequency data provide range and reflectivity information and the ideal Hanning window is compared with the radar signal in Fig. 2.5(c). Fig. 2.5(d) shows

the spectrogram of the time domain chirp over the bandwidth. The radar chirp has a low non-linearity, which represents the average of deviation between the spectrogram line and a linear line from the start and end frequencies of the chirp. We have used this configuration in the radar for the 2021 field experiment in the arboretum area, Tuscaloosa, Alabama. These results are also reported in Abushakra et al. [39].

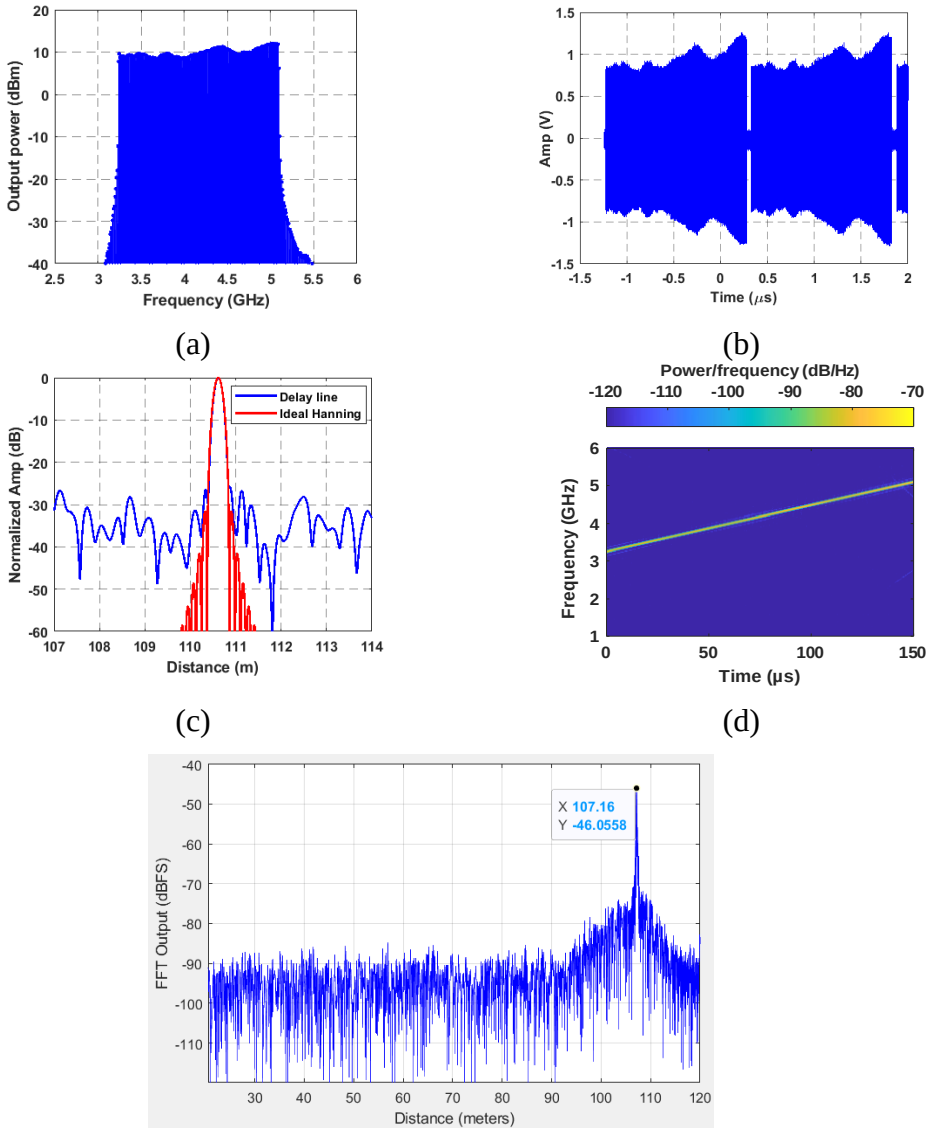

Figure. 2.5 Chirp characterization 3.25-5.15 GHz with 10 dBm output power (a) output chirp frequency spectrum (b) time-domain (c) optical delay line impulse response (d) spectrogram (e) A-scope from TI software interface for the delay line test.

To extend the radar operating band, we customized connectors and cables that can operate up to 90 GHz (1.35 mm) to cover the operating band to the frequency range of 2.8-5.8 GHz, these cables and connectors have also lower losses. This allows us to improve our range resolution and decrease the radar transmit power to 3 dBm to perform successful measurements over snow in Grand Mesa, Colorado during March-April-2022. The chirp duration is increased to 250 μs. Fig. 2.6 shows the radar frequency output signal operating from 2.8 to 5.8 GHz with 3 dBm output power and the A-scope for the 100 m optical delay line attenuated with 62 dB. It could be seen that a SNR of 45-50 dB is achieved. As a tradeoff, the radar output signal linearity got degraded. However, we will discuss how to correct the transmitter non-linearity in the post-processing in Chapter 4.

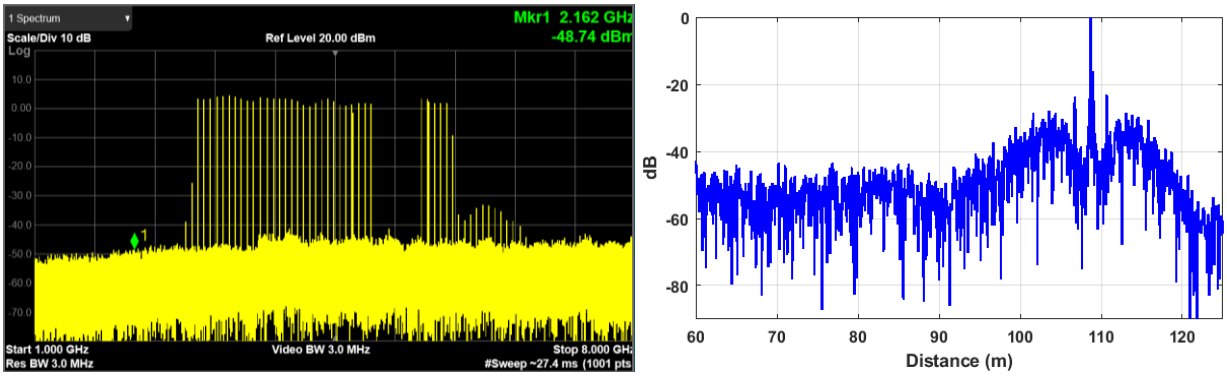

(a) (b)

Figure. 2.6 Chirp characterization 2.8-5.8 GHz with 3 dBm output power (a) output chirp frequency spectrum (b) optical delay line impulse response.

2.3.3 Second-Generation Radar Prototype with PCB Layout

In the second version of the radar, a PCB board interface is added on the top of the awr1843 board as shown in Fig. 2.7. The substrate is RO 3003 with 5 mil thickness and 0.5 oz copper cladding. The interface board has the HMC1058 mixers, power divider, SMA connectors, and local oscillator SMA connector. The mm-wave antennas on top of the TI board were

removed and the new interface board was placed where the traces of the TI board are aligned with the interface board traces. The mixer is wire bonded with 1 and 3 mil ribbon wire gold using a wire bonding machine. This interface allows us to reduce the radar box size to 25 × 18 × 12.5 cm^3 and the weight to 3.3 lb (1.5 kg) to extend the UAV flight time.

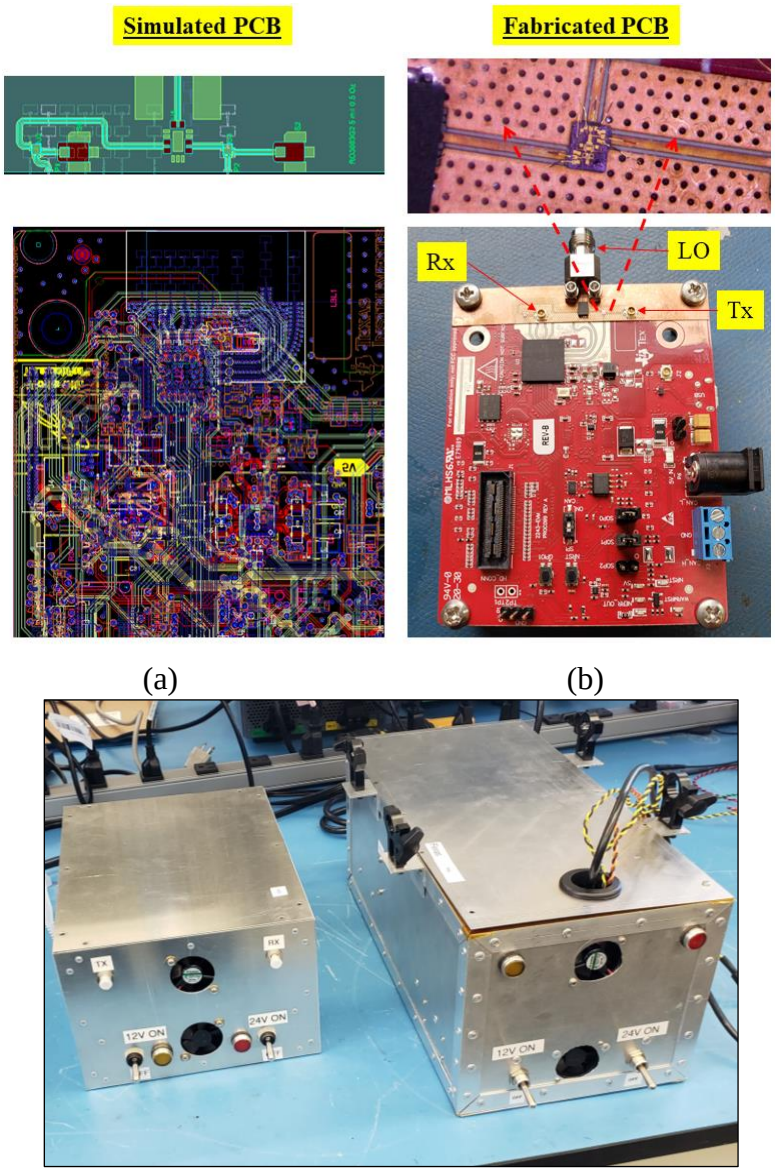

Figure. 2.7 Radar prototype (a) second radar prototype Layout simulation (b) second radar prototype fabrication and installation (c) first and second radar prototype boxes.

2.3.4 Second-Generation Radar Prototype Lab Test

The output signal of the transmitter mixer is amplified and filtered. The output power has a negative slope of 6 dB so we added an equalizer to flatten the output power at 0 dBm. Similar to the first prototype radar, a SNR of 45-50 dB is achieved with a 62 dB total attenuated 30 m cable long we used as a delay line. The second prototype operates using the full 4 GHz bandwidth from 2.2-6.2 GHz with 250 μs chirp duration. The inter-modulation is below 35 dB.

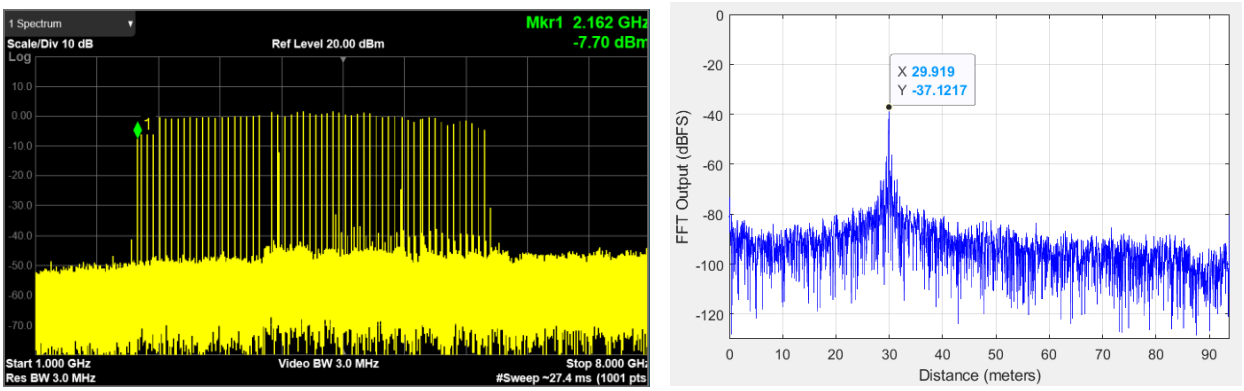

Figure. 2.8 Chirp characterization 2.2-6.2 GHz with 0 dBm output power (a) output chirp frequency spectrum (b) 30 m delay line impulse response.

2.4 Radar Link Budget

For the link budget analysis, two possible scenarios were taken into consideration in our test: the nadir case and the 20^{o} off-nadir case. Assuming that both the transmitter and receiver antennas are identical and the gain (G) of each of them at the center of the operating band is 15-17 dBi. The distance between the antennas is set to be 1.3 m to achieve an isolation of -60 dB within the operating band.

For the nadir case, the received power from a point target at range R is assuming the transmitter and receiver antennas are identical.

$$P_r = \frac{P_t G^2 \lambda^2 \sigma}{(4\pi)^3 R^4} \tag{2.6a}$$

Where P_r is the power received from the target in Watts, σ is the radar cross section in $meter^2$, P_t is the transmitter power in Watts, R is the radar range in meters, G is the antenna gain and λ is the radar wavelength in meters. The equation is modified for a perfect planar reflector as

$$P_r = \frac{P_t G^2 \lambda^2 |\Gamma|^2}{(4\pi)^2 (2R)^2} \tag{2.6b}$$

The signal-to-noise ratio for a planar reflector is given by (2.7) [15] [40]:

$$SNR = \frac{P_t G^2 \lambda^2 |\Gamma|^2}{(4\pi)^2 (2R)^2 KTBN_F} \tag{2.7}$$

where K is Boltzmann constant, T is the temperature in kelvin, B is the IF bin width, Γ is the reflection coefficient, and N_F is the noise figure of the receiver. For a distributed target, the radar equation is modified as:

$$P_r = \frac{P_t G^2 \lambda^2 \sigma^o A}{(4\pi)^3 R^4} \tag{2.8}$$

For a distributed target the radar cross-section is related to the illuminated area, A, and radar-cross-section per unit area as:

$$\sigma = \sigma^o A \tag{2.9}$$

With unfocused Synthetic Aperture Radar (SAR) processing in the along-track direction and pulse-limited case in the range direction, the illuminated area, A, at the incidence angle, θ, can be determined as:

$$A = 0.5\sqrt{R\lambda}\,\frac{c}{2B\sin(\theta)} \tag{2.10}$$

Herein, θ is the incidence angle in radians or degrees. The signal-to-noise for unfocussed SAR is given by:

$$SNR = \frac{P_t G^2 \lambda^2 \sigma^o A}{(4\pi)^3 R^4 K T B N_F} \tag{2.11}$$

Based on the link budget analysis, the transmitted signal is amplified to the range between 3-10 dBm. This power level is sufficient to obtain approximately 45 dB of SNR for the nadir case from the water surface at 100 m altitude. This represents the maximum possible received signal which should be taken into consideration when designing the radar to avoid receiver saturation. Also, the SNR for the off-nadir case from a dry ground surface is about 15 dB. Table 2.1 summarize the link budget for the nadir case.

Table 2.1 The link budget summary for the first-generation radar prototype

Parameter	Value	Unit	Parameter	Value	Unit
Transmit power	10	dBm	$20 \log_{10}(4\pi)$	-21.97	dB
IF bandwidth (B)	1.9	GHz	$20 \log_{10}(2R)$	-46.02	dB
Tx and Rx antennas gain	15	dBi	Receive power	-46	dBm
$20 \log_{10}(\lambda)$	-22.49	dB	-----	----	----

2.5 Radar Design and Implementation on UAV

For the field measurements, the radar system is installed on the Dragon X6 multirotor UAV manufactured by XFold, as shown in Fig. 2.9. The UAV empty payload is 30 lb while the UAV batteries are 10 lb, and the total payload is 55 lb.

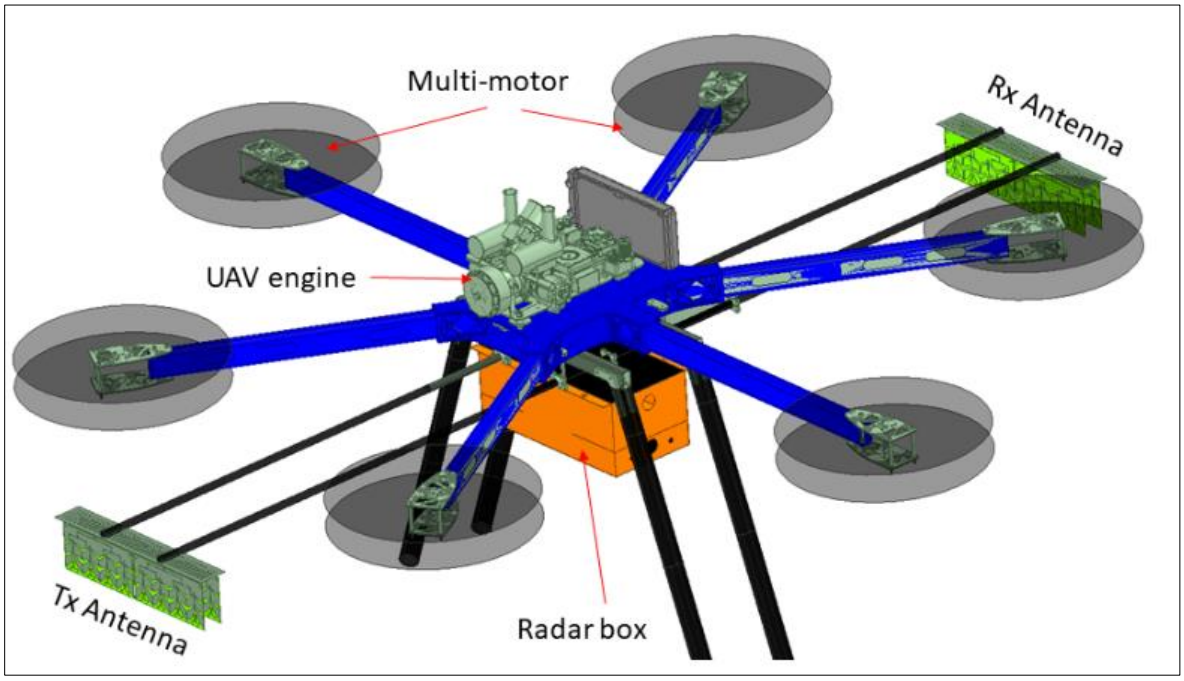

Figure. 2.9 The CAD model for the radar installation on the UAV with the antennas.

The flights are performed autonomously using a wave points navigator. The speed of the UAV is set to be 3 m/s. This speed gives sufficient stability in the flights and allows for more chirps to be averaged coherently as the maximum number of coherently averaged chirps is inversely proportional to the speed [41].

The radar's overall weight is 2.5 kg for the first prototype, while the RF part weighs 850 g only. The radar weight details with all accessories and supporting components for the first prototype are listed below:

1) Small commercial PC running Windows 10: This PC weighted about 770 g, but it is very useful to control and monitor the radar in a very fast way. Also, the automotive board needs to be connected to a PC in the radar box to record the raw data.
2) Custom power supply: The different components of the RF part, fans, and the PC need different voltages and current sources. Thus, we have 4 small PCB boards with different outputs to feed the radar system. The weight of the total power supply is about 250 g.
3) Two fan units with 1-inch diameter for air cooling: As we separated the RF part from the power supply using a metal sheet in the same box, we need to have two fans blowing the air in opposite directions for an efficient cooling system. Each fan weighed 80 g.
4) Radar box: The metal box material is mainly an aluminum sheet with 0.625 mm thickness. Based on the aerodynamic calculations, the selected thickness and supporting rods for the radar box achieved the minimum safety requirements while keeping the weight as low as possible.
5) Four mounting kits: These four mounting kits are used to mount the radar box on the drone. Their total weight is 120 g.
6) Two power switches connected to an LED: These switches are used to control the input power for the radar in the appropriate sequence. The first switch will be connected to the 24 V source. This switch will turn on the PC to start the radar configuration. Then, the second switch will enable the 12 V source to turn on the automotive board. After that, the amplifiers will be turned on by a relay channel installed in the power supply.

With this system, our drone successfully performed many flights with about 25-30 minutes for each flight. For the second radar prototype, the overall weight is 3.3 lb (1.5 kg), where most of the weight reduction is achieved by removing the up/down conversion

components, using the PCB interface board, and a lightweight PC board to operate the TI software and record the data.

Figure. 2.10 The first radar prototype flight test in the field in Tuscaloosa, 2022.

Figure. 2.11 The second radar prototype flight test in the field in Colorado, 2023.

CHAPTER 3

ULTR-WIDEBAND ANTENNA ARRAYS FOR UAV RADARS

The radar sensitivity is proportional to its power-aperture product. Thus, the design and development of an optimized antenna array is a major requirement in developing low-power UWB radars. Optimized antenna arrays are designed, developed, and integrated into the system as a part of this dissertation. The dielectric resonator antenna (DRA) is used as it is one of the preferred candidates for a wideband and high-gain antenna because of its compact size, wide bandwidth, and high efficiency. First, a 64-element rectangular dielectric resonator antenna (RDRA) planar array with (8×8) arrangement is designed and developed. The array provided very good shielding for the large feeding network while keeping a 50% impedance bandwidth with a symmetric radiation pattern and stable gain value over the frequency of interest. The mechanical structure was strong and easy to integrate into UAVs and manned aircraft. The second design is a lightweight ceramic-based RDRA array with 83% impedance bandwidth with a metal back reflector to suppress the back-lobe radiation from the feeder and to install the antenna on the UAV.

Finally, an ultra-wideband improved radiation patterns and high-gain coplanar Vivaldi antenna (CVA) linear array with a 4×1 arrangement is introduced. The E-plane gratings lobes at higher frequencies are suppressed by placing a low-profile DPA (dielectric patch antenna) at the aperture between the two tapered slots. The transverse electric (TE) modes with omnidirectional radiation in the DPA are generated for a wideband frequency range using the surface current of the CVA. The Side Lobe Level (SLL) and grating lobes are suppressed by 5-10 dB over the

operating band, where the distance between the elements over-exceeds the guided wavelength. Furthermore, slots with exponential formulas are created in the array geometry to reduce the mutual coupling.

3.1 UAV Antennas Review and Requirements

The radar transmitter sends the transmit signal as electromagnetic wave (EM) waves through the transmitter antenna. Then, the reflected wave from an object is captured by the receiver antenna. The radar can have two separate antennas in a “bi-static” radar, where the transmitter and receiver have different antennas, or a “mono-static” radar where there is only one antenna for the transmitter and receiver. In this case, a switch is needed to direct the transmit signal from the transmitter to the antenna and the received signal from the antenna to the receiver.

Modern radar systems such as FMCW radars require a broad bandwidth for better range resolution [15]. Thus, the supported antennas for the radar should cover the operating frequency band. Recently, as radars on sUAV have been widely used for a wide range of remote sensing applications, including measuring soil moisture and ice thickness [18-20], designing a suitable antenna for such applications became a more crucial topic. The challenges in designing a UAV radar antenna are that the antenna must have high gain and broad bandwidth. Also, it should have a lightweight, compact form factor, and mechanical robustness to avoid any damage caused by the UAV vibration. Many types of antennas are widely used as a traditional solution to achieve these requirements, such as horn, Vivaldi, and cavity-backed antennas [42-44].

The horn antenna can achieve high gain with wide bandwidth. However, the narrower main beam in the radiation patterns requires a larger aperture area at the opening end. In addition, the size and weight of the horn antenna make it difficult to mount on a sUAV,

especially at the lower frequency range. Phased array antennas are usually a good choice for communications and radar applications. However, their complex feeding networks limit the ability to develop a large number of elements without sacrificing the overall weight and size [45], [46]. The cavity-based antenna can be used in wideband applications, but the cavity spacing will be larger at the lower frequency bands which requires complex designing methods to miniaturize a large array [47].

Among many different types of antennas that have been reported in the literature, the DRA has several attractive features such as wide bandwidth, high gain, high efficiency, and low losses, which make it an excellent candidate for many applications [48]. The DRAs features got attention to be exploited in radar applications many years before [49]. However, the interest in DRAs revived because of the recent advances in fabrication methods and the availability of many new dielectric materials with enhanced properties.

On the other hand, Vivaldi antenna can have as wide as 22:1 of impedance bandwidth [50], [51]. However, the main challenge in designing a Vivaldi antenna is to maintain stable radiation patterns at the higher end of the operating frequency band where the antenna works as a travelling wave radiator.

In this chapter, three different designs for UWB UAV radar antenna arrays are explored, designed, simulated, fabricated, and tested for UAV radar experiments. The first design is an 8 by 8-element RDRA with 50% impedance bandwidth. Then, a smaller and modified version of the first array is presented with ceramic-based RDRA to achieve 83% of impedance bandwidth. Also, a Vivaldi array with 132% impedance bandwidth and a gain of up to 25 dBi is presented. Finally, other related antenna works for radars are discussed including the design of a T-shaped Vivaldi antenna configuration and a Ku-band antenna array for manned-aircraft radar.

3.2 Dielectric Resonator Antenna (DRA)

In this section, a wideband, low-profile, and high-efficiency 64-element RDRA planar array with (8×8) arrangement is introduced. The proposed array shows very good shielding for the large feeding network while keeping a 50% bandwidth with symmetric radiation patterns, high gain value over the frequency band of interest, high Front-to-Back (F/B) ratio, and strong mechanical structure that could be mounted on a UAV or airplane. Also, a modified version of the RDRA array with (8×1) arrangement will be designed to extend the bandwidth up to 83%.

3.2.1 (8×8)-element RDRA Array with Stripline Feeding

As the DRA radiates through the whole surface, it is important when designing a large array to make sure that the feeding network is isolated from it to prevent higher cross-polarization level. In [52], the DRA was placed on the top side of the substrate and directly on the ground plane with a microstrip feeding network on the other side of the substrate. The design achieved a wide bandwidth up to 76% for a 16-element array. However, the F/B ratio was around 10 dB. The F/B ratio was improved by adding a reflector on the back side of the substrate with sufficient distance to ensure that the matching was not affected, Nikkhah et al. [53]. However, this approach increased the overall height of the array. Moreover, in S. Tang et al. [54], a low-profile DRA was fed by slot aperture for a 4 × 1 array. The feeder and substrate were isolated by a ground plane to achieve 15 dB of F/B ratio yet with a narrow bandwidth of 17% from (4.35 to 5.37) GHz. Therefore, a stripline feeder for an array could provide a good solution for reducing the interference between the radiators and the feeder as well as between the feeder and the other electronic components of the RF system.

In the beginning, a single-element RDRA is designed using Rogers RO 3010 material with relative permittivity of 10.2 and dielectric loss tangent of 0.003. The RDRA has a square

base with an area of a^2 and height b with 13.6 and 11.5 mm, respectively, as shown in Fig. 3.1. Two different substrates are used for the feedline. The upper substrate material is Rogers RO 4350 with relative permittivity of 3.66, dielectric loss tangent of 0.004, and thickness of 1.524 mm. The lower substrate is Rogers RT / Duroid 5880 with relative permittivity of 2.2 and 1.575 mm thickness.

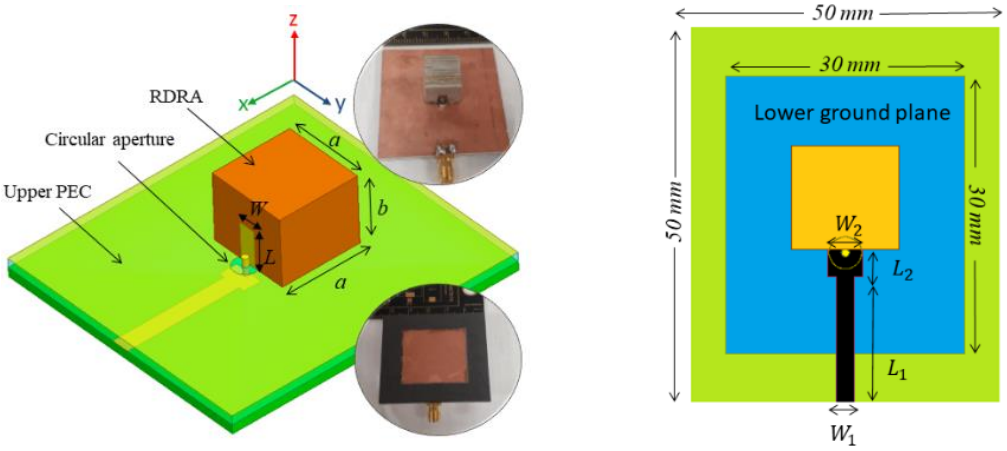

(a) (b)

Figure. 3.1 RDRA geometry (a) 3D view with fabrication (b) top view.

The connection between the feeder and the vertical strip (W=2.7 mm, L=5.77 mm) at the front face of the RDRA is conducted using a cylindrical probe with a radius of 0.5 mm. This probe passes through a circular ground-cleared area created at the upper ground plane with 1.7 mm radius. Another ground plane with (30×30) mm^2, is assigned under the lower substrate to reduce the back-lobe radiation. The feeder's dimensions are W_1, W_2, L_1, and L_2 which correspond to 2.67, 5, 17.3, and 3.1 mm, respectively. The electromagnetic simulation is conducted with ANSYS HFSS 2020 R2 [55]. The results show that the -10 dB reflection coefficient covers the frequency range from 4.21 to 6.45 GHz, while the peak realized gain is varied between 4 and 7 dBi across the operating band. The measured and simulated results are in fairly good agreement. An average radiation efficiency of 95% is achieved throughout the frequency band of interest,

which is one of the main features to build an array with large number of elements with an integrated feeding network, as shown in Fig. 3.2.

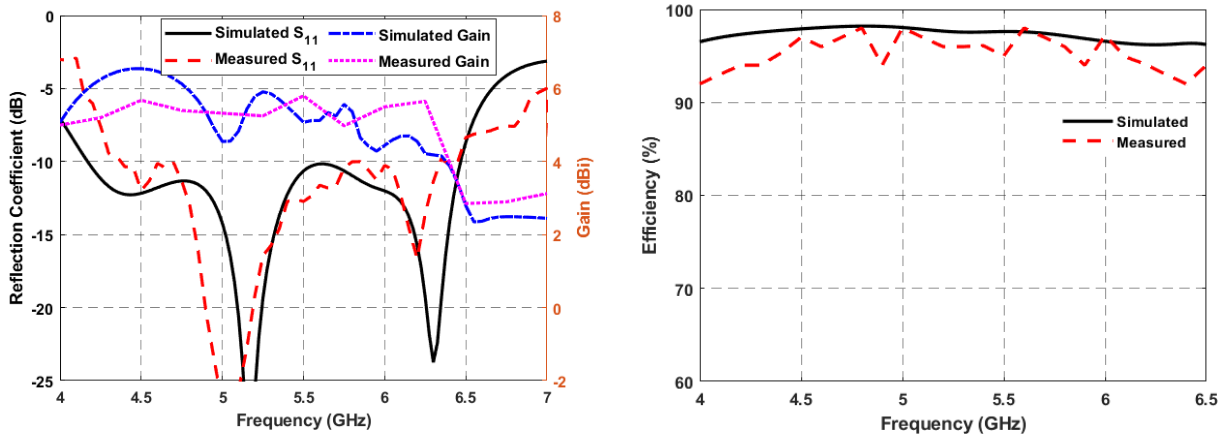

(a) (b)

Figure. 3.2 Single-element RDRA (a) reflection coefficient and gain (b) radiation efficiency.

Fig. 3.3 shows that the main lobe is directed along the +*z* axis. A low cross-polarization level of -20 dB and about 12 dB F/B ratio are observed at the *yz*-plane. The cross-polarized component at the *xz*-plane is less than -50 dB and is not shown in Fig. 3.3(b).

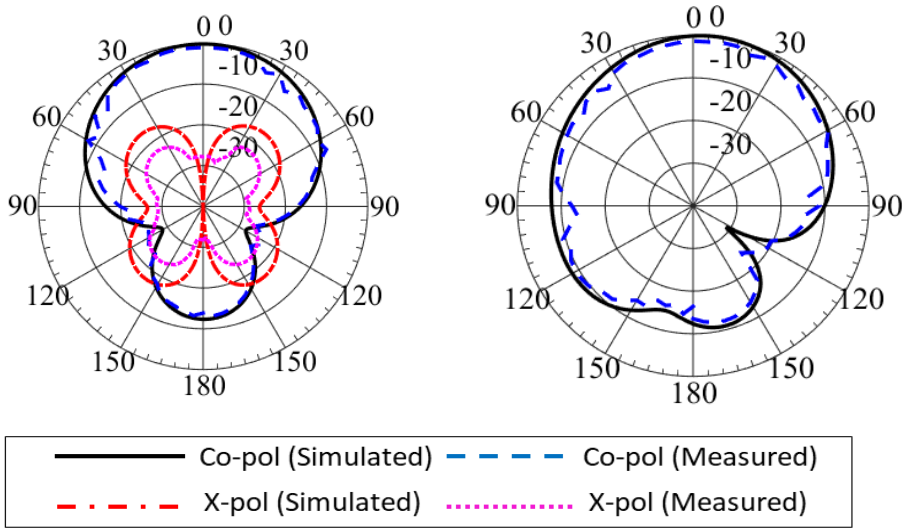

(a) (b)

Figure. 3.3 Radiation pattern of the single element RDRA at *f*= 4.6 GHz (a) *yz*-plane (b) *xz*-plane.

Fig. 3.4 shows the electric field distribution. Two resonant modes are observed across the frequency band of interest. The dominant $TE_{1\delta1}$ mode starts from the beginning of the operating band until the second resonance at f=6.3 GHz where the $TE_{2\delta1}$ starts to propagate [56].

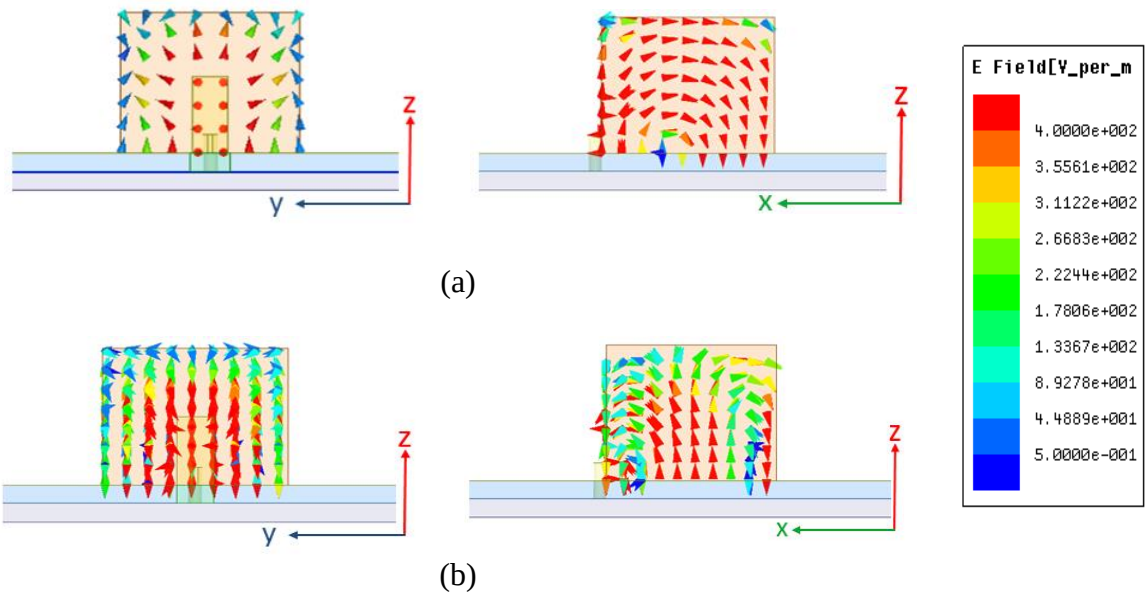

(a)

(b)

Figure. 3.4 The electric field distribution in vector format (a) f= 4.6 GHz (b) f= 6.3 GHz.

In order to design a large array from the single RDRA design, the distance between the elements should be taken carefully into consideration. In the array radiation, the side lobes are the result of interference from nearby radiating elements. In general, to suppress the occurrence of these grating lobes, one has to make sure that the distance between the elements should be smaller than one wavelength and not less than half wavelength throughout the band. However, for wideband antennas, an appropriate element spacing needs to be determined by placing multiple single RDRAs excited independently alongside each other as shown in Fig. 3.5(a). Mutual coupling is the measure of how much electromagnetic energy is coupled to each element and can be quantified with the scattering parameters, $|Sij|$ where i and j are indexes of each element ($i \neq j$).

After applying a parametric sweep over the distance between the elements, it is observed that at 25 mm of spacing, the mutual coupling between the neighboring elements through the frequency of interest is less than -13 dB except it reaches to -11 dB at *f*=5.4 GHz, as shown in Fig. 3.5(b). Also, the inter-element mutual coupling represented by the |S23| parameter shows the same level as the edge-element mutual coupling, |S12|. Thus, each DRA is spaced apart by the observed distance in both directions in the 2D array design to achieve more symmetrical radiation patterns.

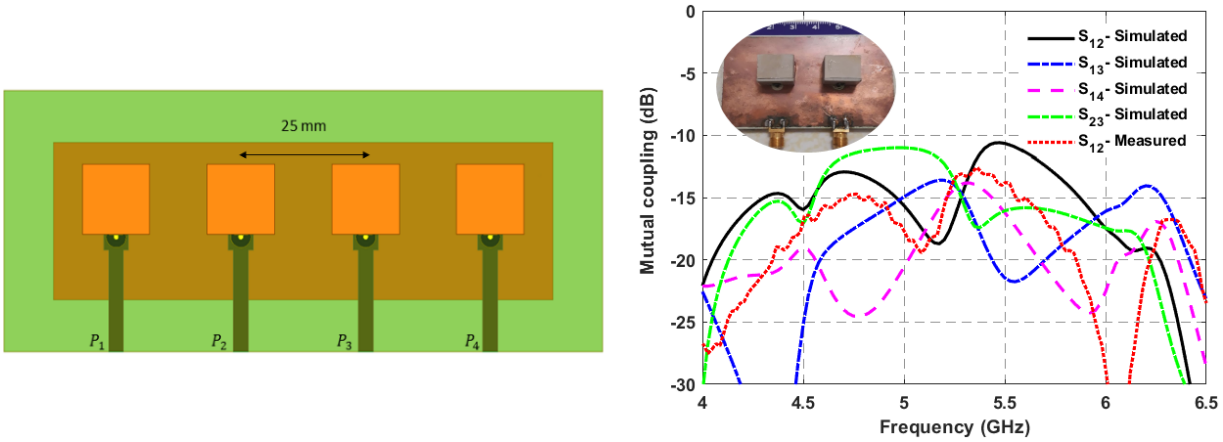

(a) (b)

Figure. 3.5 (a) single excitation neighbor elements RDRAs (b) mutual coupling.

A cooperate stripline feeding network is designed to excite the 64-element RDRA array, as shown in Fig. 3.6(a). The multi-section power divider is shown in Fig. 3.6(b). The dimensions of the feeder are W_2, W_3, W_4, W_5, L_3, and L_4 which correspond to 3.2, 1.5, 1.95, 0.25, 39.3, and 8 mm, respectively. The overall size of the array substrate is 215×215 mm^2, which corresponds to ($2.7\lambda_o$ ×$2.7\lambda_o$) which is considered relatively small compared to the large number of elements at this frequency range. As could be seen, the upper ground plane has the same size as the substrate while the lower ground has a smaller size of 195×193 mm^2. The total capacitance of the stripline is a summation of the parallel-plate capacitance (C_p) and fringing capacitance (C_f) [57]. The (C_f)

value will vary if the lower ground size is changed which affects the characteristic impedance. However, the (C_p) value stays the same as long as the lower ground plane covers the conductor in the middle, which is the case in this design. By reducing the ground size, the input impedance is slightly increased to match the 50 Ω port over the band. The overall weight of the 8×8-element array is 650 g.

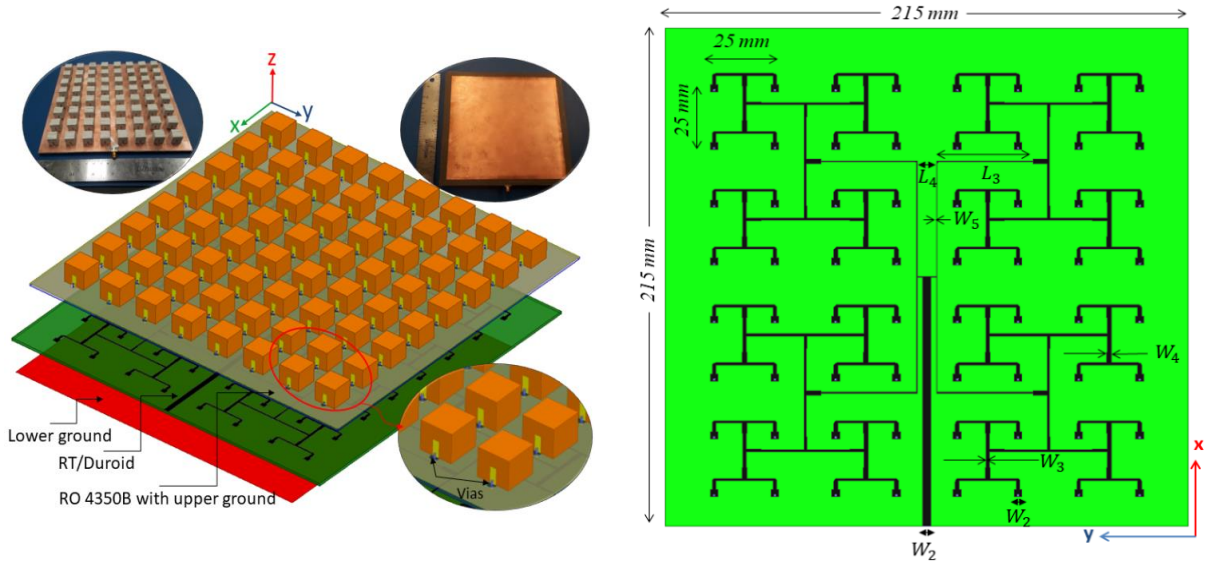

(a) (b)

Figure. 3.6 Geometry of the (8×8) planar array (a) 3D view with the fabricated array (b) feeder.

Fig. 3.7 shows the -10 dB reflection coefficient from 3.79 to 6.29 GHz, achieving 50% impedance bandwidth. The full ground plane at the bottom side of the lower substrate significantly degrades the overall matching. Also, a smaller ground plane allows the feeder radiation to adversely affect the close components of any RF system connected to the antenna, which illustrates the importance of choosing the appropriate dimensions of the ground plane to achieve the optimum bandwidth [58]. The peak realized gain varies between 18 and 22 dBi throughout the band as shown in Fig. 3.8(a). Some ripples in the gain value with respect to the

frequency show within the operating band. However, the mean value of the gain is increasing from the lower to the upper-frequency band, as the distance between the elements will increase with respect to the guided wavelength. The average radiation efficiency is 85% across the frequency of interest, as shown in Fig. 3.8(b). This efficiency is considered high compared to (8×8) array [59]. Although some discrepancies between the simulated and measured results come from the tolerance in the fabrication process, the measurement and simulation are still in fairly good agreement. The radiation patterns for the 64-element array are plotted for different frequencies in Fig. 3.9. The results show that the cross-polarization level is less than -25 dB in the *yz*-plane and -50 dB in the *xz*- plane in the operating band. The side lobe level (SLL) is between -15 and -18 dB for both the *yz* and *xz*-plane. The HPBW varies between 13º to 18º degrees while the F/B is around 20 dB through the frequency of interest. The symmetry in the radiation at the yz-plane is excellent but it is slightly less at the xz-plane as the RDRA has a higher electrical field intensity at the vertical strip side as illustrated in Fig. 3.4.

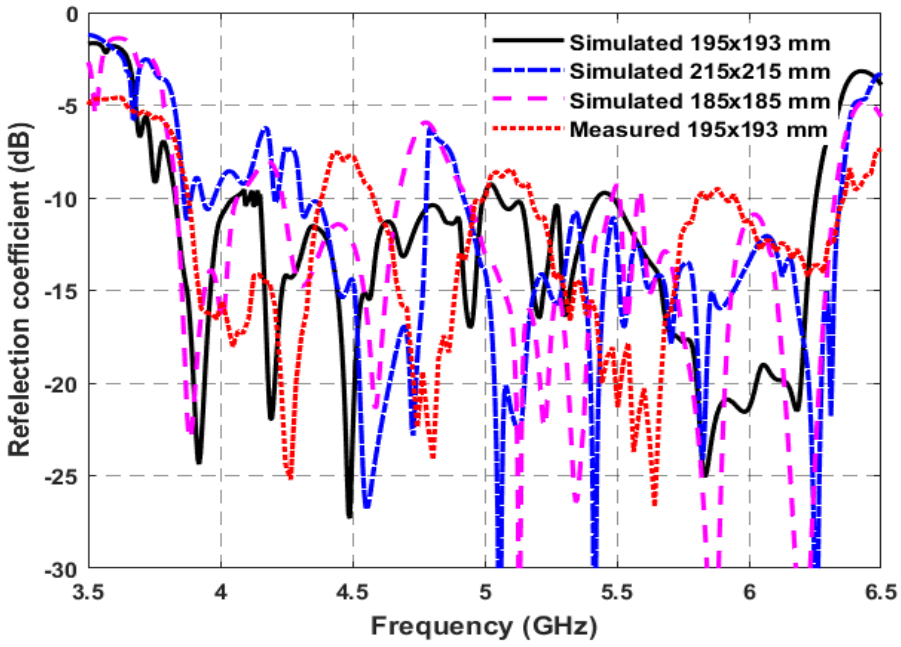

Figure. 3.7 Reflection coefficient of the 8×8 proposed planar RDRA array.

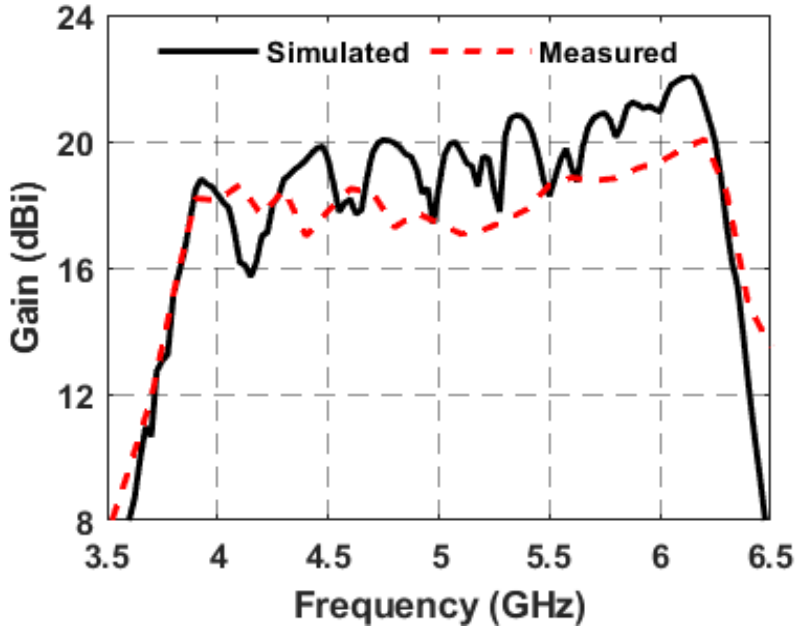

(a)

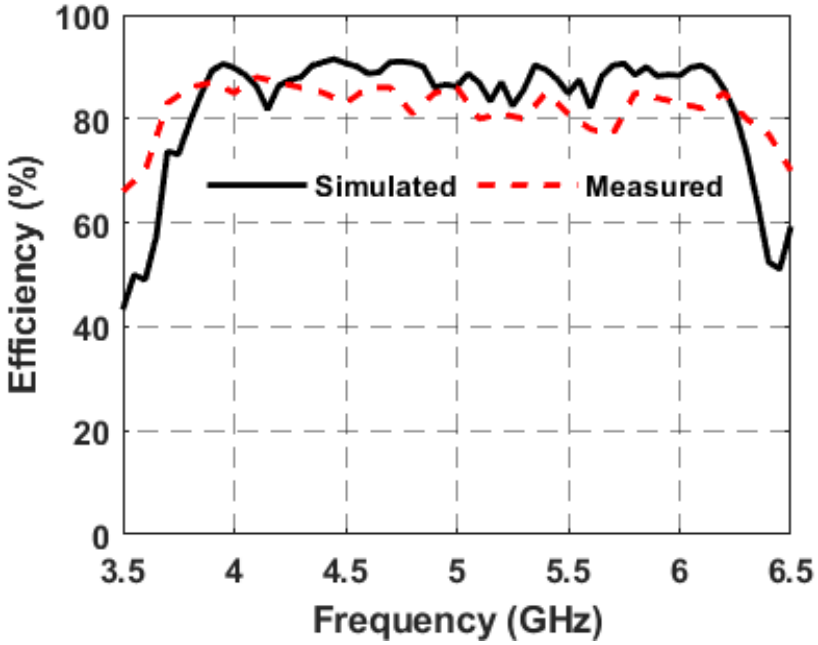

(b)

Figure. 3.8 (8×8) planar array (a) peak realized gain (b) radiation efficiency.

(yz-plane) (xz-plane)

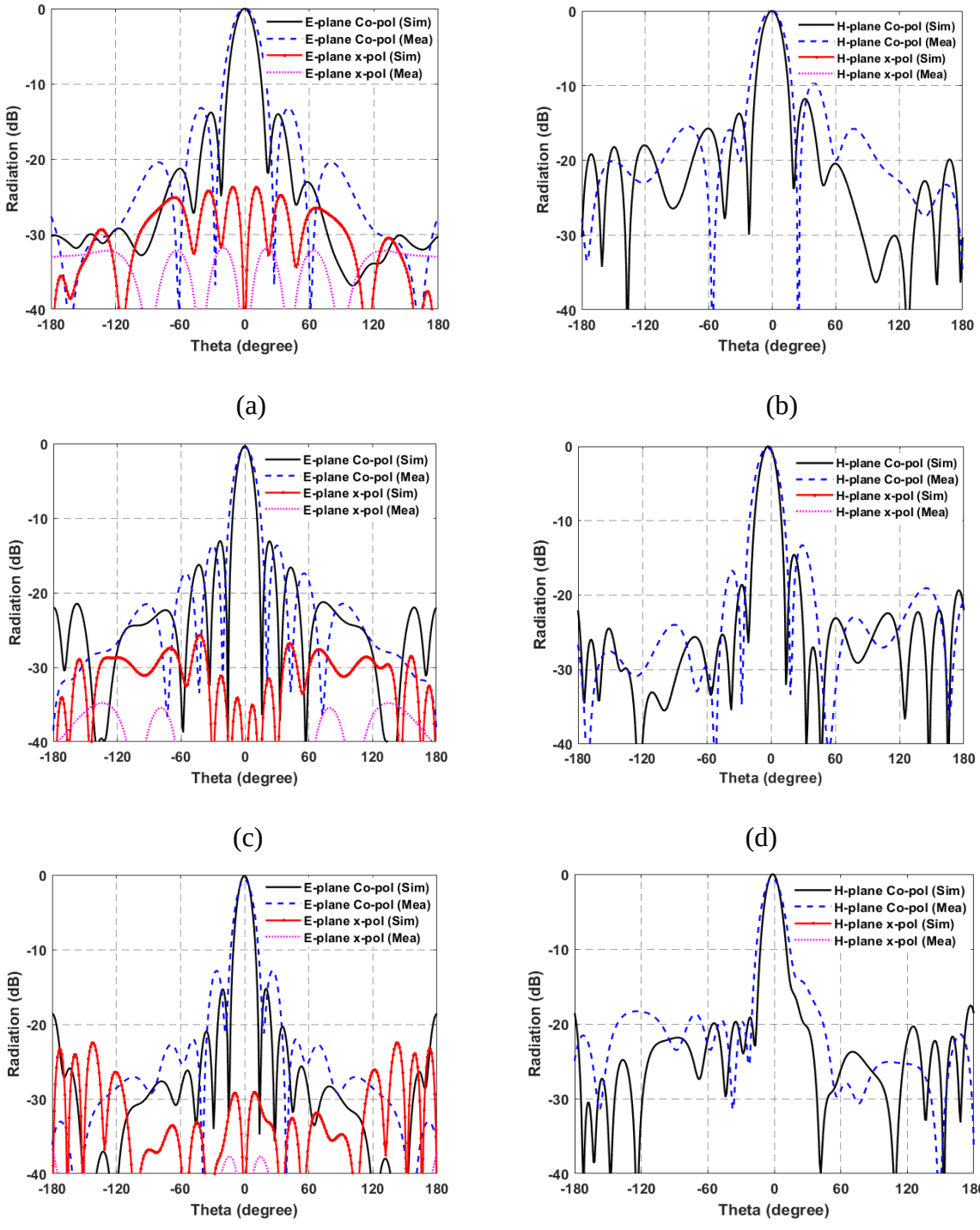

(a) (b)

(c) (d)

(e) (f)

Figure. 3.9 Radiation patterns for the (8×8) RDRA planar array at different frequencies (*a* and b) *f*=4 GHz, (c and d) *f*=5.1 GHz, and (e and f) *f*=6.1 GHz.

3.2.2 (1×8)-element Ceramic-based RDRA

This section presents a modified version of the previous array. In this design, a ceramic-based RDRA array is designed to achieve 83% of impedance bandwidth with stable radiation patterns throughout the frequency band of interest. Fig. 3.10 shows the geometry of the proposed RDRA antenna array. Similar to the 8×8 design, the RDRA is situated on the top side of the substrate and the microstrip power divider is on the backside to isolate the feeding network spurious radiation.

Herein, only one substrate is used and a metal reflector is placed at the lower back of the substrate for improving the F/B ratio and allowing for the mounting on the UAV. The RDRA material is TMM10 with a relative permittivity of 9.2. To support the radar frequency range extending from 2.5 GHz to 6 GHz, the 14 mm-thick RDRA is designed.

The power divider substrate is built with Rogers RO 4350 with relative permittivity of 3.48, and the metal back reflector is placed 10 mm below the array. The RDRA block is made with three dielectric blocks. Two of these three blocks are of the same thickness (6.25 mm), and one is 1.52 mm thick. The trapezoidal conductive strip is milled on the front face of the first ceramic layer and connected to a probe. The overall weight for this design is 255 g with a footprint of 250×100 mm^2, which is considered suitable for the UAV. The proposed array's optimized dimensions are shown in Fig. 3.10 with fabrication.

Fig. 3.11 shows the measured and simulated results of the antenna array. A comparison of the antenna array's measured and simulated reflection coefficients is shown in Fig. 3.11(a). The results show that the array covers the frequency band of 2.5-6 GHz, with 83% impedance bandwidth. Fig. 3.11(b) shows the measured and simulated gain of the antenna array.

The peak realized gain varies from 12 to 14 dBi. The radiation efficiency (Fig. 3.11(c)) is about 95% through the band. The differences between the simulation and measurement are due to the fabrication tolerance of the DRA, where we used a glue material to attach the DRA.

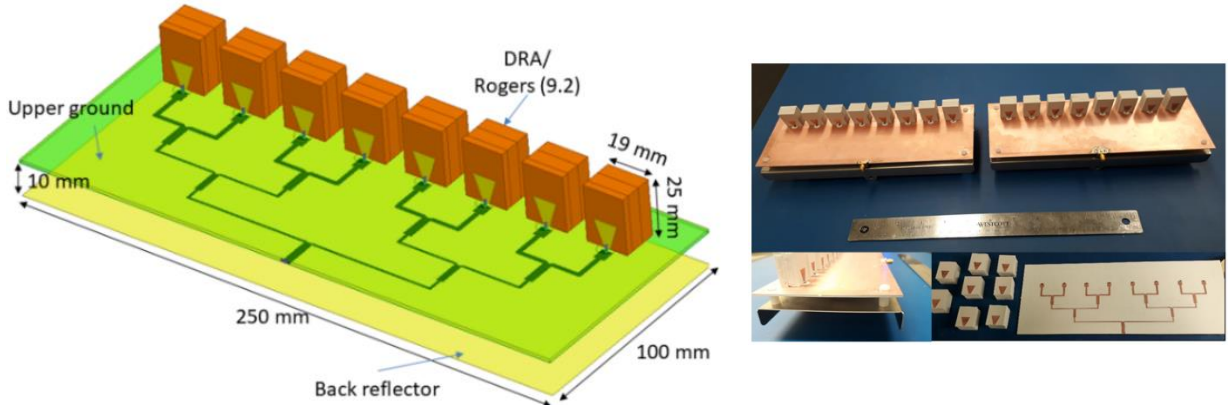

Figure. 3.10 The geometry of the (8×1) RDRA array with the fabricated prototype.

The radiation patterns are plotted in Fig. 3.12 for different frequencies. The sidelobe level (SLL) is approximately -15 dB with very good symmetry around the main beam. The E-plane half-power beamwidth (HPBW) varies between 19° and 12° over 2.5-6 GHz. In addition, the F/B ratio is better than 15 dB throughout the frequency of interest.

Also, it was found that the cross-polarization level is better than -25 dB. The measured and simulated radiation patterns are in good agreement. The array is installed on a UAV for radar measurement with spacing between the transmitter and receiver of 1.3 m to achieve isolation of 45 dB or better.

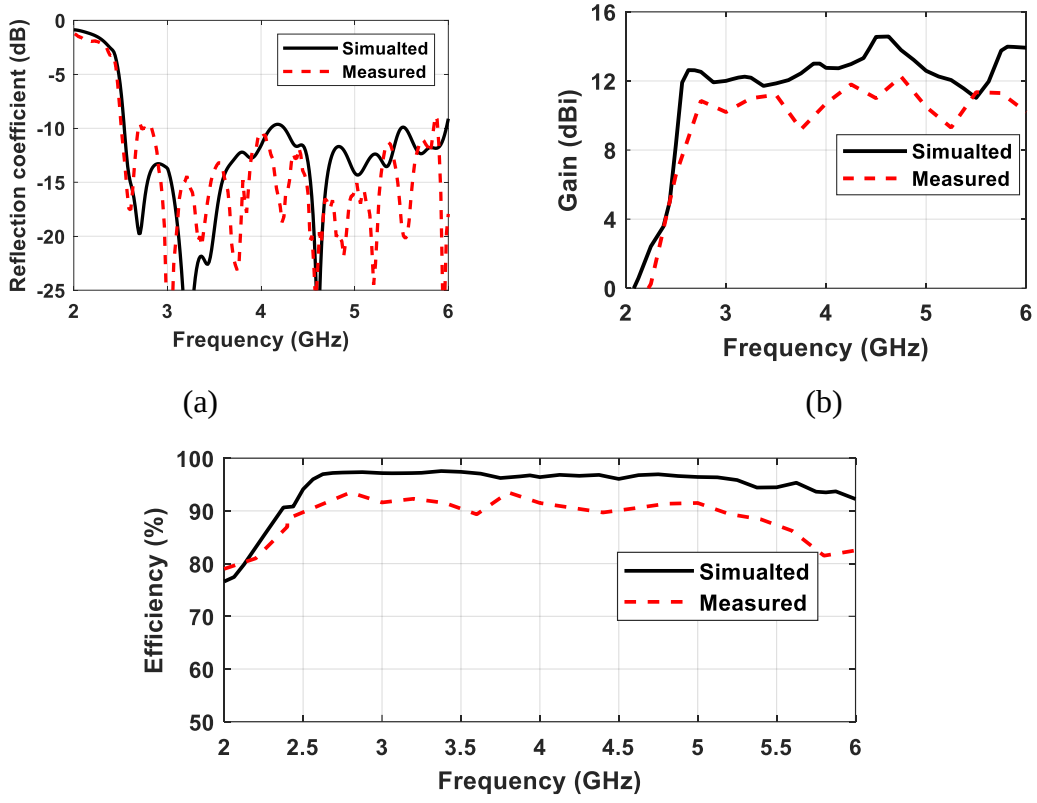

(a) (b)

(c)

Figure. 3.11 (8×1) RDRA array (a) reflection coefficient (b) realized gain (c) radiation efficiency.

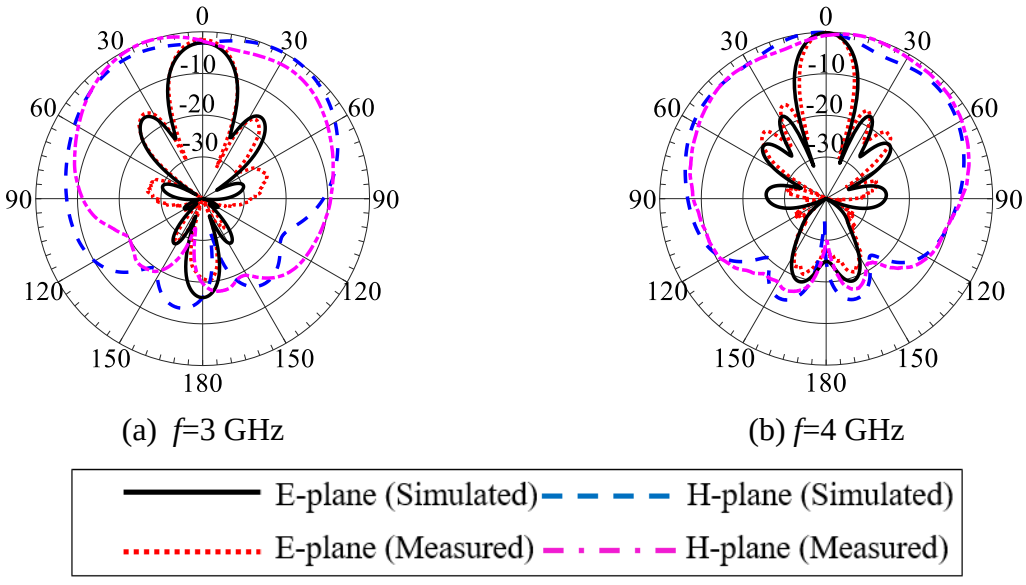

(a) *f*=3 GHz (b) *f*=4 GHz

Figure. 3.12 Simulated and measured radiation patterns for the (8×1) RDRA array.

3.3 Coplanar Vivaldi Antenna Array

3.3.1 Vivaldi Antenna Design Literature Review

Vivaldi antenna design has been a subject of extensive research for many years, the main focus was on improving the radiation pattern as the impedance bandwidth and gain have good characteristics relative to the majority of the other types of UWB antennas. Langley et al. [60] introduced the balanced antipodal Vivaldi antenna (BAVA) with two slots on opposite sides of the antenna's substrate to improve the CVA radiation performance. Subsequently, various methods were reported to improve the antipodal Vivaldi antenna (AVA) radiation performance, for instance, by adding a small resonator [61]-[64] or a parasitic elliptical patch [65] in the flared aperture which result in improving the gain value. Nevertheless, these require increasing the size of the substrate to situate these extra resonators. Zhu et al. [66] presented a linear AVA array with a metasurface located at the aperture with maintaining the same substrate size. The gain showed an average of 2 dBi improvement, though at the expense of a high SLL. In a similar approach, Liu et al. [67] placed a triangular patch on the two substrate sides of the AVA array's aperture. The gain showed an improvement at the higher frequency end but with the presence of anti-symmetrical SLL. In addition, creating slots in the geometry of Vivaldi antenna to improve the bandwidth, gain, and radiation patterns has been reported. Fei et al. [68], Oliveira et al. [69], Liu et al. [70], and Abbak et al. [71] showed that corrugated edges or multiple slots can improve the antenna performance. However, the effect at the array level was not mentioned. Nurhayati et al. [72] showed that corrugated slots at the end of the Vivaldi antenna's outer sides can improve the mutual coupling between the elements of the array. However, their array's radiation patterns suffer from a high SLL through the operating band. Zhu et al. [73] proposed a method to reduce the mutual coupling for the AVA array by adding multiple notches in the ground plane.

However, the grating lobes are still distorted. Alternatively, a dielectric lens can be used to improve the radiation pattern of a Vivaldi antenna by extending the end portion of the substrate into different shapes, e.g., circular, triangular, or trapezoidal [74]-[76]. However, with a drawback of increasing the antenna's footprint to provide more directivity. It is common that the lens material is the same as the antenna substrate, which is usually a low dielectric constant to widen the bandwidth. However, higher permittivity dielectrics lenses were used in the radiation aperture to focus the energy more toward the broadside direction. Bourqui et al. [77], Juan et al. [78], and Amiri et al. [79] proposed a modified (BAVA) by creating an aperture (gap) in the antenna substrate and inserting a higher dielectric constant material in the created gap to improve the directivity. A multi-layer dielectric lens was also inserted in front of the antenna aperture [80]. However, creating an aperture in the substrate and filling it with another dielectric material adds more complexity to the fabrication process and causes phase velocity variation for the electromagnetic waves travelling toward the end of the aperture.

Another approach by surrounding the Vivaldi antenna by either a low dielectric constant material or a 3D phase lens to improve the gain and radiation performance was reported [81], [82]. Also, a 3D massive dielectric lens was added at the aperture end of the antenna [83]. These 3D surrounding materials showed an improvement in the antenna performance such as gain and radiation pattern with SLL suppression. Unfortunately, the bulky size limits the benefits of this approach if a large antenna array is needed.

On the other hand, DRA is a 3D antenna with one more degree of freedom compared to patch antennas. This feature provides the ability to excite the desired modes with different radiation patterns that cannot be generated in a 2D antennas. In addition, the DRA radiation efficiency is higher than the 2D antennas. However, the DRA profile makes exploiting it more

challenging if low-profile antennas are needed. Thus, the dielectric patch antenna (DPA) is a compromise between the DRA and the patch antenna. The DPA is a low-profile DRA with a ratio between the maximum edge length and the height of 10 or more. Lai et al. [84] and wang et al. [85] designed DPAs and showed that these radiators can achieve high efficiency with more than 5 dBi gain even though with a high dielectric constant material. Tang et al. [54], proposed another PDA design with a bandwidth up to 20%.

3.3.2 Coplanar Vivaldi Antenna Linear (4×1) Array Design

Fig. 3.13(a) shows the conventional 4×1 CVA array designed on a Rogers RO3003 substrate with a relative permittivity and thickness of 3 and 0.762 mm, respectively. Both tapered edges of the antenna are on the top side of the substrate while the power divider is on the back side. A multi-stage power divider is used to make a smooth transition to the 50 Ω port. The Vivaldi tapered equation is given by (3.1):

$$y = Sve^{-xt} + C_1 \tag{3.1}$$

where, S is the half throat width of the antenna and is equal to 0.35 mm, t is the exponential tarped factor and equal to 84, C_1=19.1 mm, (0 mm $\leq x \leq$ 33.9 mm) and v=±1.

The CVA dimensions W and L are 186 and 93 mm, while the dimensions of the DPA are d, W_d, r_d, W_1, and L_1 which correspond to 21, 20, 7.8, 3, and 15 mm, respectively. At the lower end of the CVA, an elliptical gap is created with major and minor axes of 7 and 3 mm, respectively. Since the CVA design is a linear array, the E-plane mutual coupling can be reduced by creating a narrow gap (W_g =1 mm) between the elements as illustrated in Fig. 3.13(b). Then, two slots with exponential taper are created to each flare of the single antenna. Each slot has different optimized variables to improve the matching. The separation between the centers of slots is 20.1 mm. The

corner edges in the design are smoothed to minimize the unwanted wave diffraction that affects the return loss. The slots equations are given by (3.2).

$$\text{Slot}_{1,2} = C_2 u e^{-kt} \tag{3.2}$$

where for slot$_1$, C_2=0.8 mm, t=116.4, (19.5 mm $\leq k \leq$ 40 mm) and (-0.55 $\leq u \leq$ 1.25), while C_2=0.95 mm and t=125 for slot$_2$.

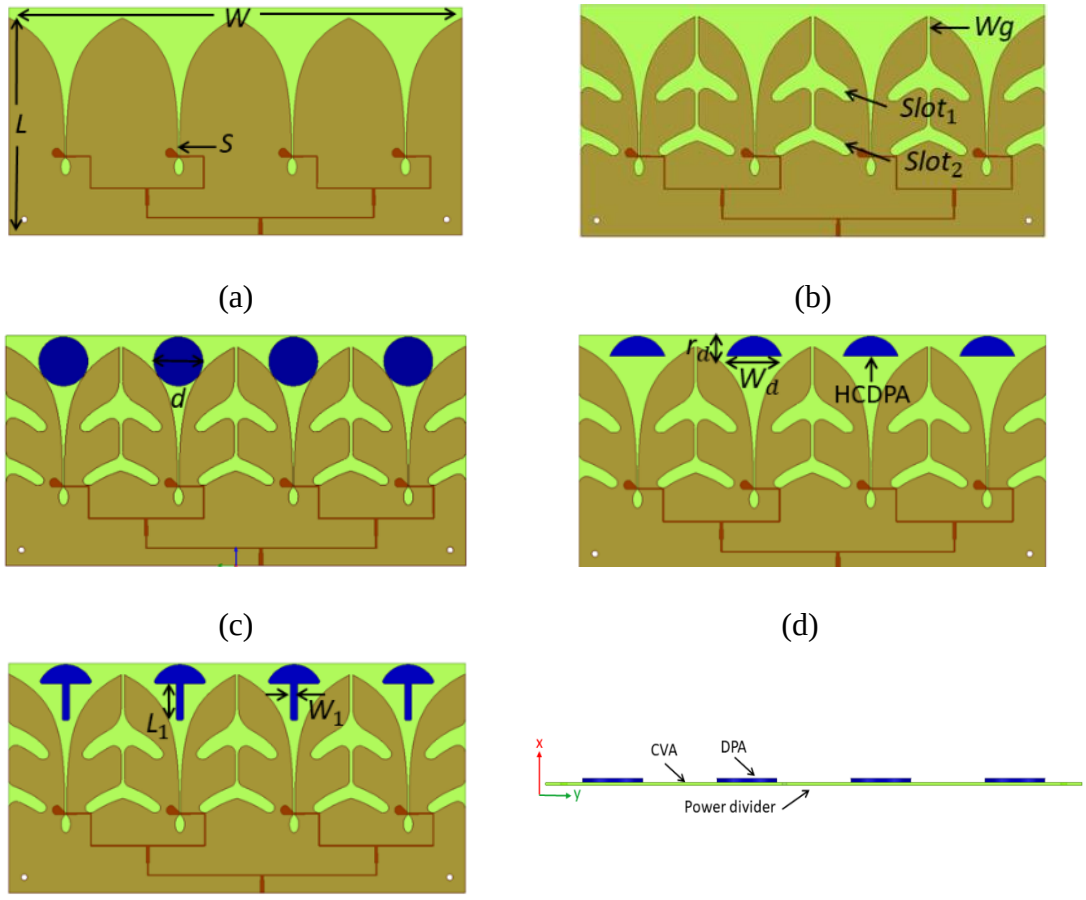

(a) (b) (c) (d) (e) (f)

Figure. 3.13 The development of the CVA array (a) conventional CVA (Ant I) (b) CVA with slots (Ant II) (c) CVA with CDPA (Ant III) (d) CVA with HCDPA (Ant IV) (e) umbrella-shaped DPA (Ant V) (f) Side view (Ant V).

The mutual coupling degrades the overall gain of the array due to the out of phase current distribution of the unwanted waves travelling between adjacent elements. Particularly, in the

CVA E-plane, travelling waves between elements on the same substrate have a significant effect on the performance of the array. The mutual coupling can be reduced by increasing the distances between elements, but this causes higher grating lobes, especially in the UWB antennas, where the distance between the elements exceeds 2 λ_g. In general, the spacing between the elements (W) is given by (3.3).

$$w < \frac{\lambda g}{1+|\cos \varphi|} \tag{3.3}$$

where, φ is the angle of the main beam. For the broadside radiation, the grating lobes will increase once the spacing between the elements exceeds one wavelength. On the other hand, larger spacing leads to a narrower main beam in radiation patterns, which is desired in radar applications. Thus, the radiation patterns of the proposed CVA array will be improved by placing a cylindrical DPA (CDPA) at the end of the flared aperture of each element, as shown in Fig. 3.13(c). The CDPA material is TMM10 with relative permittivity of 9.2, diameter (d) of 22 mm, and thickness (h) of 1.27 mm. The DPA will be coupled through the electric field distribution of the radiation aperture in the Vivaldi antenna. In Fig. 3.13(d), the CDPA is cut slightly above the center to form a half CDPA (HCDPA). Finally, in Fig. 3.13(e), an extension of the HCDPA is added to form an umbrella-shaped DPA. This geometry shows significant capabilities to direct the surface current and improves the proposed array's radiation patterns.

The reflection coefficient for the final design covers the frequency band from 2.77 to 13.6 GHz, with 132% fractional bandwidth, as illustrated in Fig. 3.14(a). This bandwidth is sufficient for most of the UWB radar applications including measurements of snow thickness and soil moisture [25], [86]. The gain value is shown in Fig. 3.14(b) and clearly improves once the slots are created between the adjacent elements. This result is expected, as the mutual coupling is reduced by the presence of slots. The shape of slots is important as stronger current intensities

will be created around them which improves the gain. However, in some cases, slots may degrade the gain at certain frequencies [87], [88]. Notably, slot shapes and their locations were optimized carefully to improve the gain over the entire frequency band. Both CDPA (Ant III) and HCDPA (Ant IV) show a slight improvement in the gain value, but the HCDPA improves the matching at the center of the operating band. The umbrella-shaped DPA shows improvement with an average of 1 to 2 dBi after *f*=7 GHz, where the gain of the final design varies from 10.8-17.8 dBi.

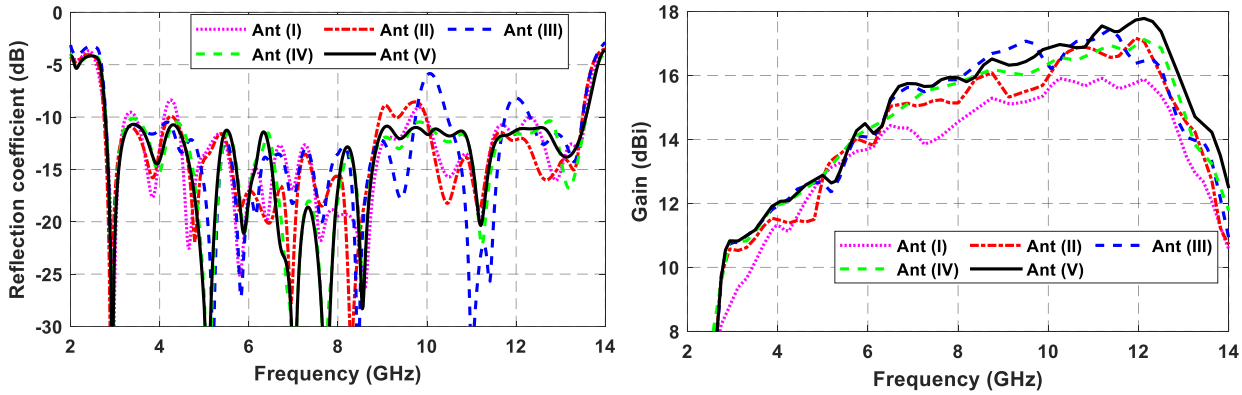

(a) (b)

Figure. 3.14 CVA development stages performance (a) reflection coefficient (b) peak realized gain.

The DPA shape is important as the coupling between the electric field in the CVA and the DPA depends on the position and the occupied area of the DPA with respect to the maximum current intensity. The E-plane radiation patterns of the proposed array show that the final design with the umbrella-shaped DPA improves the radiation patterns by suppressing the side lobes and grating lobes at the higher frequencies between 5-8 dB, as shown in Fig. 3.15. As the gain value gets slightly improved, the half power beam width (HPBW) gets narrower by approximately 1 to 2 degrees at the higher frequency band. Another notice is that the DPAs in the final design (Ant V) provide a very good symmetry in side lobes as well as grating lobes around the main beam.

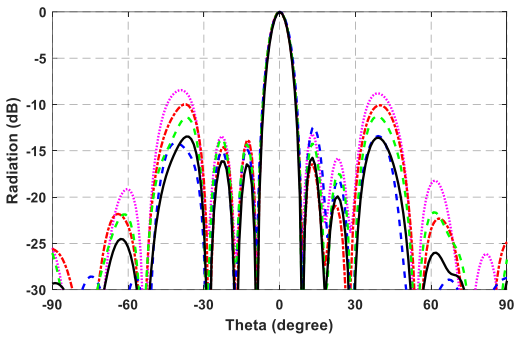

(a) *f*= 10 GHz

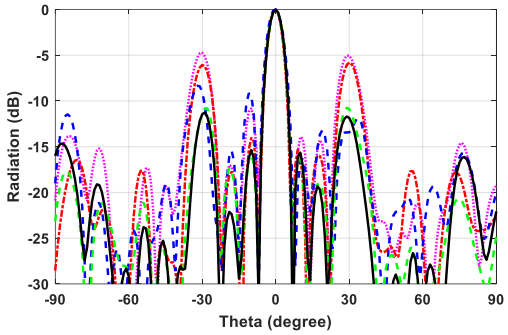

(b) *f*= 12.5 GHz

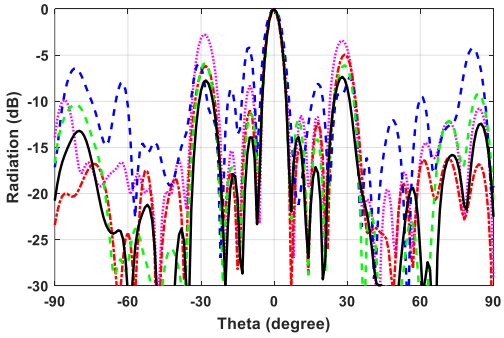

(a) *f*= 13.25 GHz

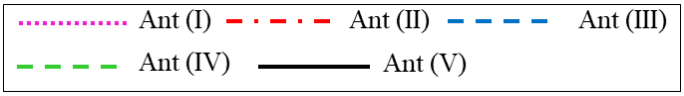

Figure. 3.15 Co-polarized E-plane radiation patterns of the 4×1 CVA array.

In this design, the distance between the elements at the end of the frequency band exceeds 3.5 λ_g. Despite this large spacing, the grating lobes and the first sidelobes are 11 dB below the main beam except at *f*=13.25 GHz, where the grating lobes reach to 9 dB below the main beam. The slots in Ant (II) improve the grating lobes up to *f*=10 GHz, where the inter-element spacing is about 2.5 λ_g. However, at higher frequencies with spacing between elements increases in wavelength, the DPAs provide more suppression of grating lobes. The cross-polarization level and F/B ratio are larger than 25 and 15 dB over the frequency range of interest, respectively. The traditional approaches to suppress the grating lobes by tapering the edge element of the array or using a non-uniform spacing degrade the gain value. However, in the

proposed design, the overall gain is improved while the grating lobes are suppressed by a notable value. The low-profile DPA contributes to the CVA array's overall radiation after the cut-off frequency of the first mode, which is approximately 7 GHz. At this frequency, the CVA grating lobes increase till the end of the operating band. The higher permittivity material of the DPA causes the radiation pattern to be more focused towards the CVA end-fire direction with compact size. However, the fractional bandwidth will be narrower [89]. Based on that, the selected material for the DPA is TMM 10 with relative permittivity of 9.2. The DPA ceramic material has other advantages such as its availability, low dielectric loss at higher frequencies, and simplicity in fabrication.

Figs. 3.16 and 3.17 present two parametric studies of the DPA material and height effects on the CVA radiation performance. Herein the figures, the SLL is defined as the difference between the peak of the main beam and the peak of grating lobes whether it is the first adjacent lobes or the farther grating lobes in the angular region of ±60^{o} around the broadside direction. In Fig. 3.16, the SLL is compared for different dielectric materials of the DPA in Ant (V) and without the DPA in Ant (II). As shown, without the DPA, the SLL reaches to -2.7 dB at the end of the band. However, it can be suppressed to less than -12 dB with the higher permittivity material.

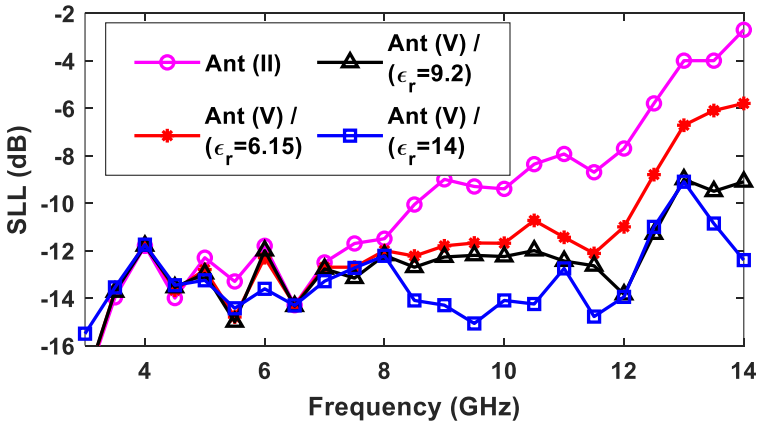

Figure. 3.16 E-plane SLL for Ant (IV) with different dielectric materials for the DPA.

One of the advantages of using the DPA instead of the previously reported dielectric lens in the literature is that it avoids cutting out the substrate and inserting another dielectric in the gap. This leads to a simplified fabrication process and a reduction in internal reflections of the electromagnetic waves between two different boundaries. Basically, the phase velocity for the wave through the CVA substrate will remain constant. Another advantage of using this design is that it offers more flexibility in changing the DPA height to further suppress the unwanted grating lobes, as shown in Fig. 3.17. In most dielectric lens cases, the thickness of the lens is limited by the substrate thickness.

However, there are two trade-offs for the DPA height that should be taken into consideration. First, even though the higher DPA will suppress the grating lobe (as illustrated in Fig. 3.17), the cross-polarization level will increase accordingly. This is due to the excitation of unwanted higher-order modes that alter the phase between the CVA fins. Secondly, the higher DPA height increases the weight of the overall array, which is one of the critical parameters for the sUAV applications. Based on the aforementioned factors, the DPA height is chosen between 1 and 1.5 mm.

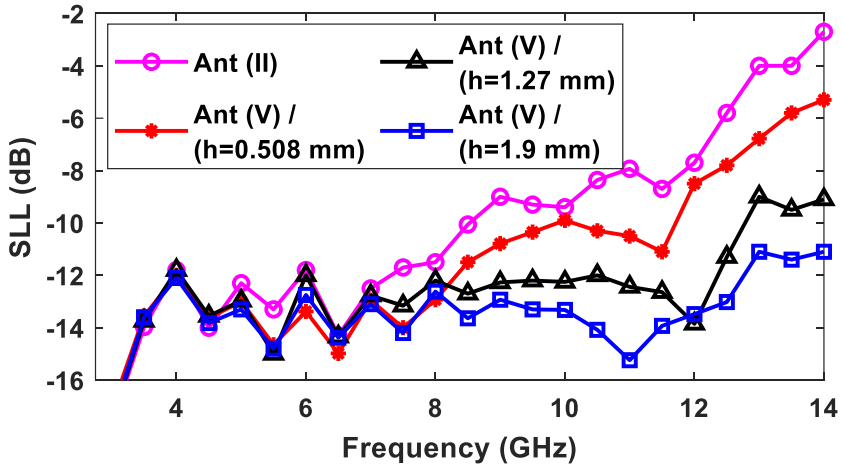

Figure. 3.17 E-plane SLL for Ant (V) with different DPA height (*h*) in mm.

The CVA operates as a resonant antenna at the lower frequency band and radiates as a travelling wave radiator at higher frequencies. The electric current model at a given wavelength for an arbitrary Vivaldi antenna with a profile of *s(x)* was reported by Chiappe et al. (3.4) [90]:

$$I(s(x)) = I_0 e^{\gamma s(x)} \times [\cos\left(k\left(s(x) - s(X)\right)\right) + j \sin\left(k\left(s(x) - s(X)\right)\right) \quad (3.4)$$

where, γ is the attenuation coefficient which is equivalent to $-t/p$ and p is the attenuation number for the antenna impedance. At higher frequencies, the current along the flared edge suffers from phase reversal which degrades the radiation performance [65]. Fig. 3.18 illustrates the conceptual reversal current for the CVA with the corresponding current loop at the radiation aperture. The electric current along the CVA tapered flare can be represented by a number of electrically small segments along the edges. Each of these segments has horizontal (I_h) and vertical (I_v) current components [91]. The horizontal current will be directed towards two different directions on each fin at the higher frequencies due to the phase reversal. However, this reversal phase is beneficial to create the required condition to excite the TE modes in the cylindrical DPA (CDPA).

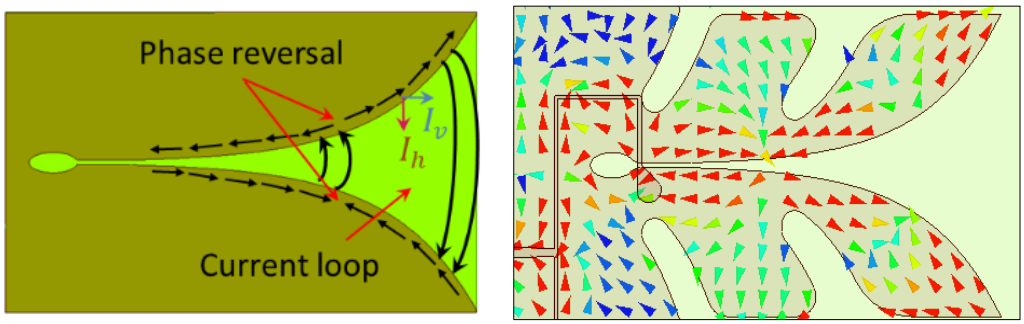

(a) (b)

Figure. 3.18 Conventional CVA current reversal (a) theoretical (b) simulation at *f*= 7 GHz.

In the previous studies, many attempts were reported to excite the $TE^{x}_{01\delta}$ and its higher order modes such as $TE^{x}_{011+\delta}$ mode in the cylindrical DRA, where the ratio between the diameter

(*d*) and thickness (*h*) is much less than 10 [92]-[95]. Normally, it is difficult to achieve a uniform current loop over a wide bandwidth because of its small radiation resistance. Accordingly, the impedance matching of the cylindrical DRA for the omnidirectional modes will be limited to a narrow band. For example, Liu et al. [92] excited the TE^{x}_{011} mode for the CDRA with 4.5 % impedance bandwidth without the need of a ground plane. However, a feeding network of printed arc-shaped dipoles was needed underneath the DRA. Furthermore, Liu et al. [95] enhanced this mode bandwidth to 16.8% by adding coupled strips to a four-arm printed network. Similar to the DRA, the low-profile DPA can radiate with the TE mode once the appropriate excitation is applied with less variation on the profile axis. The current loop in the CVA aperture, however, offers a uniform current loop distribution at higher order modes with wide bandwidth which excites the CDPA TE modes with omnidirectional radiation pattern. These modes have a horizontal-polarized omnidirectional radiation pattern that improves the E-plane radiation without degrading the H-plane radiation of the CVA, as the null of the CDPA radiation is at the CVA H-plane direction.

For the mode analysis, the CDPA in (Ant III) is considered first. This is to simplify analyzing the electric field distribution for the different modes using the basic shape. The electric field vector for the CDPA is shown at different frequencies in Fig. 3.19. At 7.5 and 9 GHz, the omnidirectional $TE^{x}_{01\delta}$ mode is propagating as expected. The proposed design excites the $TE^{x}_{01\delta}$ mode for the frequency range of 7.5-10.5 GHz, with more than 30% of impedance bandwidth. Also, the higher order $TE^{x}_{011+\delta}$ mode can be excited if a cylindrical DRA is situated with a *d/h* ratio of less than 10 [94]. Another advantage of this method is that the resonance mode in the CDPA is purely from the DPA itself as there is no embedded feeding network underneath the DPA. Normally, the feeding network will have another resonance frequency within the DPA

operating band which leads to higher cross-polarization level. The dimensions and the material of the DPA can be changed to shift the operating modes to the desired frequency range for future applications. After 10.5 GHz, the other omnidirectional mode is the TE^{x}_{121} mode [96].

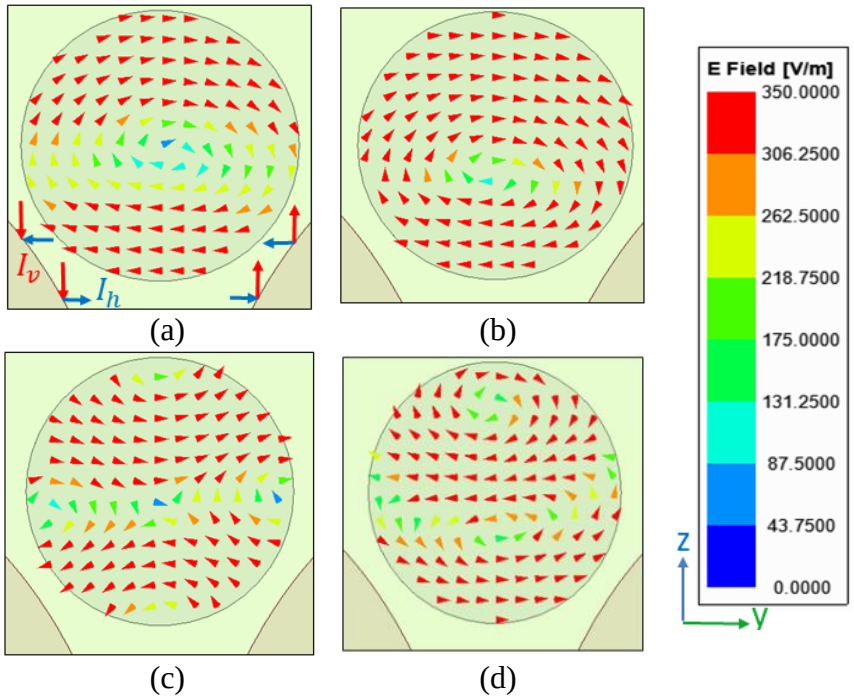

Figure. 3.19 The electric field distribution of the CDPA (a) *f*= 7.5 GHz (b) *f*= 9 GHz (c) *f*=11 GHz (d) *f*=13.25 GHz.

By examining the electric field distribution in the CDPA, one expects that the radiation pattern can be focused on different directions on the *yz*-plane. It is clear that the +z axis is the wanted direction to support the CVA end-fire pattern. The radiation in other directions degrades the performance as it generates an opposite wave travelling towards the throat of the CVA. This opposing wave performs like a multi-reflection in the overall antenna geometry and degrades the antenna matching. For this reason, the shape of the CDPA was adjusted by keeping the upper half of the dielectric loading. The electric field distribution for the proposed DPA in Ant (V) is plotted in Fig. 3.20. The modes of the proposed DPA have a similar electric field distribution as the CDPA in Fig. 3.19.

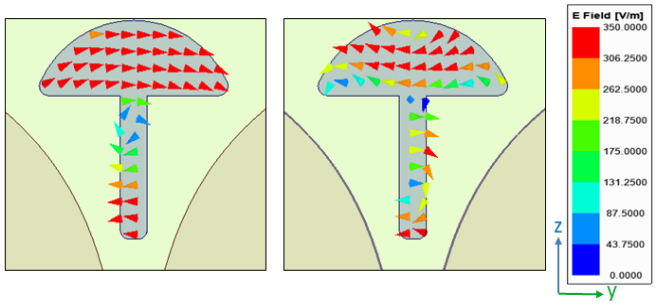

(a) (b)

Figure. 3.20 The electric field distribution of the proposed DPA (a) *f*= 9 GHz (b) *f*= 13.25 GHz.

3.3.3 Coplanar Vivaldi Antenna Planar (8×2) Array Design

To increase the penetration of the radar signal through a target (e.g., soil or ice), a high-gain antenna with a narrower HPBW along the track direction is desired [97]. Thus, four of the proposed arrays are used to form an array with 8×2 arrangement as shown in Fig. 3.21. The resulting array improves the signal-to-noise ratio (SNR) from the ground surface or any other point target as most of the energy will be focused on a smaller area. The total dimensions of the array are 377×40×93 mm^3. The linear CVA arrays were separated by a small gap of 5 mm in the *y*-direction to provide high isolation between the arrays along the *y*-direction.

The aluminum material sheet was reported previously with a wider bandwidth compared to the PCB CVA arrays [98]-[100]. Even though wide bandwidths were achieved, the heavy weight of the thick metal sheets limits the ability of such designs to be installed on the sUAV. In our design, the linear CVA array has a total weight of 50 g including the SMA connector and the DPAs. The single DPA has a minimal effect on the overall array weight as it only weighs approximately 3 g. The overall weight of the total planar array is 200 g. The CVA arrays are mounted on a thin aluminum sheet with 0.8 mm thickness. Rectangular slots (gaps) with 5 mm width were created in the aluminum sheet to reduce the effect on the CVA return loss. By creating these slots, the aerodynamic air resistance is reduced relative to a solid sheet.

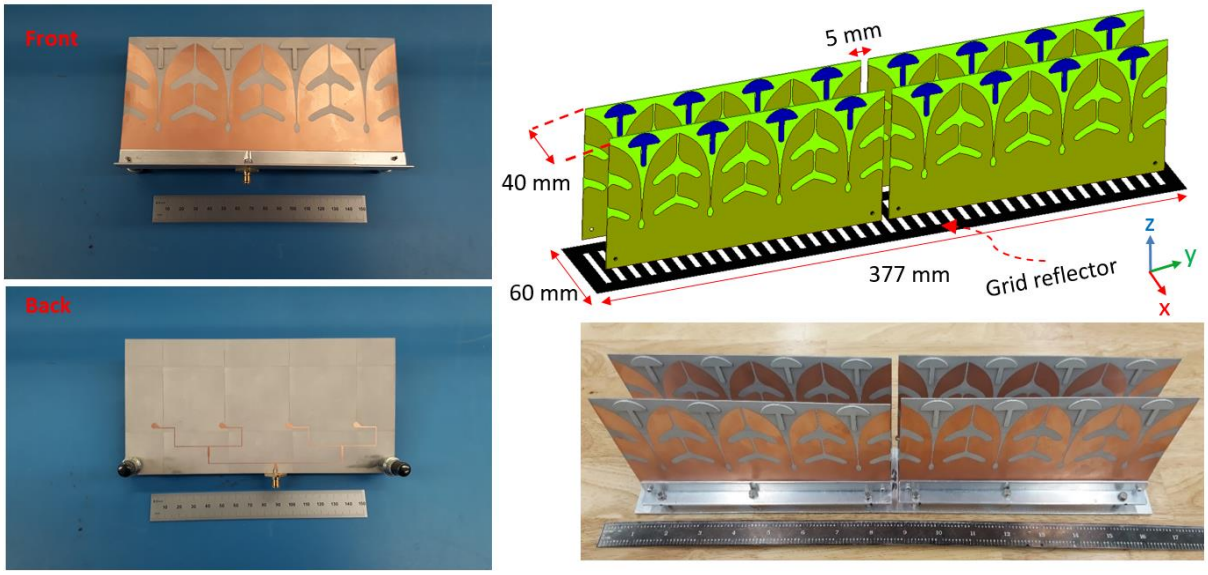

Figure. 3.21 The CVA arrays with the low-profile DPA.

The reflection coefficients of the CVA linear and planar arrays are shown in Fig. 3.22 (a). The multi resonances in the planar array are due to the presence of the external power divider and cables. The gain for the planar array is measured in the anechoic chamber after compensating for the insertion loss of the power divider and cables and it is varied from 15.2 and 24.6 dBi for the 8×2 planar array, as shown in Fig. 3.22(b). There is an excellent agreement between measurements and simulations. The radiation efficiency of the proposed array is more than 90 % over the entire operating frequency band.

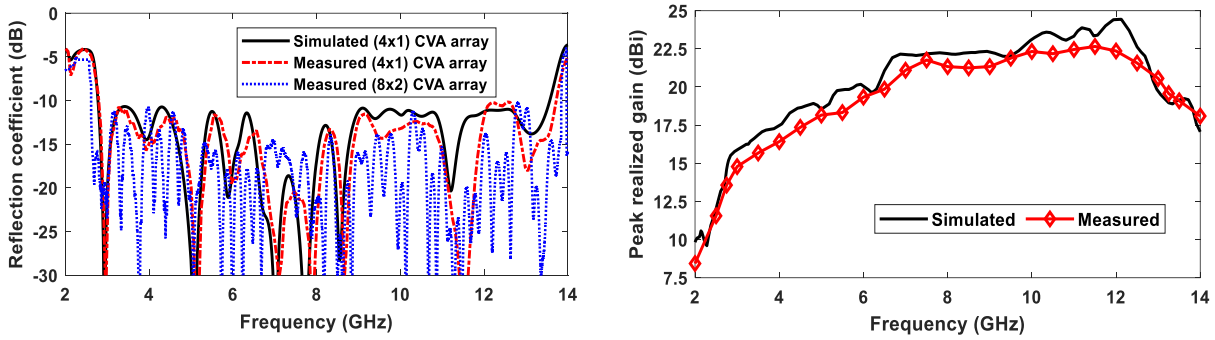

(a) (b)

Figure. 3.22 CVA arrays (a) reflection coefficients (b) total gain of the 8×2 planar CVA array.

Fig. 3.23 shows the radiation patterns with low SLL and grating lobes at higher frequencies, such as 12.5 GHz. The element spacing in the proposed CVA array is much greater than 0.5 λ at the higher frequency, which is the Nyquist sampling requirement to avoid the unwanted grating lobes [98]. This will also lead to an increase in the overall gain value as the gain is directly proportional to the antenna aperture area, while the associated grating lobes are kept below 10 dB using the DPAs to perform radar measurements.

Furthermore, the cross-polarization level is -25 dB at both planes through the entire band. The HPBW is varied from 13^{o} to 2^{o} and 60^{o} to 14^{o} for the E and H-plane, respectively. The F/B ratio is around 15-20 dB throughout the band.

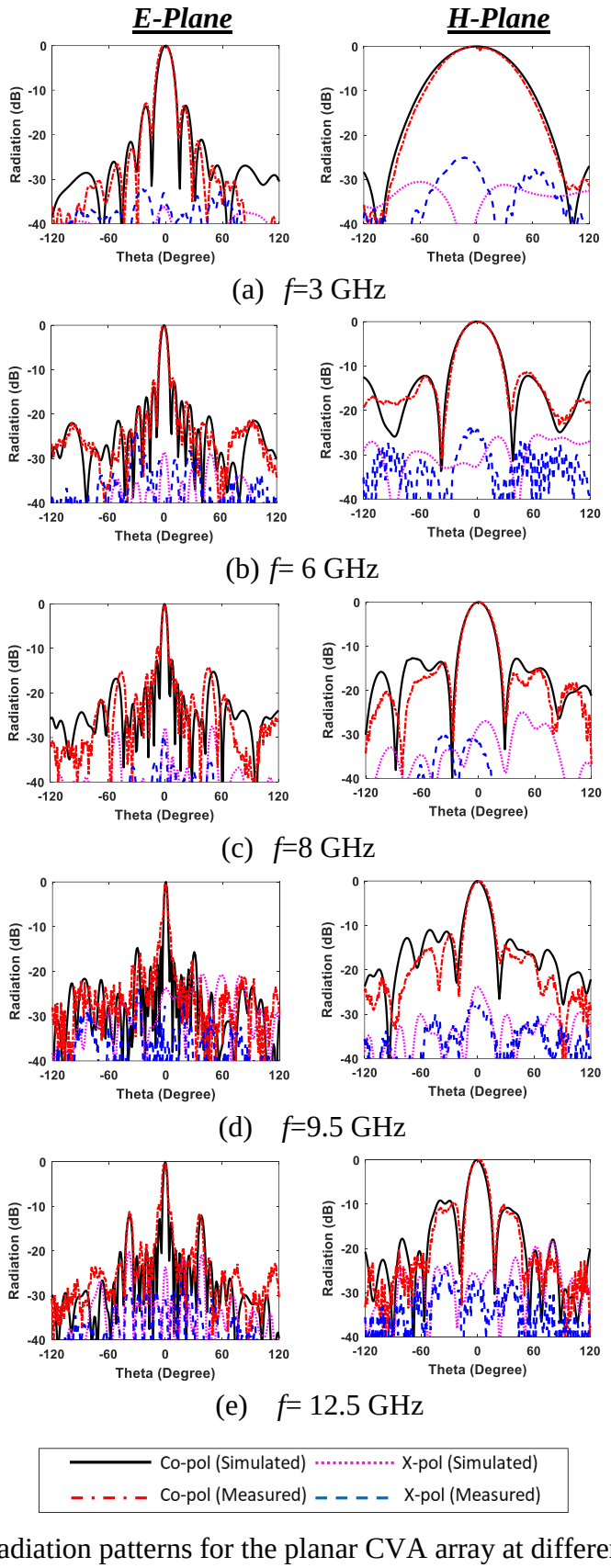

Figure. 3.23 Radiation patterns for the planar CVA array at different frequencies.

In radar applications, it is preferable to keep the F/B ratio as low as possible as in many cases the RF parts of the transmitter and receiver will be mounted on the back side of the antenna. The thin aluminum grid sheet at the back of the planar array improves the F/B ratio between 2-4 dB, as shown in Fig. 3.24. This improvement is similar to that obtained by Zhu et al. [101] by creating multiple defective structures in the AVA ground plane. However, the only difference in this design is that the F/B improvement is consistent throughout the entire band while it was achieved at the higher frequencies at the mentioned reference. Table I compares the proposed array with previous studies on this topic.

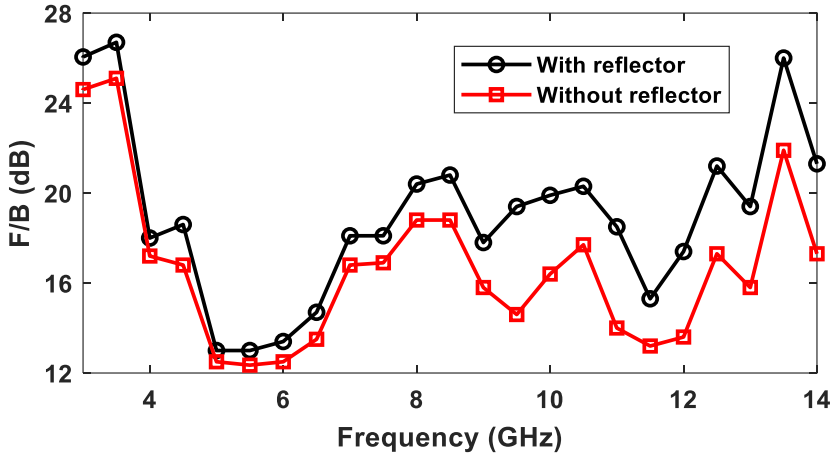

Figure. 3.24 Simulated front-to-back ratio for the planar CVA array.

Table. 3.1 Comparison between the CVA arrays and the literature

Ref.	Array type	Array volume (λ_{low}^3)	Material / Thickness (mm)	Frequency (GHz) / BW (%)	Gain (dBi)
[66]	AVA 8×1	2.3×4.8×0.06	PCB/ 0.787 mm	24.1-28.5 16.5%	9.3-12
[67]	AVA 8×1	2.3×4.5×0.04	PCB/ 0.508 mm	24.7-27.5 11.3%	12.3-12.9
[73]	AVA 8×1	2.3×4.9×0.06	PCB/ 0.787 mm	24.55-28.5 14.8%	6.9-11.3
[88]	CVA 8×1	0.84×1.9×0.006	PCB/ 1.57 mm	1.2-4.2 111%	9-16
[98]	CVA 8×8	1.2×1.2×0.75	Aluminum/ 1.7 mm	10-35 111%	10-20.6
[100]	CVA 8×8	0.8×0.8×0.7	Aluminum/ 4 mm	2-18 160%	7-25
[This work]	CVA 4×1	0.85×1.7×0.007	PCB/ 0.762 mm	2.77-13.6 132%	10.8-17.8
[This work]	CVA 8×2	0.85×3.5×0.37	PCB/ 0.762 mm	2.77-13.6 132%	15.2-24.6

3.4 Other Antenna Works

In this section, different antenna designs and configurations are presented. First, the CVA array is used to constitute a T-shaped array for the manned aircraft radar to perform snow depth measurements. In addition, a shared-slot aperture Vivaldi antenna array at the Ku-band is designed for the same purpose. Finally, a dual-band patch array is described for future radar work.

3.4.1 T-Shaped Section Vivaldi Antenna Array for Manned-aircraft Radar

The CVA array reported in the previous section is used to build an 8×4-element array for the manned aircraft radar's transmitter while a 16×2-element array is used for the receiver. The reason for selecting such a configuration is to obtain a small overlapped footprint of transmit and receive antennas. An 8×1 and 4×1 external Wilkinson power divider is used to combine the transmitter and receiver CVAs. The spacing between the CVAs is 40 mm. On the transmitter side, the edge elements were tapered to suppress the SLL at the H-plane up to -18 dB. Fig. 3.25 shows the simulated and fabricated arrays for the manned aircraft radar. The manned aircraft radar results were reported in detail in [102].

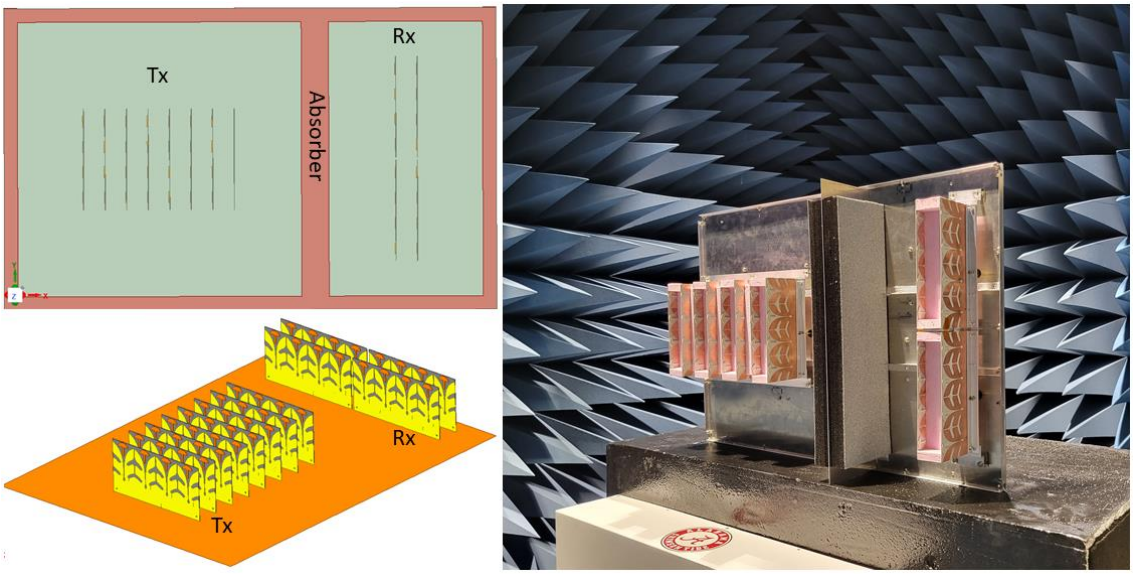

Figure. 3.25 T-Shape Mills-Cross antenna configuration.

The gain of the transmitter array is varying from 18 to 26 dBi over the frequency band of 2.77-13.6 GHz, while the receiver gain is similar to the UAV array in the previous section. The radiation patterns of the transmitter array at different frequencies are shown in Fig. 3.26. The narrow HPBW direction for the transmitter's side is orthogonal to the narrow HPBW of the receiver's array.

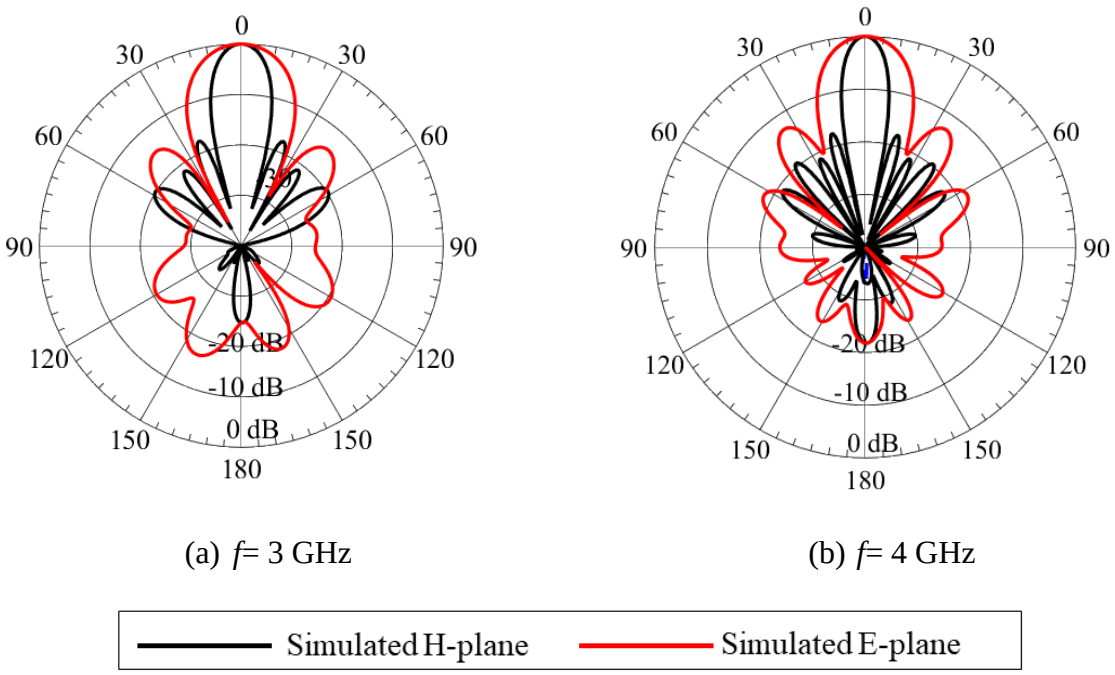

(a) f= 3 GHz (b) f= 4 GHz

Figure. 3.26 The transmitter array radiation patterns for manned-aircraft radar.

3.4.2 Dual-band Ku-band Patch Antenna Array

Dual-band antennas are widely used for many wireless communication applications such as low/high-speed up/downlink, where the lower band is used for up-link the data and the higher band is used for downlink. In addition, it is used to cover some of the WLAN, ISM, and Multi-Input-Multi-Output (MIMO) applications [103], [104]. Furthermore, a dual-band antenna can be designed to have two different operating modes in one design [105]. Creating the dual-band feature in a patch antenna can be utilized by many methods. First, by creating a slot in the patch geometry [106], [107] or by using a rectangular slot antenna with strips [108]. The slot shape and dimensions need to be adjusted to shift the second band to the required frequency range. This method has the advantages of simple design, and ease of fabrication, and does not require increasing the patch size to add an extra resonator. Another method is by adding an extra radiator with a small gap from the main antenna body [109]. As the antenna main body is radiating at the lower frequency band, the extra resonator will start to radiate at its resonance frequency through

the coupling with the main antenna part. In addition, using shorting pins has been reported for a multi-band antenna design [110]. Furthermore, Khaleghhi [111] proposed a dual-band antenna supported by a meander line for WLAN application. Herein, the single-element design is utilized using two identical substrates with the material of RO 5880 with a dielectric constant of 2.2 and thickness of 0.787 mm. The substrate dimensions are (20 × 20) mm^2. The microstrip line feeder is assigned at the lower side of the bottom substrate as shown in Fig. 3.27. A ground plane between both substrates is used to isolate the feeder from the patch antenna which is mainly to suppress the cross-polarization level. A via is used and passed through both substrates to excite the antenna while a circular aperture is created in the ground plane around the via with a radius of 1.2 mm. A thin rectangular slot with a dimension of W_s and L_s at the higher end of the patch antenna is created to generate the second resonance.

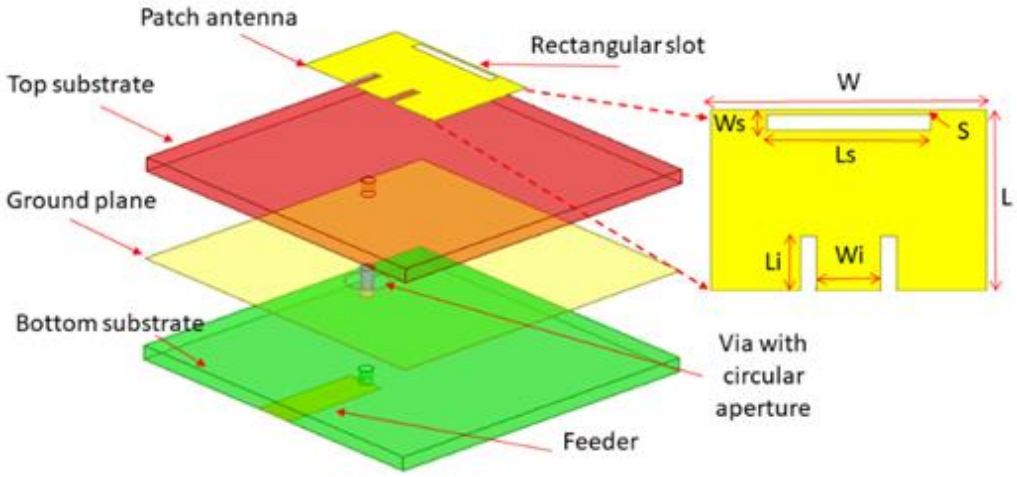

Figure. 3.27 Dual-band antenna single-element geometry.

Since the slot's dimensions and location with respect to the patch geometry control the second resonance, a parametric study is performed on the length, width, and location of the slot as shown in Fig. 3.28. It could be noticed that the length of the aperture shifts both resonances,

longer slot results in shifting the resonances to the lower frequency range. The width, however, didn't show a significant effect on the reflection coefficient. The location of the slot with respect to the patch's upper side (*s*) controls the first resonance, while the second resonance is not affected, as shown in Fig. 3.28 (c). This design as a result has the flexibility in changing the first or second resonance or both of them by changing the appropriate slot dimension.

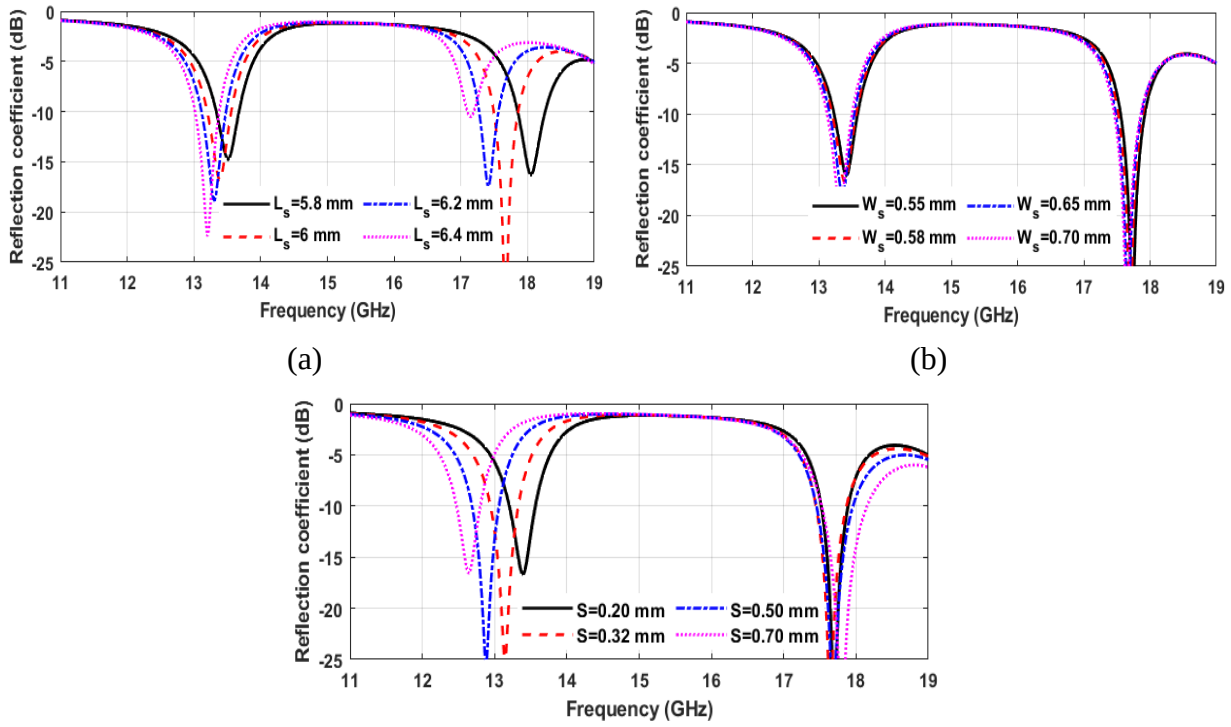

Figure. 3.28 Parametric study for the reflection coefficient of the single element.

In order to design the array, a sixteen-output ports Wilkinson power divider layout is designed as shown in Fig. 3.29. The power divider has a matching of -12 dB or better over the band from 11 to 19 GHz, and it has a better than -15 dB reflection coefficient over the two bands of interest, as shown in Fig. 3.30. The wide bandwidth of the power divider is preferred to prevent extra resonances that may result from the variation of the input impedance of the antenna with respect to the power divider output port. The isolation between any two adjacent ports is

better than -15 dB and is utilized by adding 100 Ω resistance to the power divider branches. The insertion loss is approximately 2-3 dB over the entire band.

The antenna single-element design is integrated with the power divider in one design as shown in Fig. 3.31. The overall dimensions of the array are 210×70×1.575 mm^3. A metal back reflector is added 5 mm below the array's lower side to suppress the back lobe and allow for mounting on the platform later on.

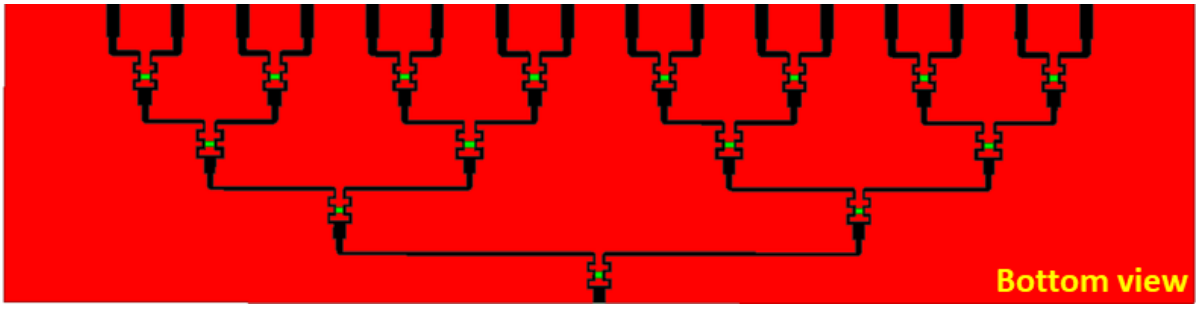

Figure. 3.29 Sixteen-port power divider layout.

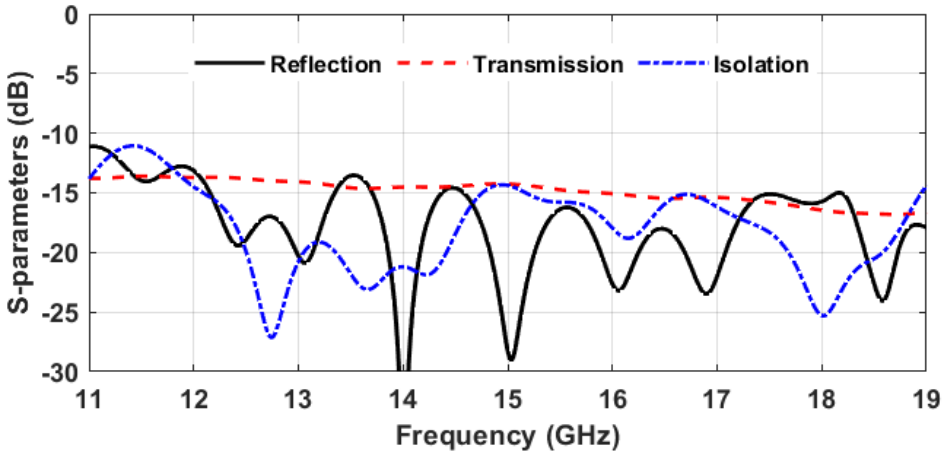

Figure. 3.30 Sixteen-port power divider s-parameters.

The reflection coefficient and peak gain of the proposed array are shown in Fig. 3.32. It could be seen that the two resonances at the 13 and 17 GHz frequency bands are matched with the 50 Ω output port of the power divider. The first and second resonances cover the frequency ranges of (12.53-13.17) GHz and (16.9-17.75) GHz with 4.98% and 4.9% fractional bandwidth,

respectively. At the center of the bands, the peak realized gain is approximately 17-17.5 dBi and it gets as low as 6 dBi at the isolation frequency band between the two operating bands.

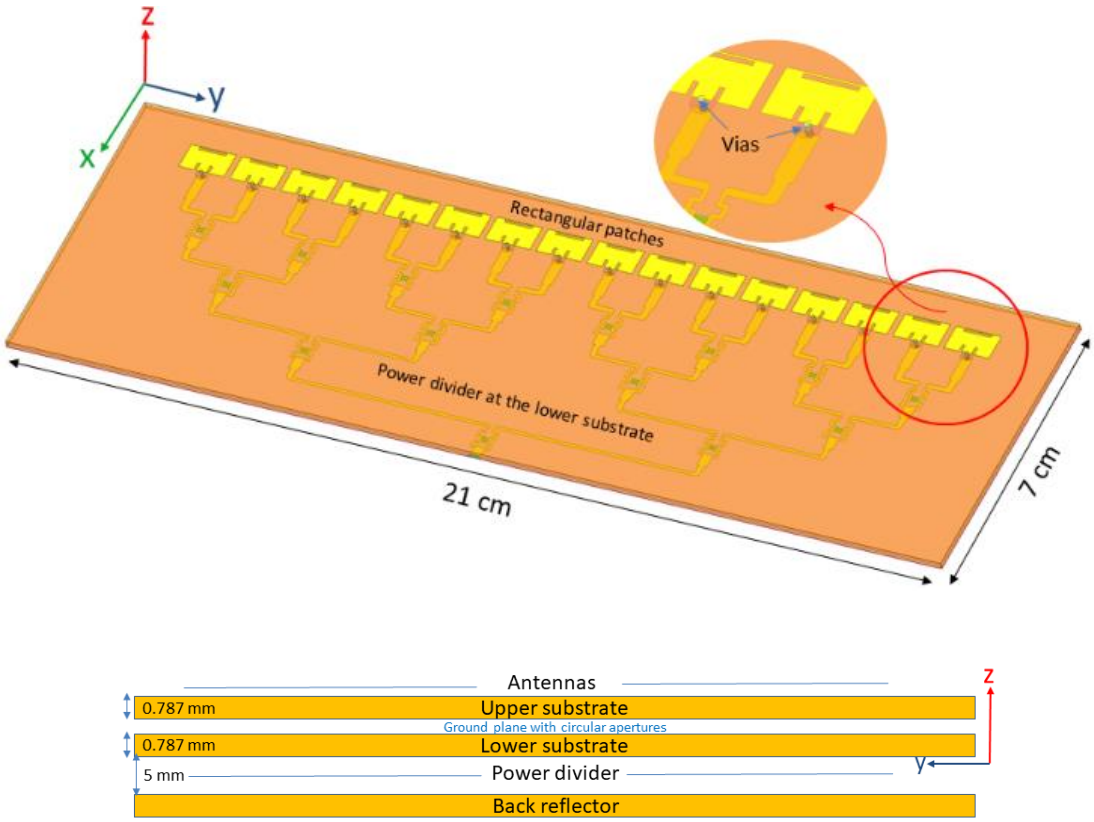

Figure. 3.31 Geometry of the dual-band patch antenna array.

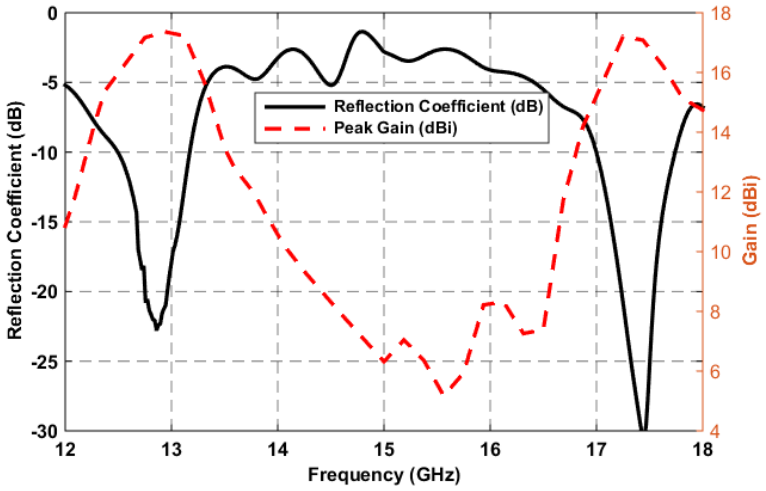

Figure. 3.32 Reflection coefficient and peak realized gain.

Fig. 3.33 details the array radiation patterns at the frequency band of interest. The E-plane HPBW is about 8° at the lower band and reaches to 5° at the higher one. The F/B ratio is better than 15 dB for the lower band and around 10 dB for the higher band. The cross-polarization level is better than -25 dB in both bands.

Two identical arrays are aligned in both vertical and horizontal directions to measure the mutual coupling between them, as shown in Fig. 3.34. It can be seen that both directions with 20 cm spacing have a mutual coupling of -40 dB.

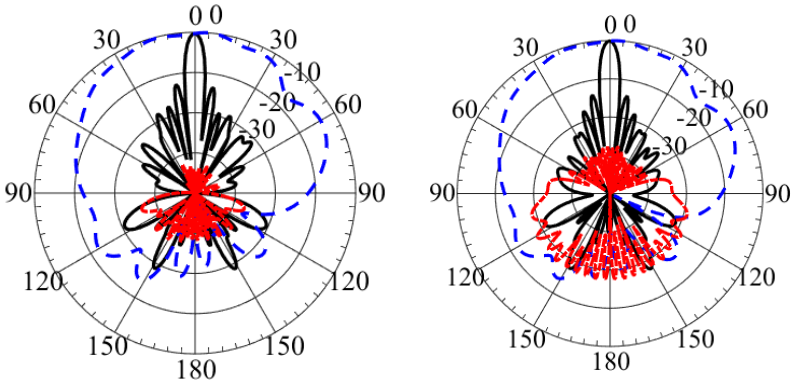

(a) *f*=12.7 GHz (b) *f*=13.1 GHz

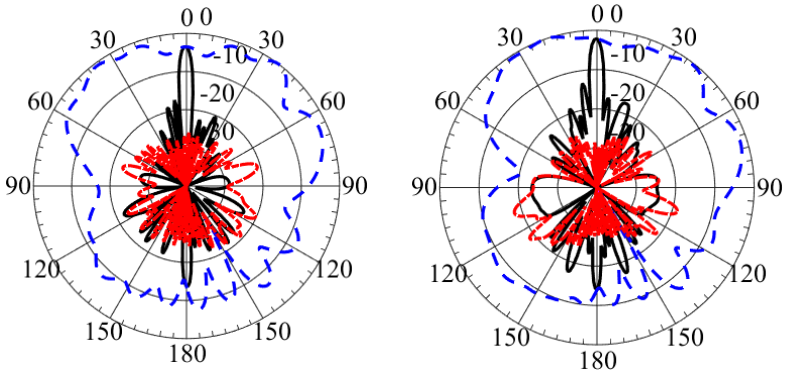

(b) *f*=17.1 GHz (b) *f*=17.6 GHz

Figure. 3.33 Radiation patterns at the two bands.

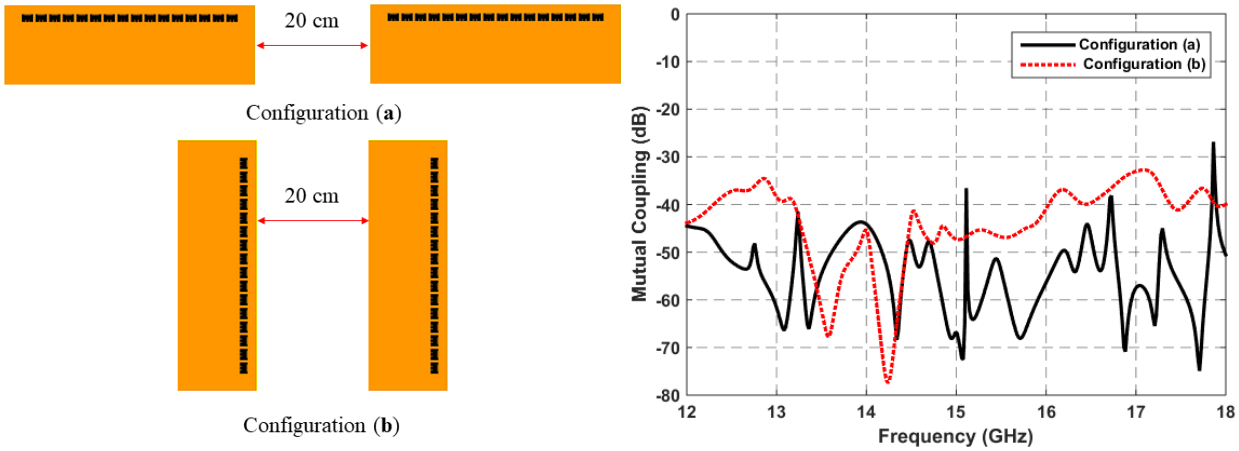

Figure. 3.34 Two identical arrays with different orientations and mutual coupling.

CHAPTER 4

RADAR SIGNAL PROCESSING

In this chapter, a description of the radar raw data structure is presented. Also, the algorithms used to process the data are presented including both focused and unfocused SAR. In addition, a correction for the transmit chirp non-linearity including phase and amplitude errors are shown. Finally, an auto tracker processor to track the snow top and bottom layers is described to generate a snow thickness map.

4.1 Radar Raw Data Collection Using the Data Capture Board

The radar raw data are collected with the DCA1000 (data capture board) from Texas Instruments (TI). The DCA1000 board is connected to the mm-wave sensors through a 60-pin high-speed cable as shown in Fig. 4.1.

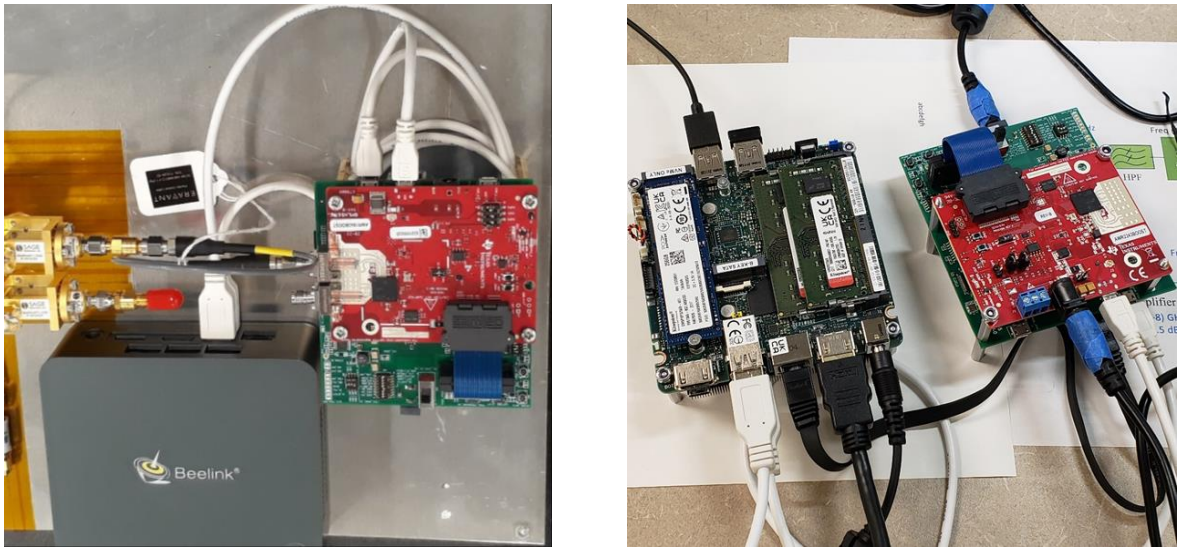

(a) (b)

Figure. 4.1 The computer connection with the DCA1000 and mm-wave boards (a) first radar prototype (b) second radar prototype.

The data are then stored in a mini-computer (PeeLink7) with 16 GB RAM and core i5 for the first radar prototype, as shown in Fig. 4.1(a). The computer's hard disk storage size is 256 GB with 4 USB ports and one Ethernet port. The mini-computer weight is approximately 1.7 lb. (0.77 kg). For the second radar prototype, we used a computer board manufactured by NUC with a total weight of 0.6 lb. (0.27 kg) including an external fan unit. The radar configuration is performed using TI interface software (mm-wave studio v2). There are a few jumpers on both boards (AWR1843 and DCA1000) that need to be configured before operating the radar. On the AWR1843 board, the S jumper should be configured as 001.

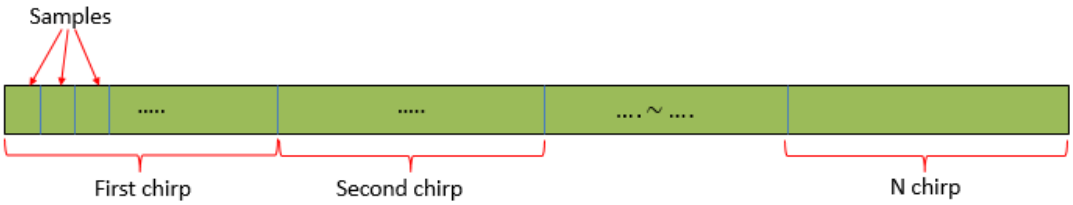

(a)

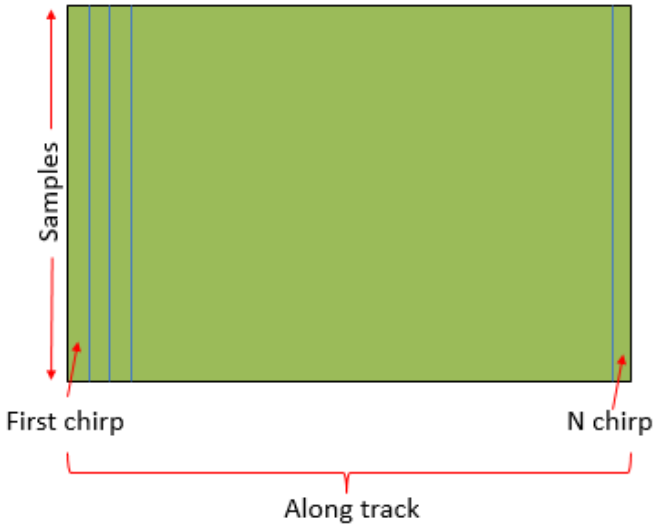

(b)

Figure. 4.2 The radar raw data structure (a) original binary file output (b) data in radar matrix form.

On the DCA1000 board, the 5-V jack power switch should be directed to the 5-V side. Once the power is connected, the orange and green LEDs on the AWR1843 will turn on and a green light on the DCA1000 left upper cornet will also turn on. This indicates that both boards are connected to the power source. For AWR1843, the S2 switch should be set to the SPI side while the SOP switch should be configured as SOP0 and SOP1 are "on" while SOP2 is "off". After these configurations are done the user should be able to connect to the device using the mm-wave studio. The host computer IP address should be 192.168.33.30 with a subnet mask of 255.255.255.0. The collected radar data are in binary files with a 1-GB size for each file. The radar will keep recording until the user stop the transmit signal or the computer storage is full. Most of the flights require 10-18 files based on the radar configuration, speed of the UAV, and the length of the flight. The binary file, however, needs to be read from a MATLAB interface to get the I&Q signals from the raw data. Fig. 4.2 shows a simplified block diagram for the initial data structure obtained from the radar. Then, we re-arranged the data into a matrix form to create the radar echogram. The matrix dimensions are arranged as; the number of samples (M) × the number of chirps (N). To fit the original format data into the matrix we subtracted a few chirps from the data line. In the radar matrix, the along-track distance (D) is given by:

$$D = v \times N \times \tau \tag{4.1}$$

Where v is the UAV flight speed in m/s, N is the number of chirps, and τ is the chirp duration in Sec. The y-axis of the radar matrix (range) is given by:

$$R = \frac{f \times c}{2 \times S} \tag{4.2}$$

Where f is the sampling frequency, S is the chirp rate. As the mm-wave evaluation board has multi-transmitters and multi-receivers, we selected the edge Tx and Rx antennas and connected them to our up/down converters. In Fig. 4.3, the software interface configuration is

shown where Tx2 and Rx0 are enabled. The physical locations of the transmitter and receiver antennas are shown in Fig. 4.3 (b).

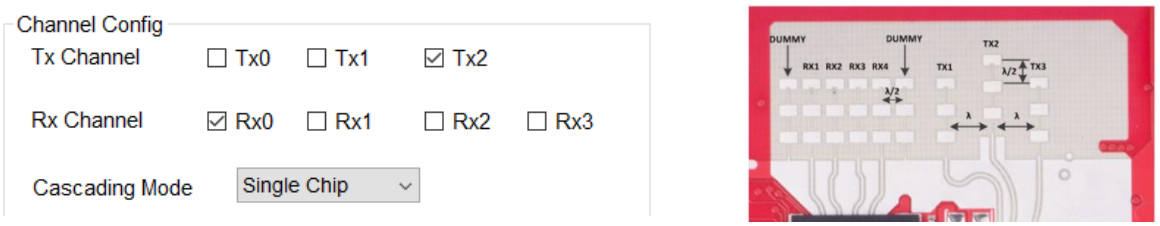

(a) (b)

Figure. 4.3 The evaluation board transmitter and receiver (a) software configuration (b) layout.

4.2 Unfocussed Synthetic Aperture Radar (SAR) Processing

After the data are collected, the data are imported and read from the binary files into a matrix. For initial processing, one chirp from the matrix (A-scope) is plotted to compare the link budget with the theoretical calculations. The impulse response of the radar-measured data at the nadir-looking angle over 100 m flight altitude is plotted in Fig. 4.4 over the lake surface.

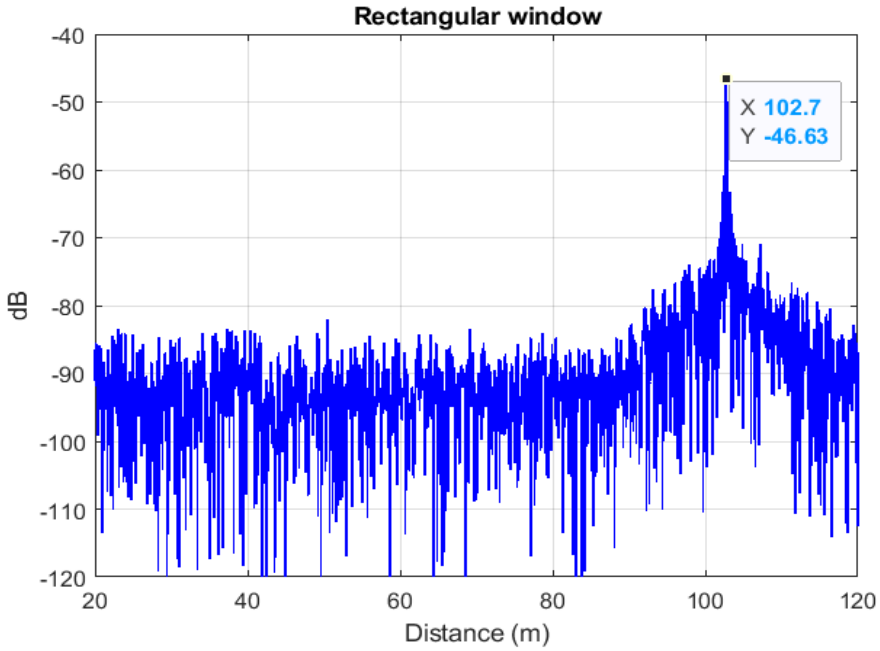

Figure. 4.4 Measured impulse response from the water surface at nadir-looking.

The chirp peak value is -47.42 dBm, which is close to the theoretical value for the radar (-46.05 dBm) that was shown in Chapter 2. The SNR is approximately 50 dB. Also, the raw data will be weighted by a Hanning window to suppress the SLL to -31.5 dB ideally instead of -13.5 dB for the rectangular window. This section's results are obtained using the first radar prototype with a 1.9 GHz bandwidth configuration shown in Chapter 2. The radar raw data are processed with focused and unfocused SAR algorithms to improve the SNR. In the unfocussed SAR, 3000 chirps are coherently integrated (CI) or averaged. The maximum number of chirps that can be averaged is given by equation (4.3)

$$\text{Max. number of averaged chirps} = \frac{AB}{v} \tag{4.3}$$

Where *A* is the illuminated area, *B* is the signal bandwidth and *v* is the UAV speed. Based on the calculation, the maximum number of averaged chirps is approximately 6000. However, to obtain a smooth radar echogram, only 3000 chirps are averaged coherently. This results in a 34 dB SNR improvement. Fig. 4.5(a) shows the impulse response for the optical delay line test with 62 dB total attenuation before and after the CI, where the theoretical 34 dB SNR is achieved. Fig. 4.5(b) shows the corner reflector impulse response for the nadir case where the SNR improvement is around 25 dB.

To generate the radar echogram, the collected raw data from the delay line test are used. The transmitter port is connected to the optical delay line and the receiver port is connected to the other end while the total attenuation is 62 dB which is equivalent to the free space loss for 100 m when subtracting the antenna's gain value. Fig. 4.6 illustrates the delay line echogram with the Hanning window and 3000 chirps coherently averaging. The point target at about 108 m and appears as a straight line. After the CI is performed, a few chirps, (4-7), will be averaged non-coherently to reduce the image speckle. After that, a median filter is applied.

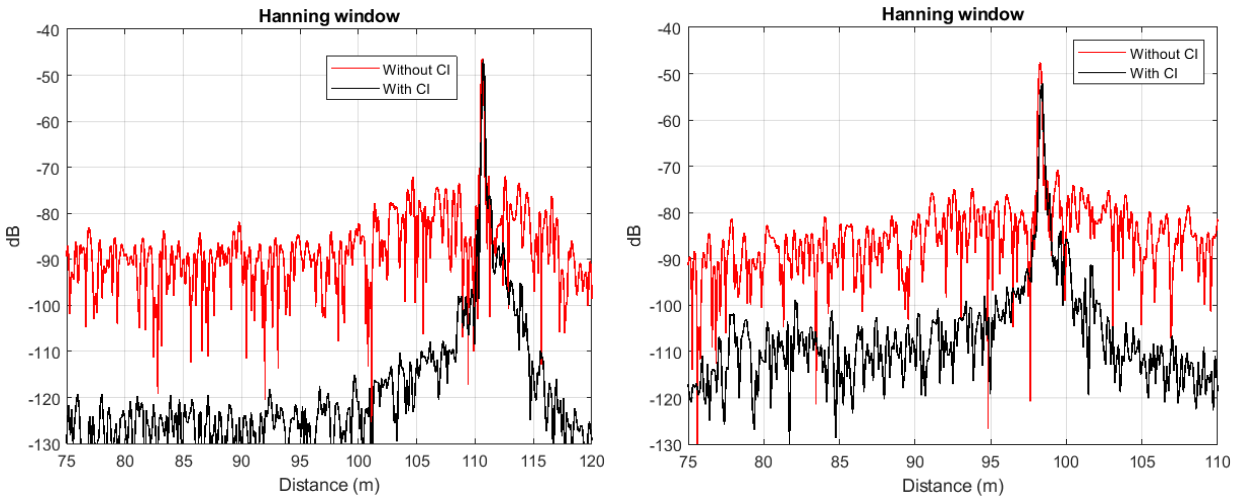

(a) (b)

Figure. 4.5 Radar measured impulse response (a) optical delay line (b) corner reflector.

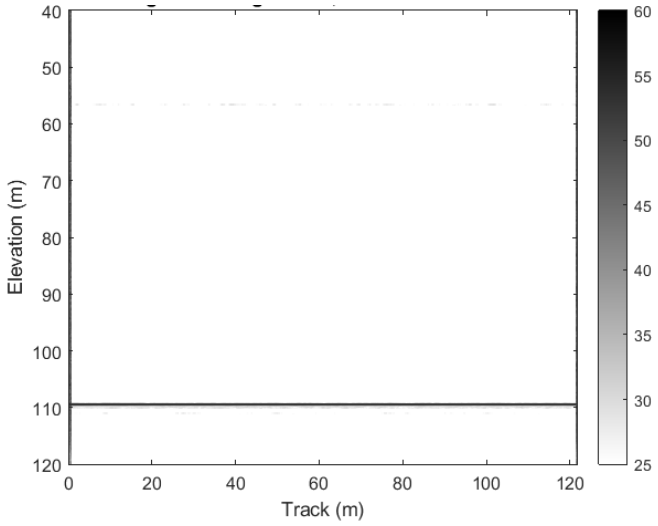

Figure. 4.6 Radar echogram using delay line data.

As shown before, the radar noise floor is at -90 dBm. Thus, to test the capability of detecting a signal lower than the noise level, an attenuation values of 100 dB and 112 dB were added to the delay line. This is equivalent to steering the antenna by 20-30 degrees. After that, the data were recorded and the impulse response is plotted in Fig. 4.7. It could be seen that even though the signal is at -95 dBm for the 112 dB total attenuation case, the CI still improves the SNR by approximately 30 dB.

In Fig. 4.8, A-scopes from the field results are shown for the nadir and off-nadir side antenna looking over a water body in Tuscaloosa, AL in 2021.

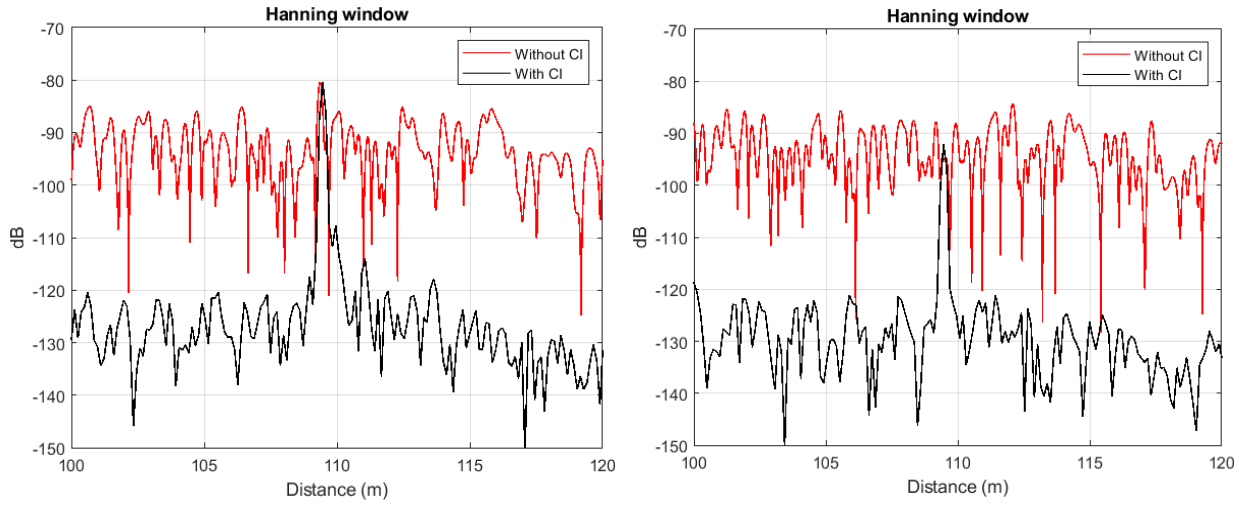

(a) (b)

Figure. 4.7 Measured delay line impulse response (a) 100 dB attenuation (b) 112 dB attenuation.

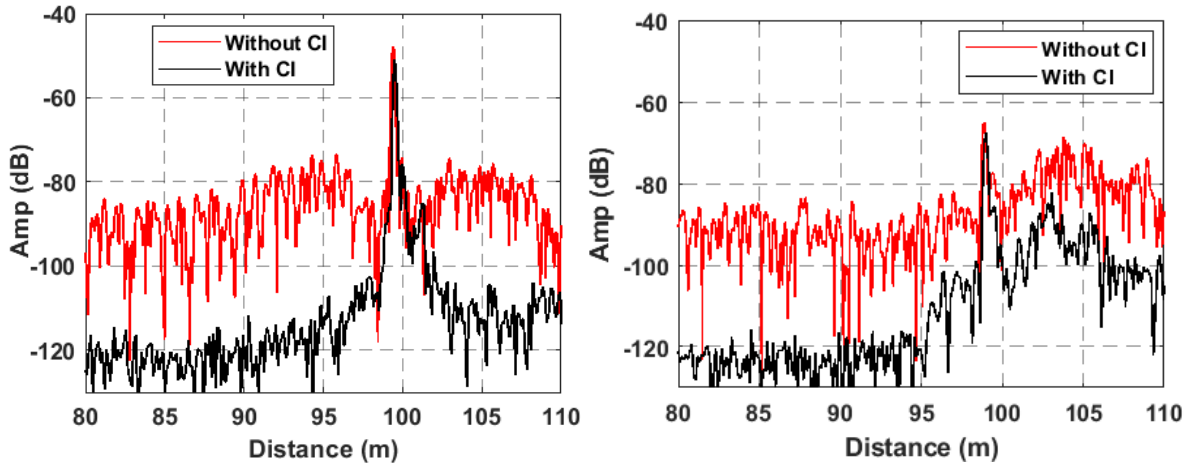

(a) (b)

Figure. 4.8 Measured impulse response over water (a) nadir (b) 20-degree off-nadir.

4.3 Focused Synthetic Aperture Radar (SAR) Processing

The radar data are also processed with a synthetic aperture radar (SAR) algorithm to obtain a 1-m along-track resolution and improve the SNR. C. Simpson, 2022 [112], described in detail a fully focussed SAR algorithm procedure for a UAV radar operating over 2-6 GHz and

used to measure soil moisture. Abushakra et al [113] used the same SAR algorithm developed by Simpson and used it to process this radar data for snow measurements in Colorado after tuning the processor to fit the radar data. SAR processing of the received signal narrows the beamwidth in the azimuth direction to improve the along-track resolution. The transmitter signal of an FM-CW radar can be expressed as [114-117]:

$$v_T(t) = V_o e^{-j(\varphi(t))}, -\frac{T_P}{2} \leq t \leq \frac{T_p}{2} \tag{4.4}$$

where $\varphi(t) = \omega_o t + \frac{\alpha t^2}{2}$ with α = chirp rate in rad/s and T_p is the chirp duration. The received signal is a time-delayed version of the transmitted signal with reduced amplitude and can be expressed as:

$$v_r(t) = KV_o e^{-j(\varphi(t-\tau))} \tag{4.5}$$

Herein, τ is the time delay. *K* accounts for spreading and attenuation losses. In FM-CW radar, the received signal is multiplied with a sample of the transmitted signal in a mixer (multiplier) and filtered to eliminate the sum frequency to generate the beat frequency signal (IF) (difference frequency) proportional to the target range. For an analytical signal, multiplying and filtering are equivalent to multiplying the received signal with a conjugate of the transmitted signal.

$$v_{IF}(t) = KV_o^2 e^{j[\varphi(t)-\varphi(t-\tau)]} \tag{4.6}$$

where,

$$\phi(t) = [\varphi(t) - \phi(t-\tau)] = \left[\alpha\tau t + \omega_o\tau - \frac{\alpha}{2}\tau^2\right] \tag{4.7}$$

We can neglect the 3rd term referred to as the residual video phase because $\tau << Tp$. The time delay to the target as the radar carrying platform flies by the target is given by:

$$\tau(x) = \tau_o + \partial\tau(x) = \frac{2R(x)}{c} \tag{4.8}$$

where τ_o is the minimum time delay when the target is located on the radar boresight and $\partial\tau(x)$ is the extra time delay associated with the radar carrying platform approaching and moving away from the target.

$$R(x) = \sqrt{R_o^2 + x^2} \tag{4.9}$$

where *x* is the along-the-track distance and R_o is the minimum -range to the target. For $x << R_o$, we can approximate *R(x)* as

$$R(x) \approx R_o + \frac{x^2}{2R_o} \tag{4.10}$$

The IF signal now can be expressed as a function of distance and time and then range migration is performed at the time domain. The signal is then passed through a filter with a frequency-domain transfer function given by:

$$H(K_x) = e^{j\frac{cR_oK_x^2}{4\omega_o}} \tag{4.11}$$

Fig. 4.9 shows a simplified block diagram for the SAR processor. The SAR main steps including motion compensation, range migration, and azimuth de-chirp are shown with their order in the processor. In Fig. 4.10 the 1-m side length trihedral corner reflector used for radar calibration is shown before and after SAR processing. The range hyperbola associated with the calibration target extending over a distance of 35 m is focussed to about 1-m spot.

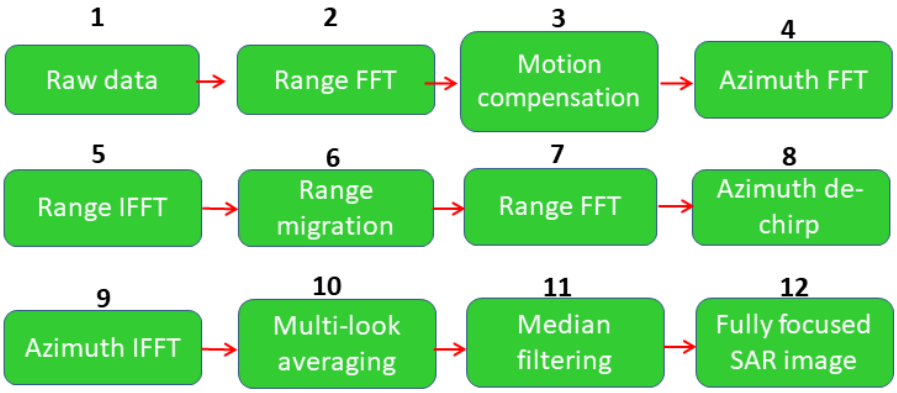

Figure. 4.9 Block diagram for SAR algorithm.

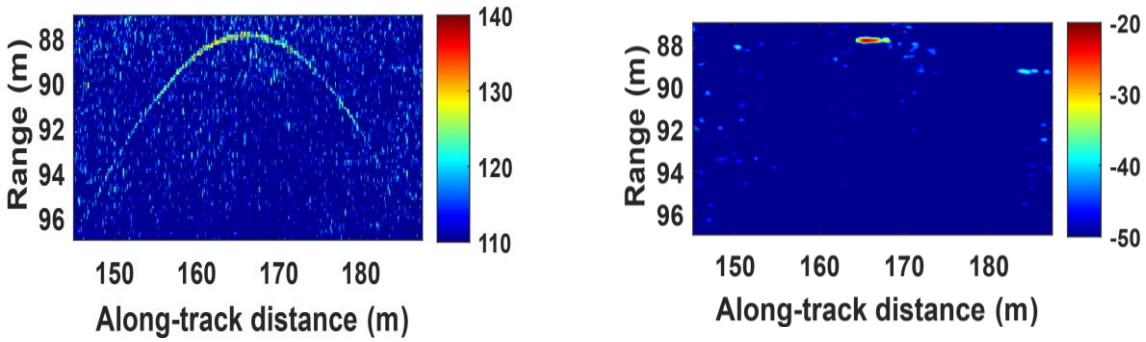

(a) (b)

(c)

Figure. 4.10 A sample echogram generated from the measured field data (a) corner reflector after FFT (b) corner reflector after SAR processing (c) trihedral corner reflector.

4.4 Chirp Non-linearity Correction

As we extended the radar bandwidth starting from 1.9 GHz to 4 GHz, the chirp no-linearity increased due to phase errors. The transmit signal is amplitude-modulated over this large bandwidth. The amplitude and phase variations cause spurious sidelobes. Peek [118] and Meta et al. [119] analyzed the effect of amplitude and phase errors on the FMCW radar response and provided an approach to correct for these errors. The FMCW radar IF signal can be modeled as follows (4.12):

$$y(t) = A_0[1 + ma(t)]e^{j\left(\pi\left(2f_0\tau + 2\alpha\tau t - \alpha\tau^2\right) + \phi(t)\right)} \tag{4.12}$$

where, $[1 + ma(t)]$, is the detected envelope of the IF signal, α is the chirp rate, τ is the delay time duration until the return signal arrives, *t* is the beat signal duration vector, f_0 is the chirp starting frequency, and $\phi(t)$ is the unwrapped phase error. To compensate for amplitude errors, the IF signal is multiplied by the inverse of the detected envelope of the IF signal. Amplitude corrections result in the suppression of symmetrical sidelobes caused by the amplitude modulation of the transmit signal.

Transmit signal phase errors are estimated using the procedure described by Peek [118] and Meta [119] using the radar response measured with a delay line or the corner reflector used for radar calibration. Then, the phase-corrected signal is passed through a de-skew filter to align the beat signal in time. The results are compared with an ideal impulse response as follows:

$$y_{ideal}(t) = e^{j\pi\left(2f_0\tau + 2\alpha\tau t - \alpha\tau^2\right)} \tag{4.13}$$

More details for this analysis are reported in our paper [113]. As can be seen in Fig. 4.11, after applying the above corrections in the post-processing, the main lobe is matched well with the ideal response. In addition, phase errors are suppressed. A full testing file is recorded and the

delay line echogram is plotted after correction. The echogram shows a very clean image with a strong peak in the range of 108 m. This advanced processing allows us to automate the tracking of surface and bottom interfaces for snow depth measurements.

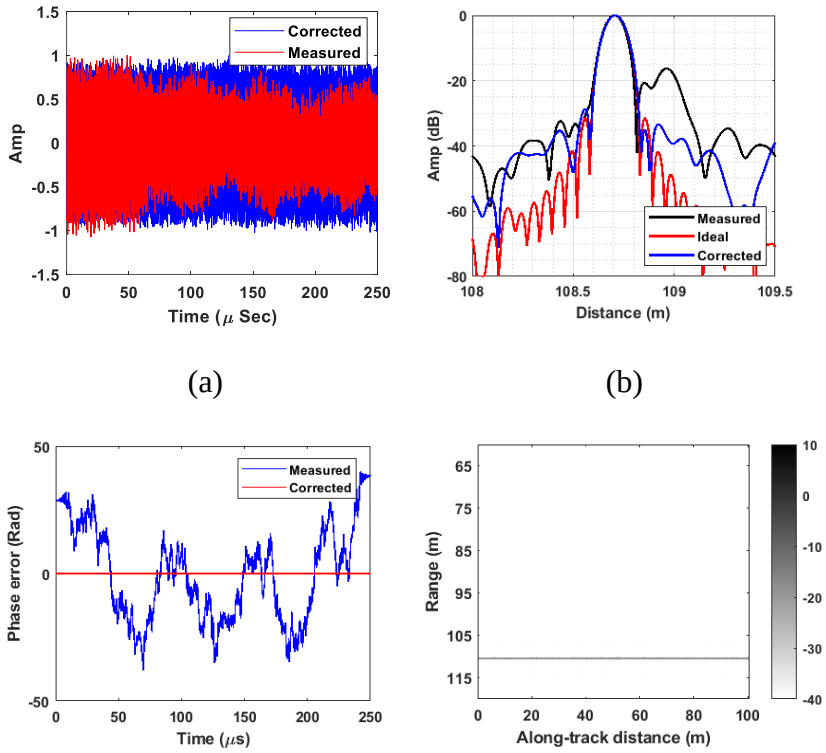

Figure. 4.11 The proposed radar chirp characteristics with phase and amplitude corrections (a) time domain (b) impulse response (c) phase error (d) delay line echogram after phase and amplitude correction.

4.5 Snow Map Tracker and GPS Correlation

To generate a snow thickness map, two important issues need to be addressed in the UAV radar. The first is to correlate the GPS data with the radar data. The GPS data are obtained from the UAV GPS module to obtain the altitude, yaw, pitch, and roll angles as well as the location. As mentioned in Chapter 2, the relay channel is added to turn on/off the amplifiers. Usually, the relay is turned on by the UAV pilot at 40 m height or more to prevent receiver saturation. In Fig. 4.12, the radar echogram at the UAV's start and end of the flight line is shown. At the take-off,

the relay channel is activated and the radar started to record. The GPS will start recording at the same time as it is synced to the same relay channel. Then, we interpolate the GPS data to fit the radar data. The second issue needed to generate the map is to detect the top and bottom of the snow, which are called air-snow and snow-ground interfaces. The difference between the two interfaces represents the snow thickness after correcting with the snow dielectric constant.

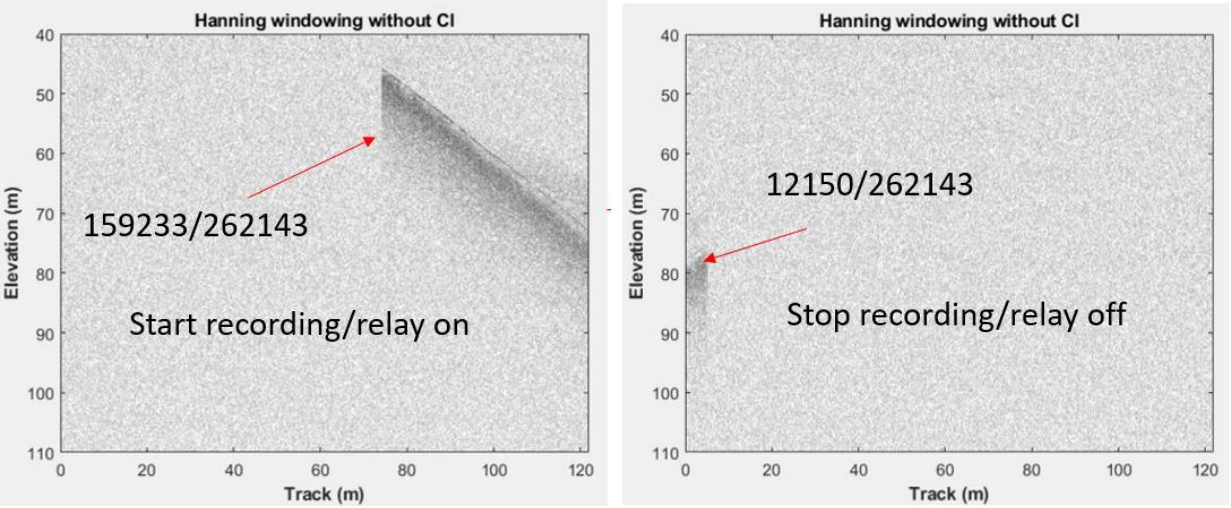

Figure. 4.12 The radar echogram at the relay on/off time.

CHAPTER 5

FIELD DEPLOYMENTS

In this chapter, a description of three main deployments for the UAV radars is presented. The two radar prototypes are tested in the field in Tuscaloosa, AL, and Grand Mesa, Colorado during the period between 2021 and 2023. The First radar prototype shown in Chapter 2 was deployed in the arboretum area at the University of Alabama, Tuscaloosa in 2021 for soil moisture measurements. We used the 1.9 GHz bandwidth signal with 10 dBm of transmit power.

Later on, in March-April 2022, the radar was deployed in Grand Mesa, Colorado for snow depth measurements. The selected location for the deployment contains about 2 m of snow. The radar bandwidth was extended to 3 GHz with transmit power of only 3 dBm. Finally, in 2023, the second radar prototype was deployed in Grand Mesa with 4 GHz bandwidth and 0 dBm of transmit power.

The main improvements achieved for the radar system for measurements in 2023 are weight reduction, size miniaturization, extending the bandwidth, and reducing the amount of transmitting power. High transmit power can result in a large directly coupled-through signal that generates the third-order frequency products at the receiver mixer. In addition, high transmit power increases interference to other nearby communication systems.

Table 5.1 summarized the three deployments' radars specifications and field experiment details. The flight's height and time were adjusted based on the field conditions such as altitude, air pressure, wind speed, and temperature. It could be seen that due to the height altitude of Grand Mesa, the flight time and height were reduced significantly compared to Tuscaloosa area.

The UAV operating team performed the field measurements including preparing the UAV's take-off point, in-situ measurements, and transferring the equipment to the test location.

Table 5.1 Radar field deployments summary.

#	Sep-2021	March-2022	Feb-2023
Deployment Location	Tuscaloosa, AL	Grand Mesa, Colorado	Grand Mesa, Colorado
Deployment purpose	Soil moisture	Snow measurement	Snow measurement
Radar weight (kg)	2.5	2.5	1.5
Up/down convertors Interface type	WR-12 (waveguide)	WR-12 (waveguide)	PCB (wire bond)
Max. Bandwidth (GHz)	1.9 (3.25-5.15)	3 (2.8-5.8)	4 (2.2-6.2)
Tx Power (dBm)	10	3	0
Chirp on duration (μs)	150	250	250
Chirp idle time (μs)	5	5	5
Radar box size (mm)	35 × 15 × 15	35 × 15 × 15	25 × 18 × 12.5
Antenna mutual coupling (dB)	55-60	55-60	55-60
Minimum detectable Rx signal (dBm)	-90	-90	-90
Flight altitude (m)	90-100	65-75	55-65
Avg. Flight time (min)	20-25	7-10	7-10

5.1 Radar Measurements over Soil

The radar's first prototype was used to collect data over the University of Alabama arboretum in Tuscaloosa as shown in Fig. 5.1. Several flights were performed with different antenna steering angles. During the flights, the wind speed was low with a calm lake that allowed us to increase the UAV height up to 100 m with a UAV speed of 3 m/s. The UAV with 5.5 lb. weight was able to fly up to 25 minutes. The radar data are processed with an unfocussed

Synthetic Aperture Radar (SAR) algorithm. Plotting the range profile history without the focused or unfocused SAR processing algorithms would have less SNR with fewer details in the radar echograms. Thus, the radar data are processed with an unfocussed Synthetic Aperture Radar (SAR) algorithm.

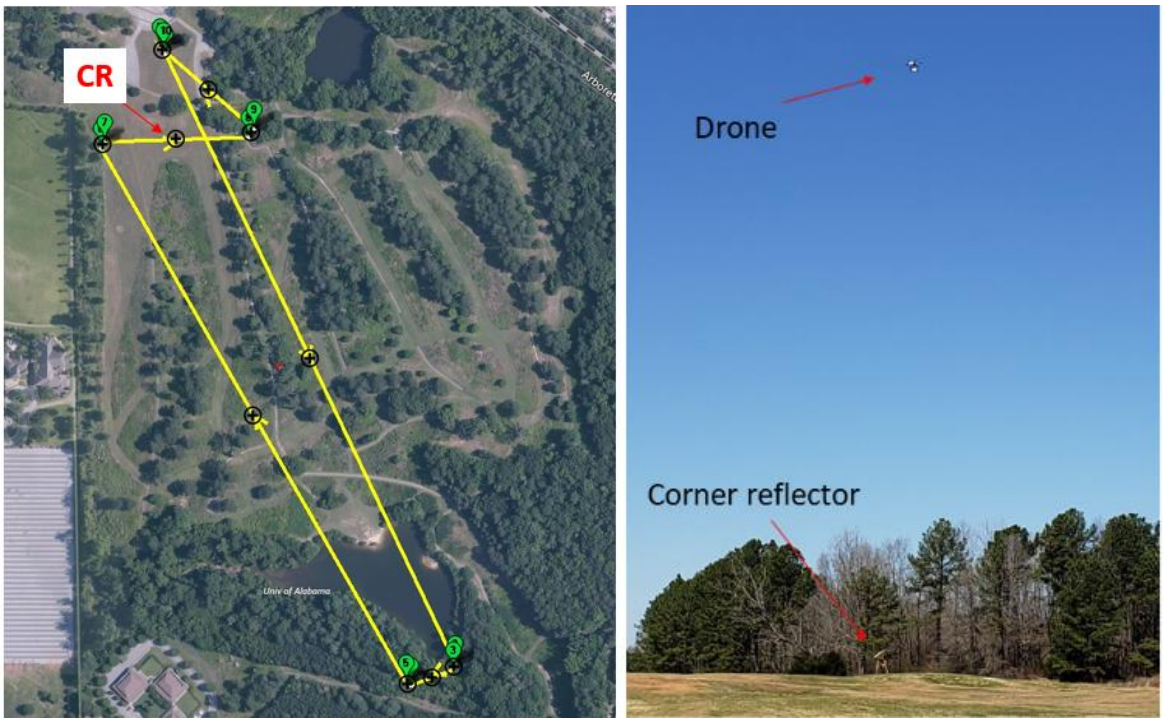

Figure. 5.1 UAV flight line over the arboretum area in Tuscaloosa.

In the unfocussed SAR algorithm, digitized radar data are averaged over an unfocussed aperture without phase corrections to obtain higher SNR over the flight region. The unfocussed SAR algorithm is utilized to obtain higher SNR over the flight region. To improve the SNR, a similar approach to what we described in Chapter. 4 is used here for the radar echogram where 3000 chirps are coherently Integrated (CI) after applying Hanning window. Furthermore, a few along-track samples are incoherently averaged and then filtered with a median filter to further improve image interpretability. Fig. 5.2 shows the echogram for the off-nadir antenna beam steering with 20^{o}. The flight line included trees, surfaces covered by short

grass, and a lake. This resulted in a very strong specular reflection and range sidelobes associated with radar response that can be clearly seen over the lake. The strong returns are from the sidelobes of the antenna from the lake. The strong returns are followed by backscatter over incidence angles between 20 and 30 deg. The aerial image of the flight path is shown in Fig. 5.3 to compare the truth area's details with the radar results. In addition, the radar resolution is sufficient to separate returns from vegetation and backscatter from the ground below the trees.

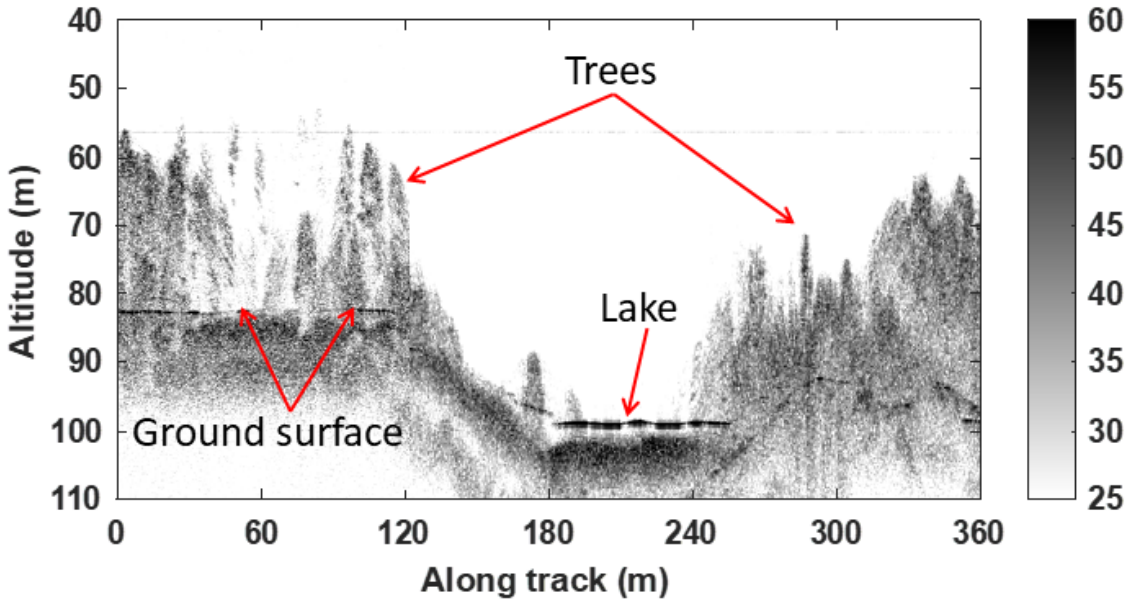

Figure. 5.2 Echogram for the flight line with twenty-degree steering.

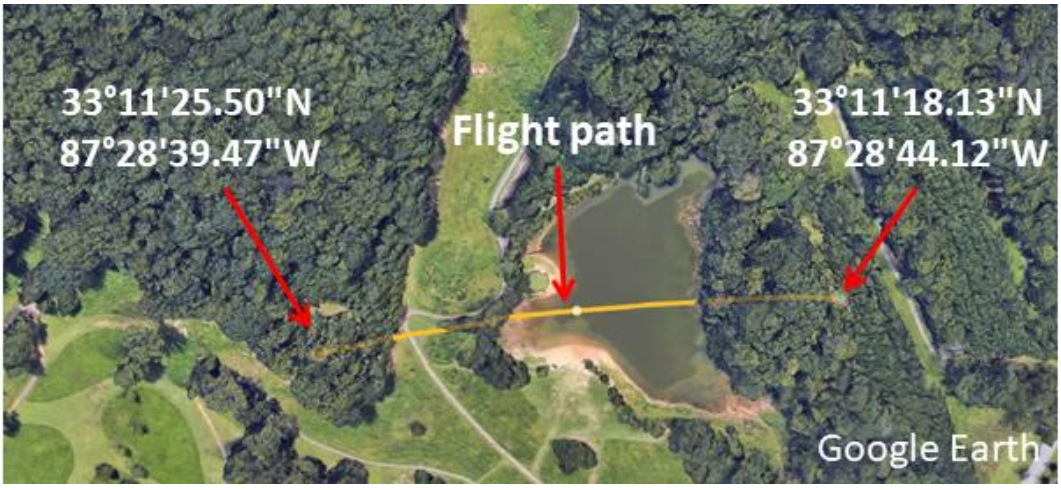

Figure. 5.3 Google Earth aerial image for the flight line.

5.2 Snow Measurements Deployment 2022

The field tests of the radar were performed in Grand Mesa, Colorado, during the period between 25th-March and 1st-April-2022. Three different locations are chosen to perform the radar flights to cover both forested and open areas as shown in Fig. 5.4. The radar flights are performed at 75 m altitude. The antennas were adjusted to point the antenna main beam vertically for snow depth measurements and spaced by 140 cm to achieve an isolation of 60 dB.

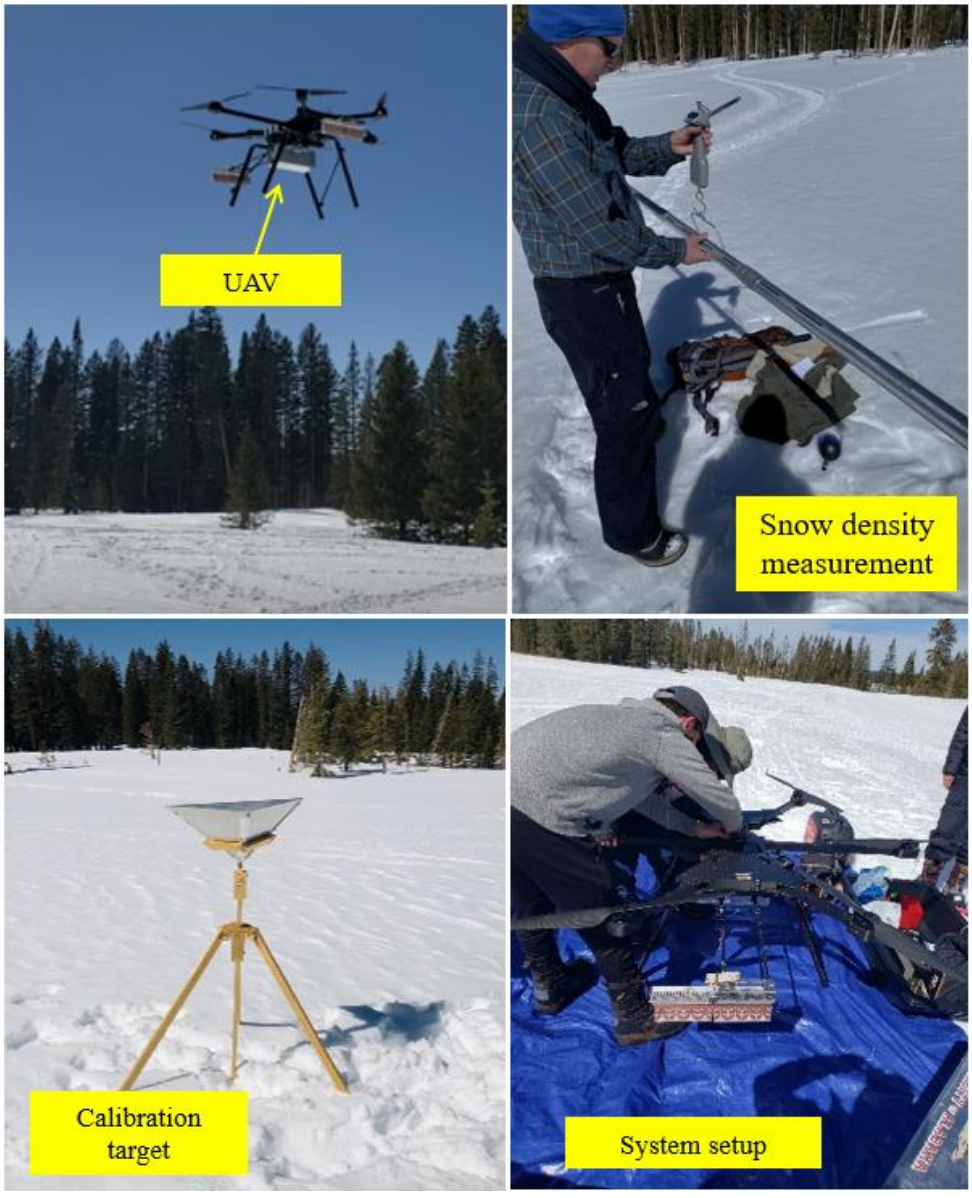

Figure. 5.4 Field measurements for the UAV radar for 2022 deployment.

Flight lines with a total length of 600-700 m for each flight were used to measure the snow depth in the area. The wind speed was about 3-6 m/s during the flights. The flight time was reduced to 7-10 minutes as the UAV batteries' discharge rate is greatly affected by the altitude of the area. For radar snow depth measurements, the distance between the air-snow and snow-land surfaces needs to be adjusted based on the snow dielectric constant. Thus a snow tube is used to measure the snow density (ρ_d) in the flight area which is basically a mass/volume ratio. At the location, it was found that the snow density varied between 0.27 and 0.31 g/cm^3 with a mean of 0.288 g/cm^3 after averaging several points. The snow density is used to calculate the dielectric constant of the snow (ϵ_s) which is given by (5.1) [120]:

$$\epsilon_s = 1 + 1.7\rho_d + 0.7\rho_d^2 + 8.7W_v + 70W_v^2 \tag{5.1}$$

where, W_v is the snow wetness that (0.02 - 0.025). Based on these measurements, the dielectric constant of the snow is found to be about 1.8. For the snow depth, it was measured using a 3 m avalanche pole at several locations to validate the radar data. The actual GPS points for the in-situ measurements were compared to the UAV GPS points. Measured snow depths in the survey area varied between 1.5 and 2.1 m. Fig. 5.5(a) shows the radar echogram generated after Fourier transforming the raw data before SAR processing where the air-snow surface can be clearly seen. The off-angle scattering from the snow surface and volume made the snow-land interface a little blurry. With a fully focused SAR algorithm, both interfaces become more clearly visible because of improved resolution and higher signal-to-noise ratio as shown in Fig. 5.5(b). Fig. 5.5(c) shows the corner reflector used as a radar calibration target is shown before and after SAR processing. The range hyperbola associated with the corner reflector extending over a distance of 35 m is focussed to about a 1-m spot.

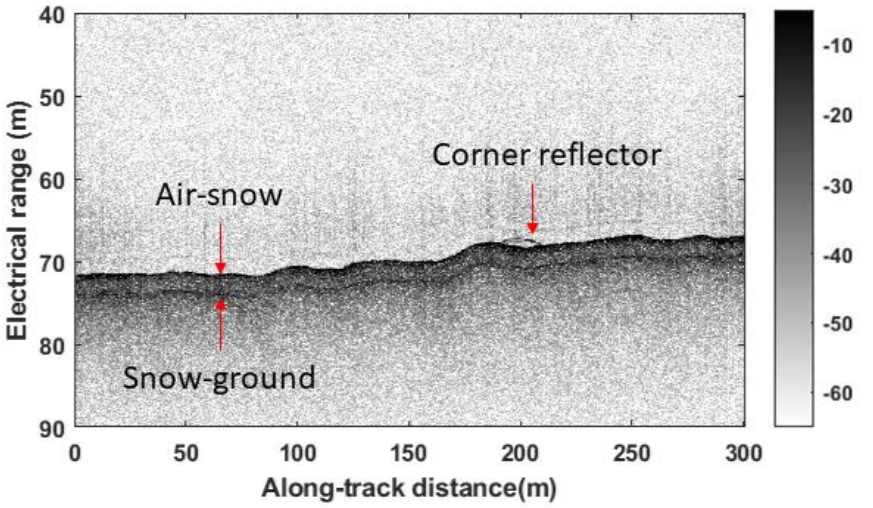

(a)

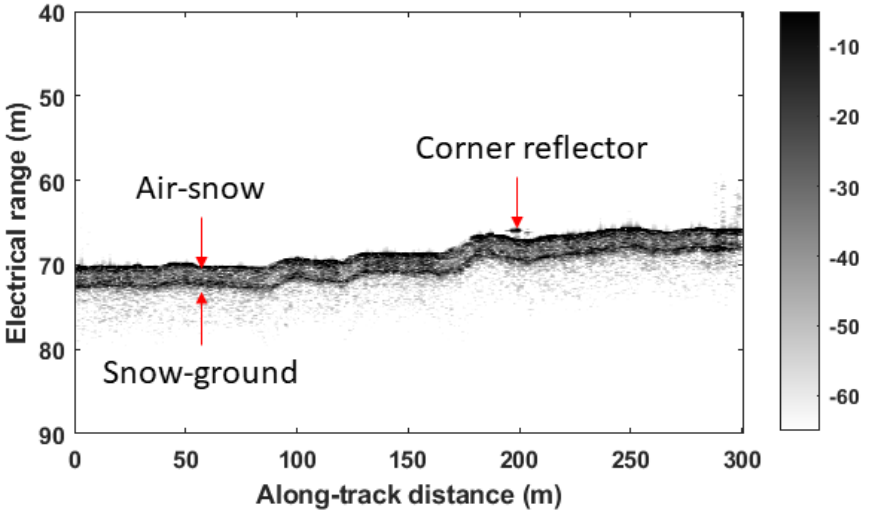

(b)

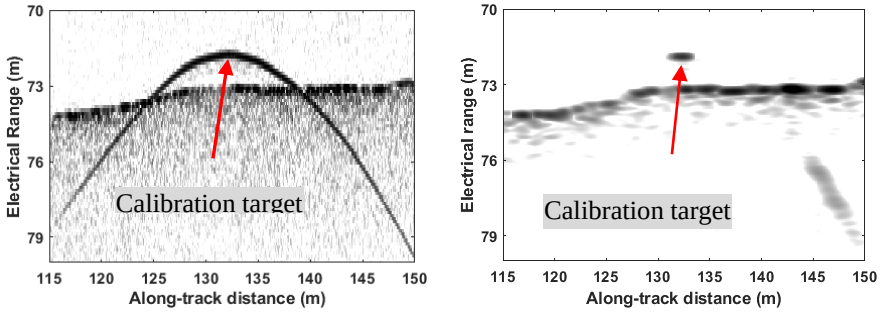

(c)

Figure. 5.5 Radar echograms for an open area (a) with FFT (b) after focused SAR (c) corner reflector before and after SAR.

Also, Figs. 5.6 and 5.7 show the radar echogram over an open area with light vegetation cover. Both top and bottom interfaces are clearly visible, with a small tress in the middle of the flight line. The estimated snow thickness varied between 1.5 and 2.1 over this flight line. Fig. 5.7(a), shows the flight line over the forested area with 20-25 m tall trees. The air-snow and snow-land interfaces are clearly seen under dense-tree cover.

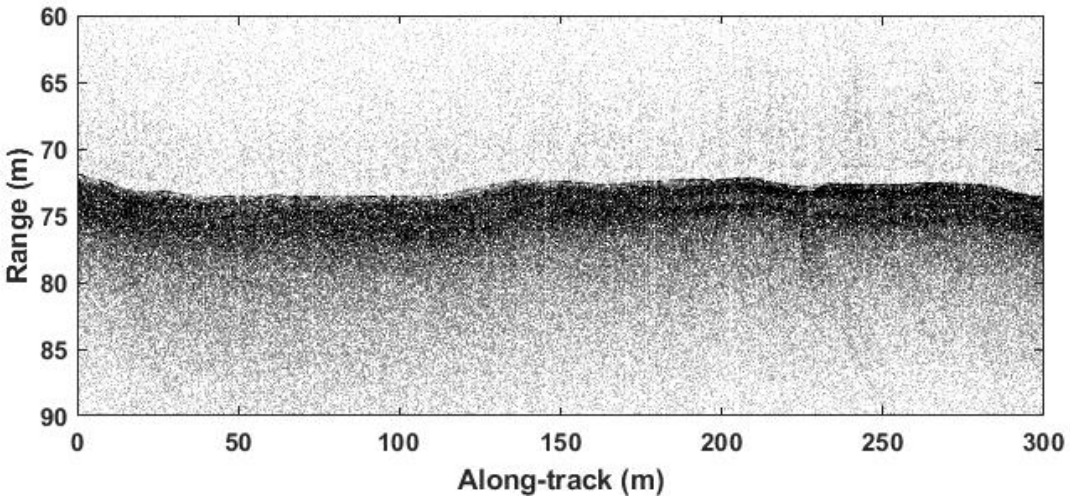

(a)

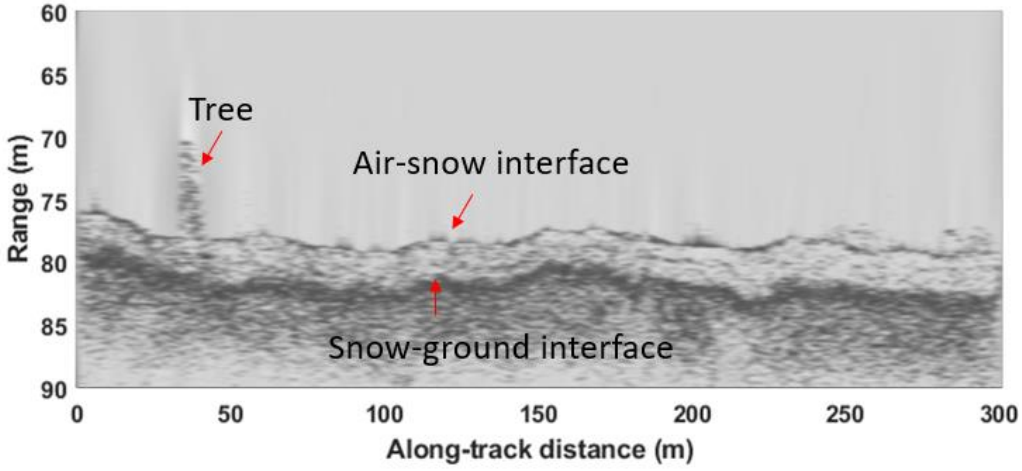

(b)

Figure. 5.6 Radar echograms for an open area (a) with FFT (b) after focused SAR.

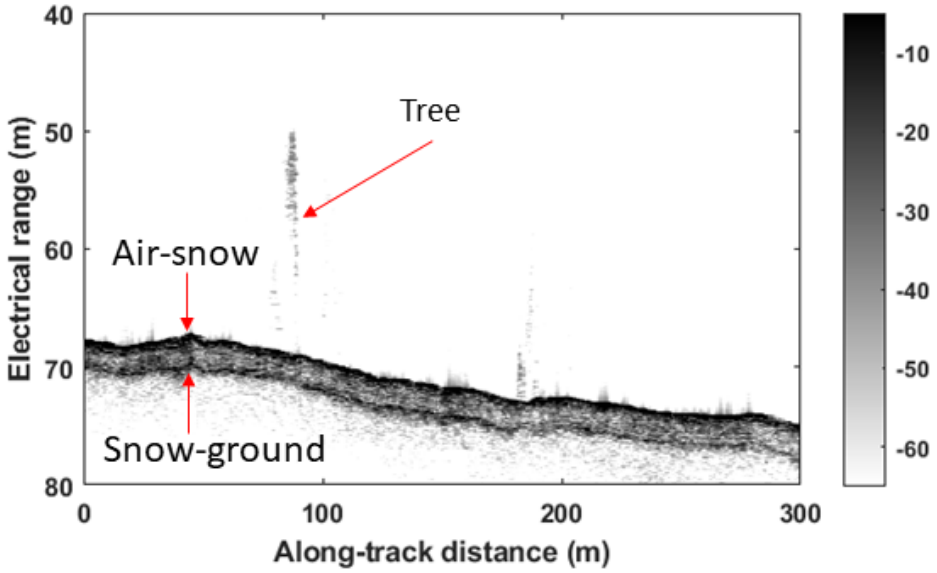

Figure. 5.7 Radar echograms for an open area with light vegetation.

To measure the actual snow depth, the electrical range is converted to actual snow depth using the measured snow dielectric constant from the in-situ measurements. Then, the altitude is normalized to simplify depth monitoring over the entire flight line, as shown in Fig. 5.8(b). It can be seen that the snow depth varied between 1.4 and 2.1 m over this flight line. In addition, the UWB radar with high sensitivity is found to be capable of mapping snow internal layers, which are generally isochrones that permit analysis of sub-seasonal snow accumulation rate on a regional scale. These internal interfaces are resulting from variations in weather conditions including wind, temperature, and snowfall rate, and are called sometimes snow-ice layers.

To validate the snow internal layers measured by the radar, a snow pit with a 1×1.5 m^2 area and a depth of 2 m was created at one point at the middle of the flight line to reach the ground surface, as shown in Fig. 5.9 which illustrates a flight line in an open area that shows two strong-return internal layers. The first and second layers are approximately located 60 cm and 120-140 cm underneath the air-snow interface, respectively. Both radar and in-situ

measurements are in good agreement for the internal layers inspection in the test area. Fig. 5.10 shows a full flight line of 600 m over the area of interest.

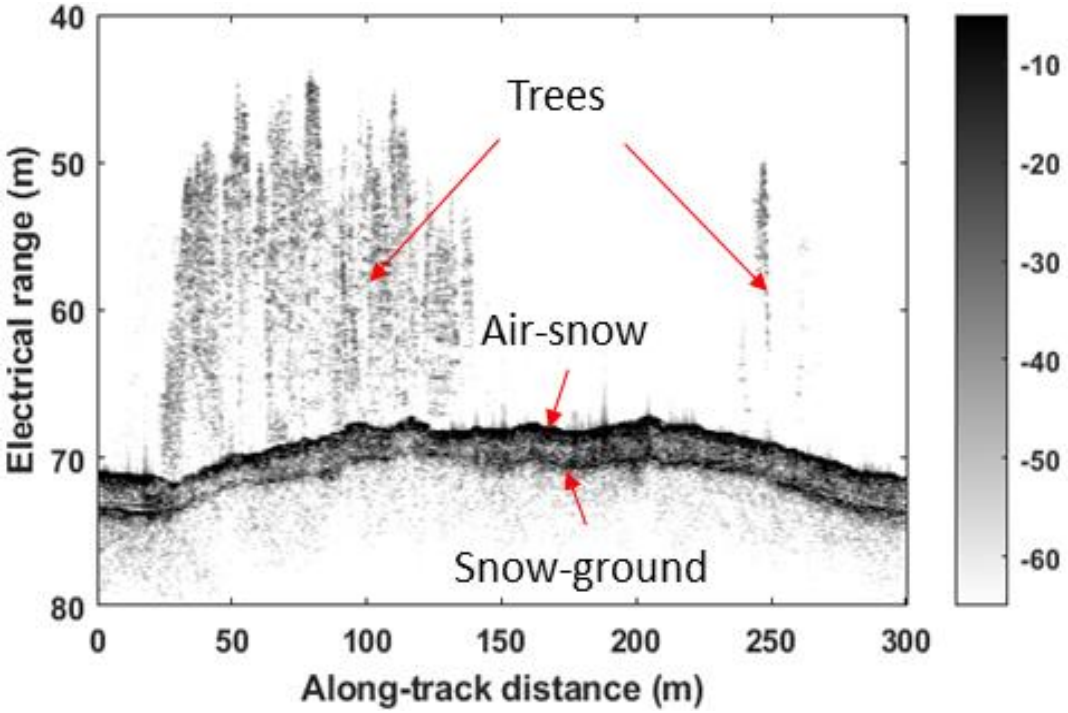

(a)

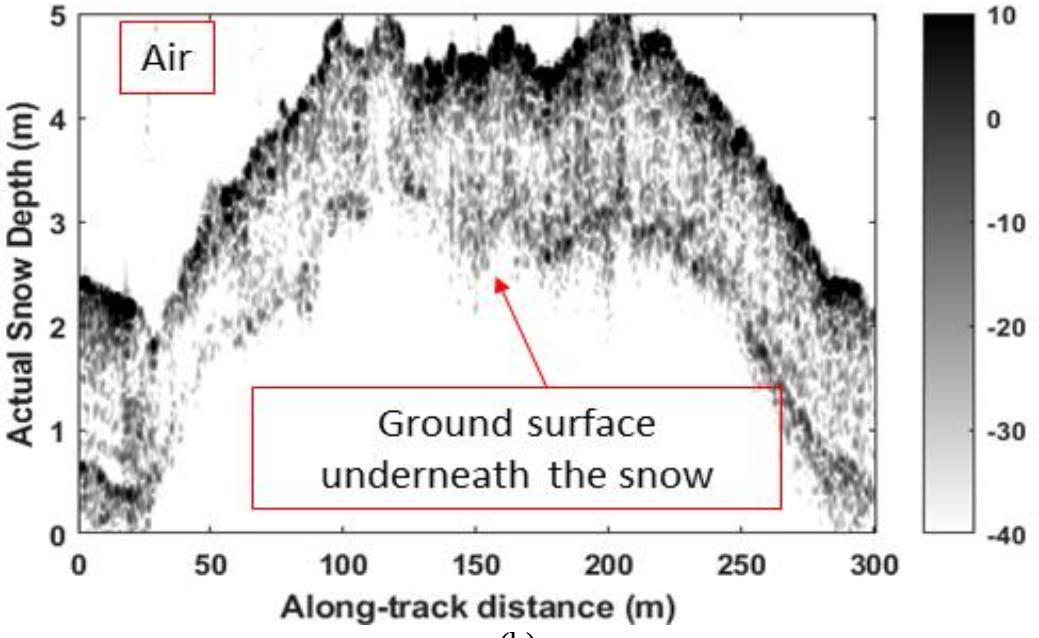

(b)

Figure. 5.8 Radar echograms for heavily-vegetated area (a) electrical range (b) true snow depth.

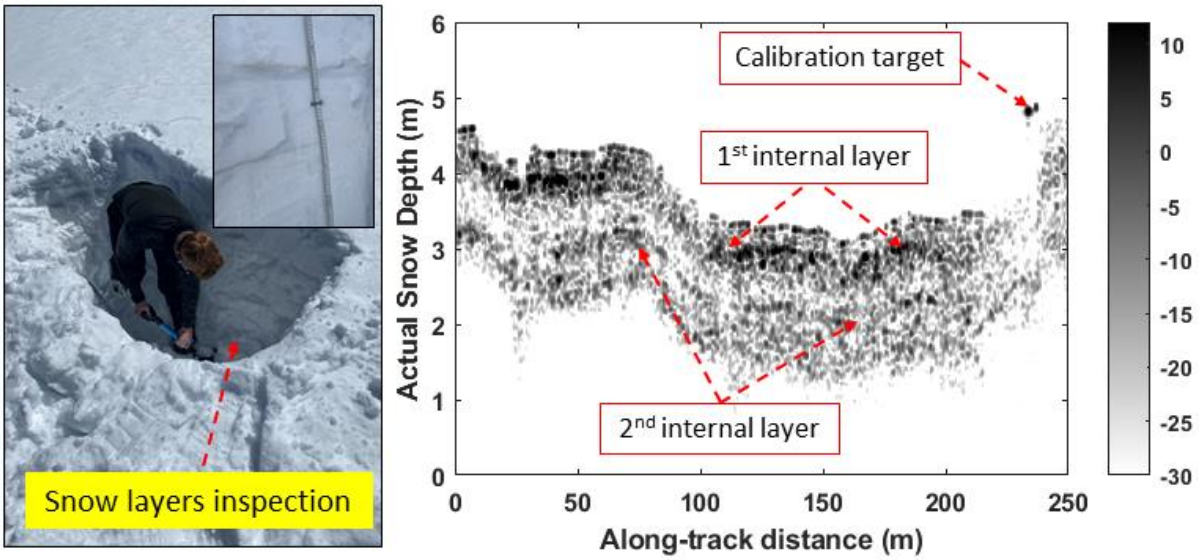

(a) (b)

Figure. 5.9 (a) Internal layers in-situ measurement (b) radar echogram shows the snow's internal layers.

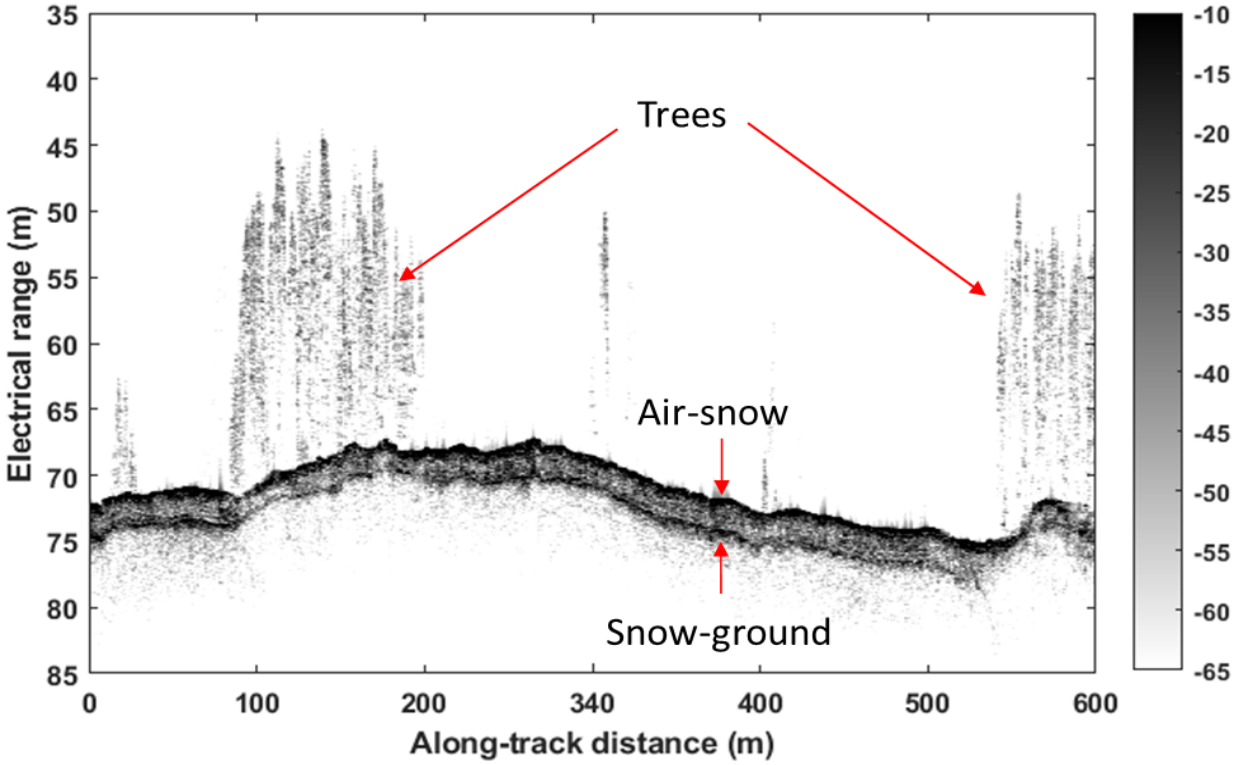

Figure. 5.10 A full flight line of 600 m length over the snow cover in 2022.

Fig. 5.11 shows one A-scope from the snow data. The phase and amplitude corrections show 3-6 dB improvements of SNR before the air-snow surface, while the SAR processor improves the SNR by approximately 35 dB while the maximum possible theoretical SAR processing gain is about 37 dB. The realized gain is within 2 dB of the maximum SAR processing gain. The small deviation from the ideal SNR improvement is caused by the rapid fall of coherent backscatter at the nadir and also by small phase errors introduced by UAV motion. The data reported here do not include compensation for motion-induced errors.

Identification of the top and bottom interfaces of the snow cover is the first step in the snow depth measurements. Thus, the automated layer tracker reported in Chapter 4 is utilized to quickly and reliably identify these two layers in post-processing. After the two layers are identified, the estimation of snow depth is calculated by taking the difference between the bottom and top interfaces and multiplying this difference by the range resolution. In addition, this range is corrected for the effects of the snow's dielectric constant.

The result is an estimation of the actual snow depth for each chirp in the flight line as shown in Fig. 5.12. In this line, a frozen lake covered by 2 m of snow is seen. Three short flights in a grid pattern over the region of interest were performed over an open area of 300×150 m^2. Then, the data of each flight line are tagged with the GPS data and then the automatic snow tracker is applied to estimate the snow depth.

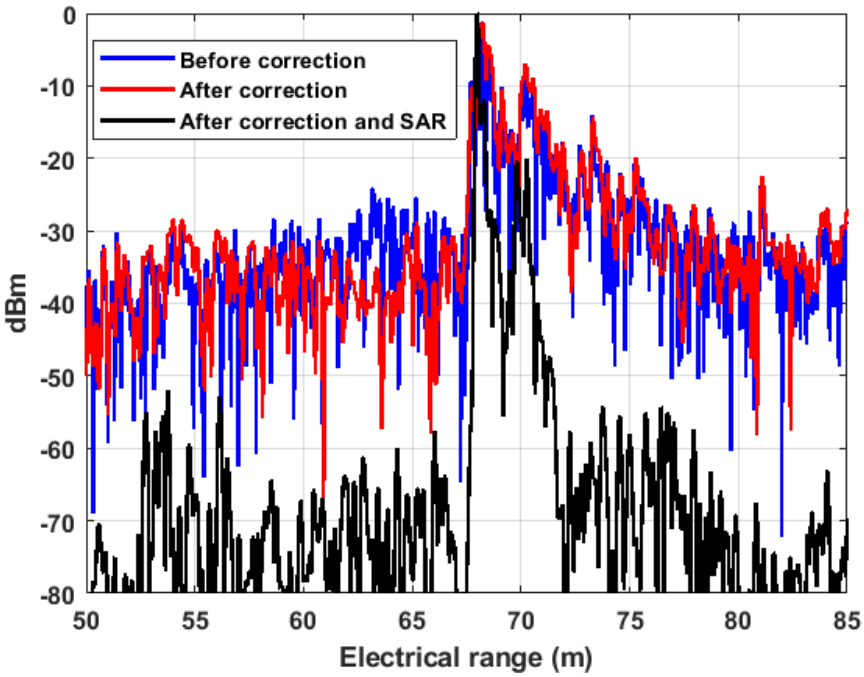

Figure. 5.11 A-scope from the measured snow data before and after chirp corrections.

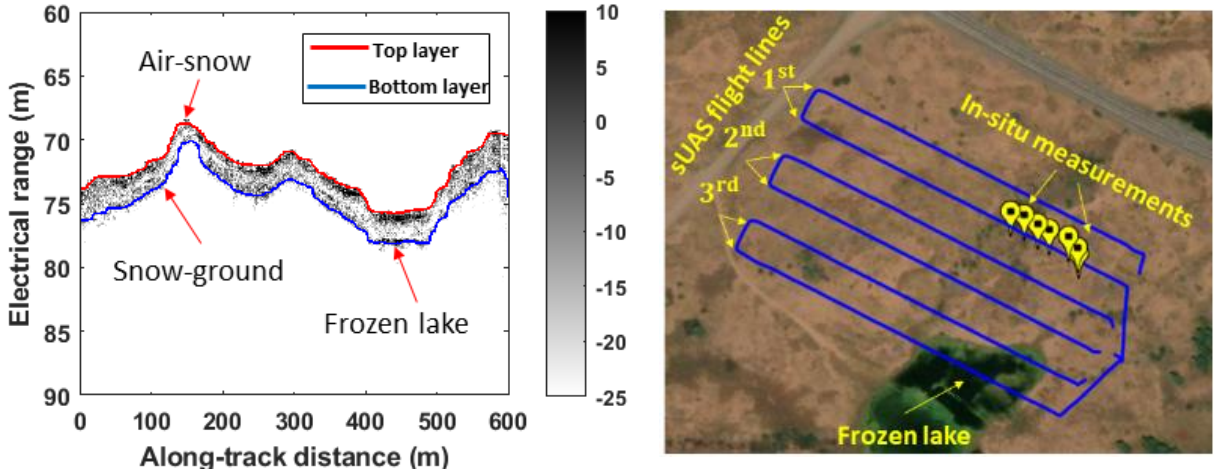

(a) (b)

Figure. 5.12 (a) snow tracker top and bottom layers (b) UAV flight grid pattern.

The depth estimation is performed individually for all flight lines in the grid pattern. Once the estimation of every flight line is completed, the depth and position data for each flight line is loaded and concatenated. A meshgrid is formed from the conglomerated position and depth data. This meshgrid is finally plotted on a satellite image of the region of

interest. The result is a webmap display of the snow depth distribution over the area of interest as shown in Fig. 5.13. From the snow map, the snow depth with the position is seen. The snow depth exceeds 2 m, in some areas while in other areas it is about 1.3 m only, which is mainly depending on the surface terrain where it is more likely for the snow to accumulate in the lower areas relative to the higher ones. The total time needed to generate this map is approximately 4 hours.

Fig. 5.14, shows the comparison between the in-situ measurements and the radar measurements for the snow depth at the same GPS points. It can be seen that the variation is about of ± 10 cm. Due to the difficulties in reaching the area, the in-situ measurement points were limited to a small number only.

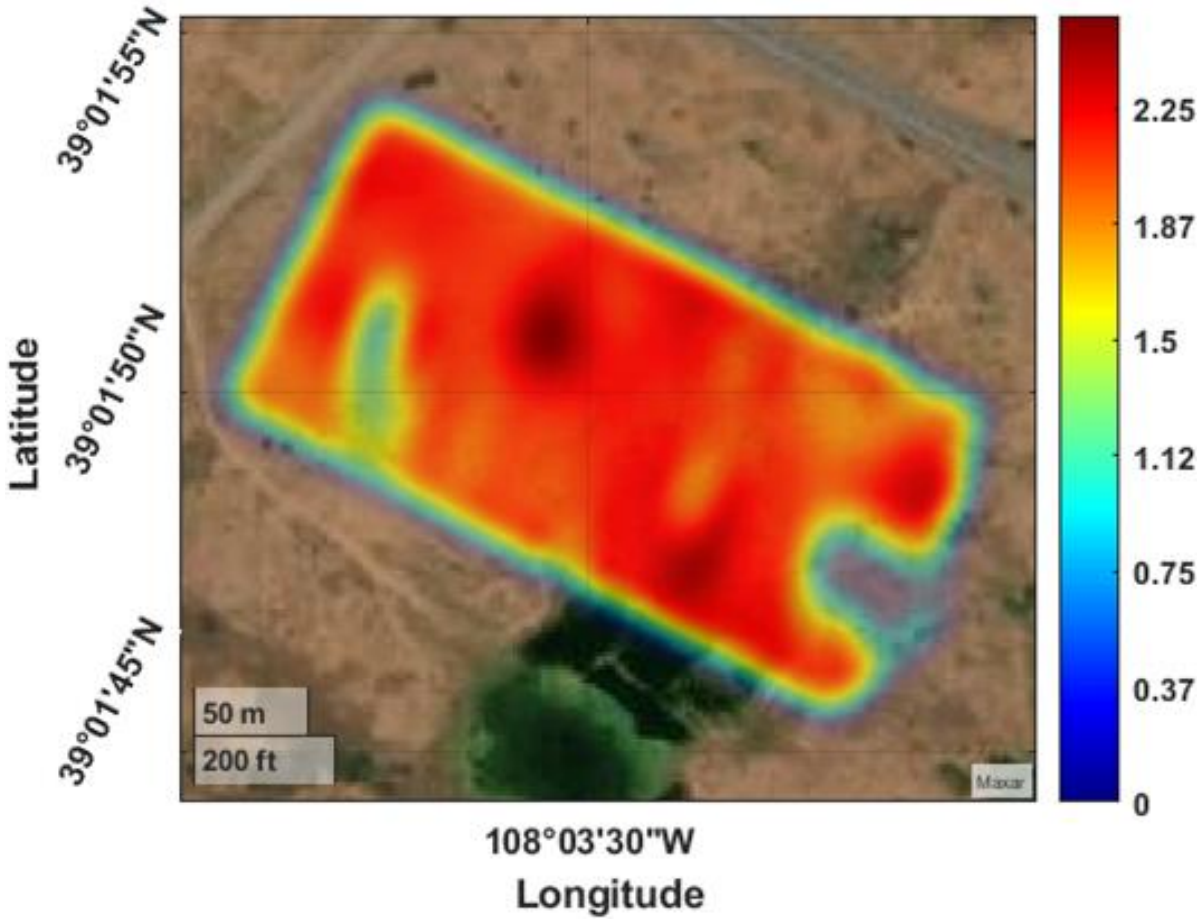

Figure. 5.13 Snow depth map from Colorado 2022 deployment.

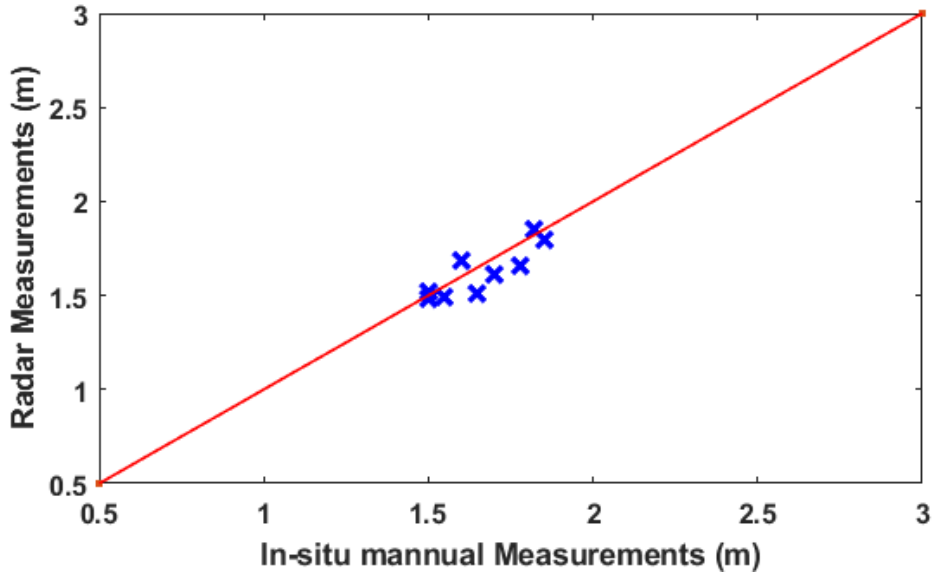

Figure. 5.14 Radar measurements with in-situ manual measurements from Colorado 2022 deployment.

5.3 Snow Measurements Deployment 2023

The miniaturized radar system (second prototype) with 1.5 kg weight was deployed over Colorado Grand Mesa during Feb-2023. The radar is configured with 4 GHz bandwidth from 2.2-6.2 GHz and supported by the CVA array reported in Chapter 3. However, the antenna design was modified to start the lower frequency from 2.2 GHz instead of 2.77 GHz.

Fig. 5.15 shows the radar test in the field. The test was performed over an area that was very close to the 2022 deployment. The weather condition was suitable for a UAV flight during the period Feb-1st to Feb- 4th. The wind speed was relatively constant between 1-5 m/s. The radar echogram from this deployment is shown in Fig. 5.16. The snow tracker is applied on this flight line to estimate the snow depth as shown in Fig. 5.17.

Figure. 5.15 Radar field deployment in Colorado 2023.

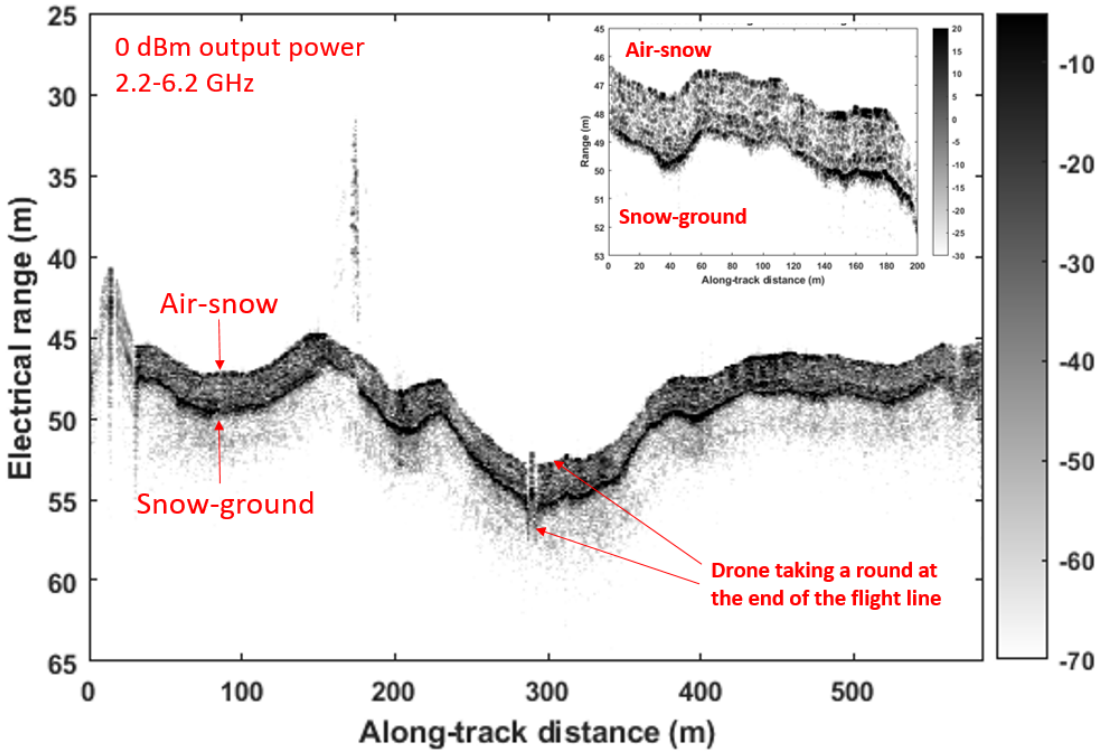

Figure. 5.16 A full flight line of 600 m length over the snow cover in 2023.

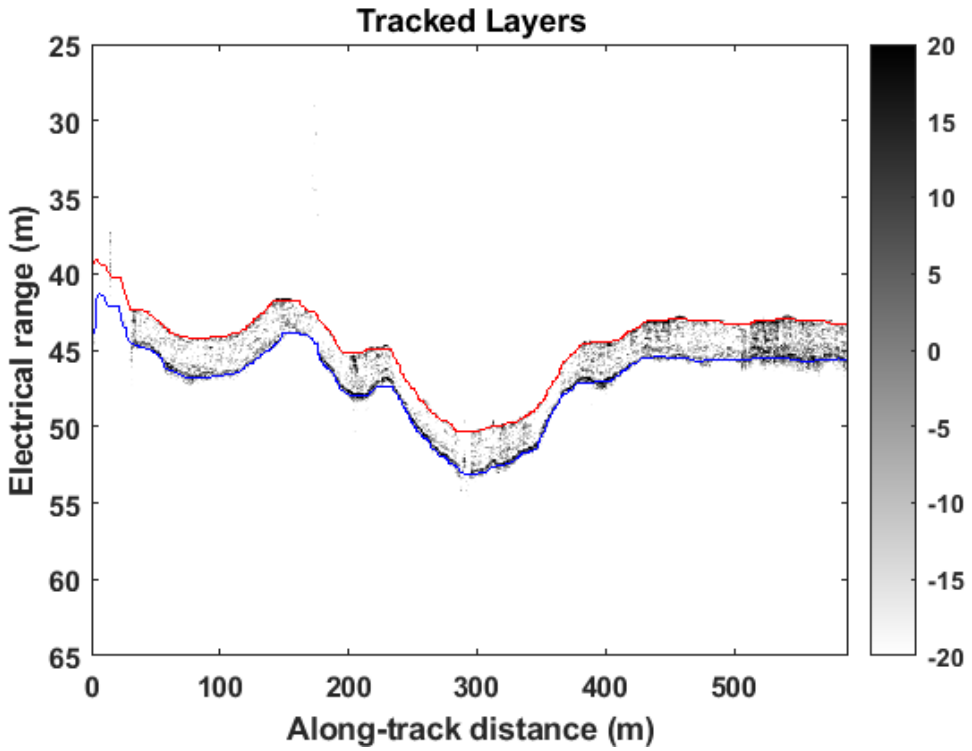

Figure. 5.17 Auto snow interfaces tracker applied on 2023 radar data.

In this deployment, 5 parallel flights were performed to cover an area of 270×300 m^2 as shown in Fig. 5.18. The spacing between the line was set to be 30 m and the UAV height was 55 m. The radar used the 4 GHz bandwidth signal with 0 dBm transmit power to generate this map. The result snow map shows a snow depth variation between 1-2.2 m in the area as shown in Fig. 5.19. The in-situ measurement team found that the snow dielectric constant was about 1.6 in the test area and this value was used to correct the electrical range in the radar measurement.

For the next deployment, a hybrid engine UAV may be used to extend the flight time furthermore to scan a larger area. The radar is capable to operate for about 60 minutes with its own batteries. Thus, a UAV with extended flight range will provide a wide range of test flights using the current radar systems.

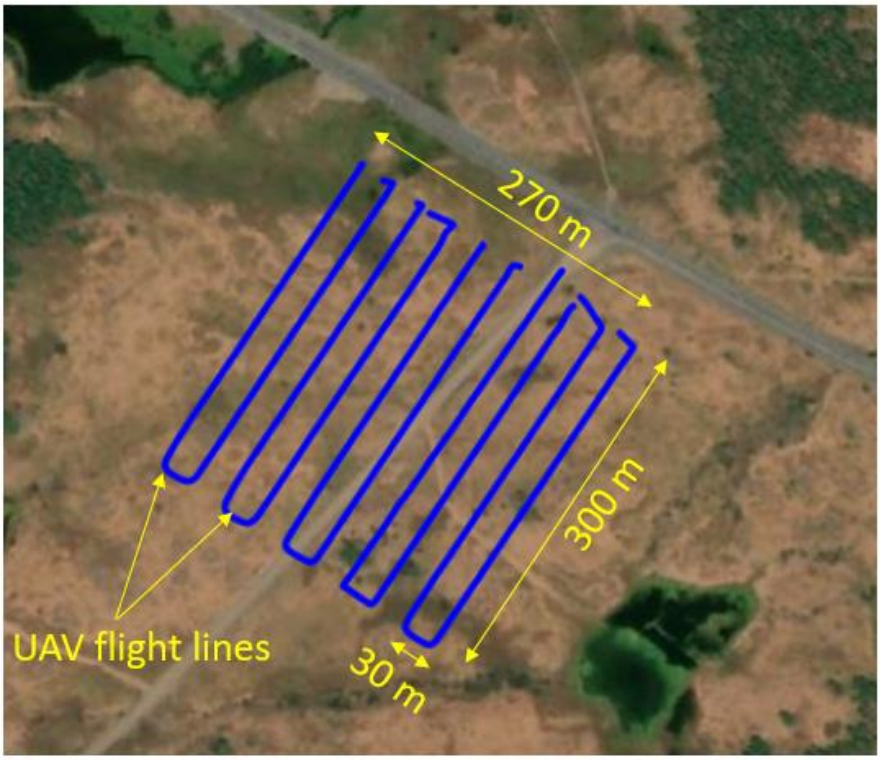

Figure. 5.18 UAV flight grid pattern at 2023 deployment.

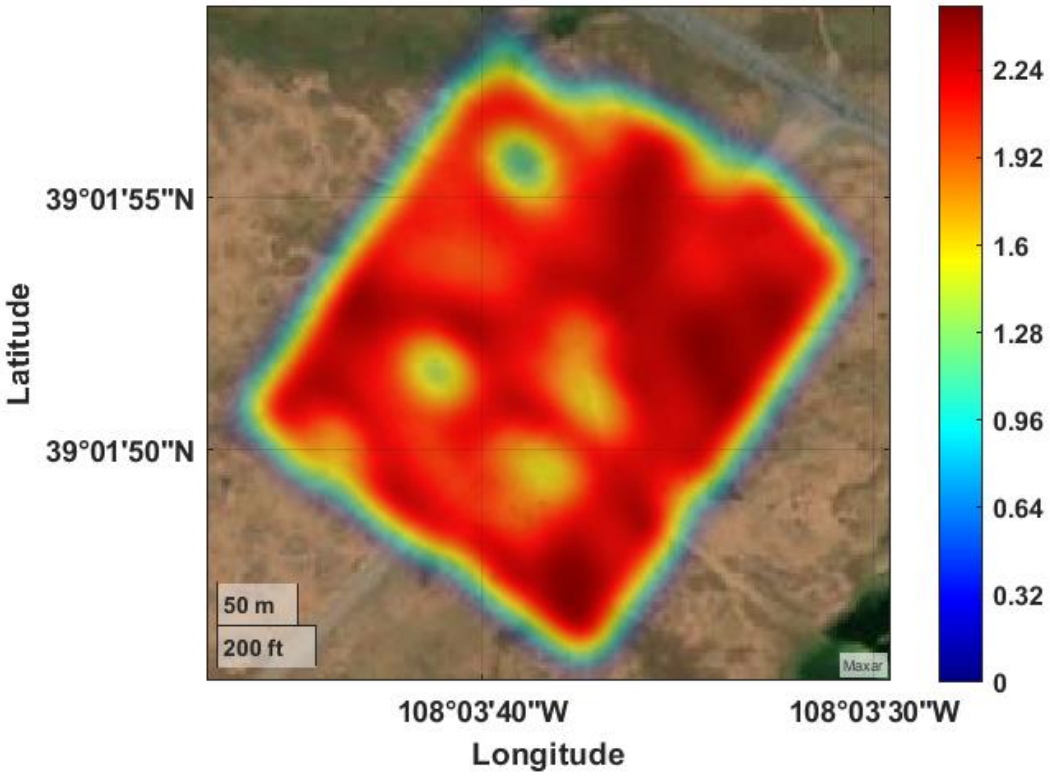

Figure. 5.19 Snow map from 2023 deployment.

CHAPTER 6

CONCLUSION AND SUMMARY

This chapter provides a summary of the dissertation's major accomplishments: (1) the development of two compact UWB radars using an automotive radar evaluation board; (2) the design of compact and lightweight UWB antenna arrays for use on small UAVs; (3) results from field tests; and (4) future research directions.

6.1 UWB Radars

Small UAVs equipped with ultra-wideband (UWB) radars have a great potential for fine-scale remote sensing of snow, soil moisture, sea and land ice, vegetation, coastal regions, and other targets. One of the major requirements for radars and other sensors for use in small UAVs is their lightweight and compact size. Radars using Monolithic Microwave Integrated Circuits (MMICs) can be developed. The cost of MMIC radars will require enormous resources, which are not available at typical university research institutions involved in remote sensing research. However, the industry has spent a lot of resources to develop mm-wave radar chips for automotive applications over the last few years. A novel approach to building a compact, lightweight FMCW radar for remote sensing applications is demonstrated by taking advantage of Commercial-Off-The-Shelf (COTS) mm-wave radar chips.

As a part of this dissertation, UWB radars using mm-wave automotive RF sensor evaluation boards are developed. Two down-converters are developed and used to down-convert 77-81 GHz mm-wave FMCW radars transmit signal into 2-6 GHz range. One of the down-converters is developed using waveguide components and the other uses mm-chips. The received

FMCW signal in the 2-6 GHz range is up-converted into the mm-wave range for processing and digitization. The first prototype is developed using waveguide and connectorized components. The weight of the first prototype was 5.5 lb. A more compact and lightweight second prototype with a larger operating bandwidth is developed using mm-wave chips and has 3.3 lb. weight. A PCB capable of operating in the mm-wave range with mixers and power divider was successfully designed and fabricated. This board is wire bonded to the mm-wave radar evaluation board. The radars are tested at different altitudes from 55 to 100 m on the UAV with output power as low as 0 dBm.

6.2 UWB Antenna Arrays

Different novel antennas were simulated, fabricated, and tested to support the UAV and manned aircraft radars in the field. The (8×8) DRA array achieved 50% impedance bandwidth with a gain value as high as 22 dBi. Another linear DRA array with 8-element was designed and installed on the UAV with 83% bandwidth. In addition, Vivaldi array achieved a wide bandwidth up to 132% with as high as 25 dBi gain while keeping a lightweight of 200 gm. The antennas achieved the major requirements of the radars link budget, the UAV total payload, and showed very good performance in the field.

6.3 Field Test Results

The two UWB radars including the antenna arrays were integrated into small UAVs. The initial test flights were conducted over a field site in Tuscaloosa, Alabama. The site was selected to contain small grass covered soils, tall trees, and a small lake. The radar was flown in a grid pattern to collect data over several flight lines during the summer of 2021.

The results from these flights demonstrated that the UWB radar with transmit power of about 10 mW can be used to collect calibrated backscatter data with fine resolution to obtain information on soil moisture, vegetation, and water levels.

Two more field tests were conducted to evaluate UWB radars performance over snow on Grand Mesa, Colorado during 2022-2023 field seasons. The radar data were collected in conjunction with detailed in-situ measurements that included snow thickness, snow density, and internal layers. Signal and data processing algorithms to correct for the system amplitude and phase non-linearity were modified and applied to obtain close to ideal point target responses. Also, a SAR processor developed for UWB FMCW radars was modified and applied to data collected to generate SAR images to generate snow thickness estimates.

The results over snow showed that very low-power UWB FMCW radar with transmit power as low as 1 mW can map snow-air and snow-land interfaces with SNR ratio of more than 25 dB. The SAR images used to estimate snow thickness and generate snow thickness maps for areas flown by the UAV. The snow thickness estimates obtained from radar data were within $\pm$ 10 cm of the in-situ measurements.

6.4 Publications List

This section summarizes the first author's publications published during the enrollment in the Ph.D. program at the University of Alabama.

6.4.1 Journal Publications

1. F. Abushakra *et al*., "Snow Depth Measurements with Ultra-Wideband Compact FMCW Radar on a small Unmanned Aircraft System," in *IEEE Journal of Radio Frequency Identification*, doi: 10.1109/JRFID.2023.3259240.
2. Feras Abushakra et al. "Ultra-wideband Coplanar Vivaldi Antenna Array with Dielectric Patch Antenna for Grating Lobes Suppression" *in IEEE Access*, vol. 10, 2022, doi: 10.1109/ACCESS.2022.3175840.

3. Feras Abushakra et al. “A Miniaturized Ultra-Wideband Radar for UAV Remote Sensing Applications” *in IEEE Microwave and Wireless Components Letters (MWCL)*, vol. 32, no. 3, pp. 198-201, March 2022, doi: 10.1109/LMWC.2021.3129153.
4. Feras Abushakra, A. Al-Zoubi, I. Al-Hmoud, T. Walpita, and N. Jeong, "Wideband and High-Efficiency 64-Element RDRA Array for Radar Applications," *in IEEE Open Journal of Antennas and Propagation (OJAP)*, vol. 2, pp. 932-936, 2021.
5. Feras Abushakra and Nathan Jeong, "Frequency Band Rejection Technique Based On the Operating Modes For a Wideband H-Shaped DRA", *Applied Computational Electromagnetics Society Journal (ACES)*, vol. 36, no. 2, pp. 168-173, 2021.
6. Feras Z. Abushakra, Asem S. Al-Zoubi, Ismail Uluer, and Derar F. Hawatmeh, "Ultra-Wideband E-shaped Dielectric Resonator Antennas Fed by Coaxial Probe and Trapezoidal Conductor", *International Journal of Electronics Letters*, vol. 9, no. 2. pp. 246-255, 2020.

6.4.2 Patents

1. Feras Abushakra, Omar Asfar, and Nathan Jeong "Miniaturized Reflector Antenna", US Patent, No. 20220352639, Nov. 2022.

6.4.3 Conference Publications

1. F. Abushakra *et al*., "Ultra-Wideband Ceramic-Based Dielectric Resonator Antenna Array For Radar Applications," *2022 International Workshop on Antenna Technology (iWAT)*, 2022, pp. 161-163, doi: 10.1109/iWAT54881.2022.9811038.
2. F. Abushakra and Prasad Gogineni "Drone-Based FMCW Radar For Remote Sensing Applications," *IEEE International Conference on Wireless for Space and Extreme Environments (WiSEE 2022)*, Winnipeg, Canada, 2022.

6.5 Future Works

The use of automotive radar chips to develop UWB radars for use on UAVs for remote sensing is demonstrated as a part of this dissertation. There are further opportunities for innovative applied research exploiting the full capability of the radar chips.

1. One of the areas for future research is to make the frequency range of operation, center frequency, and bandwidth selectable based on the measurement requirements and operational constraints. For example, for soil moisture measurements, the frequency range of operation over 1-5 GHz is much more desirable to match existing and future satellite missions' frequencies in L (1.25 GHz), S (3.2 GHz) and C (5.3 GHz) bands.

   Radars operating at much lower frequencies in VHF and UHF are needed for soil-water content and sea-ice measurements. These can be accomplished by making PLO frequency selectable, and up- and down-converter filters tunable or easily replaceable.

2. Polarimetric radars will provide much more useful information on vegetation and bio-mass. Polarimetric UWB radars can be developed by exploiting MIMO capability of automotive radar chips and developing dual-polarized transmit and receive antenna arrays. Most of automotive radar chips contain a minimum of two transmitter and four receiver channels to synthesize a large virtual cross-track array.

   One of the transmitters can be connected to a V-polarized antenna array and the other to an H-polarized antenna array. One of the receivers can be connected to a V-polarized receive antenna array and the other to an H-polarized receive array. As shown in table 6.1, polarimetric data can be collected on alternate chirps.

Table 6.1 polarimetric radar data.

Chirp #	Transmit Polarization	Receive Polarization
1	V	VV, VH
2	H	HH, HV

3. As a part of the dissertation, use of mm-wave chips to develop an up-down converters is demonstrated. There is an opportunity to further miniaturize and develop more advanced UWB radar for remote sensing. MM-wave amplifier and mixer chips are available to further miniaturize and develop a fully integrated system that weighs only 2 lbs or less.
4. Generate a soil moisture map similar to what we have done for the snow map.
5. Perform more experiments on the bi-static UAVs measurement over snow.
6. Operate the radars on a hybrid engine UAV to extend the flight time up to two hours to scan wide areas.
7. Gimballed antenna mount on a UAV to point the antenna beam at nadir because mapping snow-air, snow-land, and internal layers depends on coherent returns from these interfaces. These returns fall-off very rapidly with the incidence angle.

REFERENCES

[1] T. Oki, S. Kanae, "Global hydrological cycles and world water resources". *Science*, vol. 313, issue 5790, pp. 1068-1072, 2006.

[2] D. Pimentel, "Soil Erosion: A Food and Environmental Threat, " *Environ Dev Sustain*, vol. 8, pp. 119–137, 2006.

[3] R. Lal, "Water management in various crop production systems related to soil tillage," *Soil and Tillage Research*, vol. 30, Issues 2–4, pp. 169-185, 1994.

[4] Somers, LD, McKenzie, JM. , "A review of groundwater in high mountain environments ", *WIREs Water*. 2020; 7:e1475. doi.org/10.1002/wat2.1475

[5] C. N. Koyama, H. Liu, K. Takahashi, M. Shimada, M. Watanabe, T. Khuut, and M. Sato, "In-Situ Measurement of Soil Permittivity at Various Depths for the Calibration and Validation of Low-Frequency SAR Soil Moisture Models by Using GPR, " *Remote Sensing*, vol. 9, no. 6, pp. 580, 2017.

[6] A. Tan, K. Eccleston, I. Platt, I. Woodhead, W. Rack and J. McCulloch, "The design of a UAV mounted snow depth radar: Results of measurements on Antarctic sea ice," *2017 IEEE Conference on Antenna Measurements & Applications (CAMA)*, 2017, pp. 316-319, doi: 10.1109/CAMA.2017.8273437.

[7] Blom, John David. "*Unmanned Aerial Systems : a Historical Perspective / John David Blom.*" Fort Leavenworth, Kansas: Combat Studies Institute Press, US Army Combined Arms Center, 2010. Print.

[8] H. Shakhatreh *et al*., "Unmanned Aerial Vehicles (UAVs): A Survey on Civil Applications and Key Research Challenges," in *IEEE Access*, vol. 7, pp. 48572-48634, 2019, doi: 10.1109/ACCESS.2019.2909530.

[9] C. Xu, X. Liao, J. Tan, H. Ye and H. Lu, "Recent Research Progress of Unmanned Aerial Vehicle Regulation Policies and Technologies in Urban Low Altitude," in *IEEE Access*, vol. 8, pp. 74175-74194, 2020, doi: 10.1109/ACCESS.2020.2987622.

[10] T. Kelly. *The Booming Demand for Commercial Drone Pilots*. Accessed: Feb. 2022. [Online]. Available: https://www.theatlantic.com/ technology/archive/2017/01/drone-pilot-school/515022/

[11] FAA. Accessed: Feb. 2022. [Online], https://www.faa.gov/regulations_policies/faa_regulations/

[12] Airspace Designation and Standards, C.A.S.A., Canberra, AB, Australia, 1997.

[13] https://www.srs.fs.usda.gov/compass/2017/11/21/fia-update-on-alabamas-forests/, access April, 2023.

[14] *"Champion Trees of Alabama 2012"* . Alabama Forestry Commission. State of Alabama. 2013.

[15] Fawwaz Ulaby and David G. Long," *Microwave radar and radiometric Remote Sensing*," The University of Michigan Press, 2014.

[16] https://www.ti.com/product/AWR1843

[17] https://www.minicircuits.com/WebStore/imagevk_74.html

[18] A. E. -C. Tan, J. McCulloch, W. Rack, I. Platt and I. Woodhead, "Radar Measurements of Snow Depth Over Sea Ice on an Unmanned Aerial Vehicle," *IEEE Transactions on Geoscience and Remote Sensing*, vol. 59, no. 3, pp. 1868-1875, 2021.

[19] R. O. R. Jenssen, M. Eckerstorfer and S. Jacobsen, "Drone-Mounted Ultrawideband Radar for Retrieval of Snowpack Properties," *IEEE Transactions on Instrumentation and Measurement*, vol. 69, no. 1, pp. 221-230, 2020.

[20] R. O. R. Jenssen and S. K. Jacobsen, "Measurement of Snow Water Equivalent Using Drone-Mounted Ultra-Wide-Band Radar," *Remote Sensing*, vol. 13, no. 13, p. 2610, Jul. 2021.

[21] Kaijun Wu et al. "A new drone-borne GPR for soil moisture mapping," *Remote Sensing of Environment*, vol. 235, 2019.

[22] C. Noviello, G. Esposito, G. Fasano, A. Renga, F. Soldovieri, and I. Catapano, "Small-UAV Radar Imaging System Performance with GPS and CDGPS Based Motion Compensation," *Remote Sensing*, vol. 12, no. 20, p. 3463, 2020.

[23] M. Lort, A. Aguasca, C. López-Martínez and T. M. Marín, "Initial Evaluation of SAR Capabilities in UAV Multicopter Platforms," *IEEE Journal of Selected Topics in Applied Earth Observations and Remote Sensing*, vol. 11, no. 1, pp. 127-140, 2018.

[24] S. Prager, G. Sexstone, D. McGrath, J. Fulton and M. Moghaddam, "Snow Depth Retrieval With an Autonomous UAV-Mounted Software-Defined Radar," in *IEEE Transactions on Geoscience and Remote Sensing*, vol. 60, pp. 1-16, 2022, Art no. 5104816, doi: 10.1109/TGRS.2021.3117509.

[25] C. D. Simpson *et al.*, "Development of A UAS-Based Ultra-Wideband Radar for Fine-Resolution Soil Moisture Measurements," *2021 IEEE Radar Conference (RadarConf21)*, pp. 1-4, 2021.

[26] L. Wallace, A. Lucieer, C. Watson, and D. Turner, "Development of a UAV-LiDAR System with Application to Forest Inventory, " *Remote Sensing*, vol. 4, no. 6, pp. 1519–1543, May 2012, doi: 10.3390/rs4061519.

[27] T. Fahey, A. Gardi and R. Sabatini, "Integration of a UAV-LIDAR System for Remote Sensing of CO2 concentrations in Smart Agriculture," *2021 IEEE/AIAA 40th Digital Avionics Systems Conference (DASC)*, 2021, pp. 1-8, doi: 10.1109/DASC52595.2021.9594474.

[28] B. Welp *et al.*, "Versatile Dual-Receiver 94-GHz FMCW Radar System With High Output Power and 26-GHz Tuning Range for High Distance Applications," *IEEE Transactions on Microwave Theory and Techniques*, vol. 68, no. 3, pp. 1195-1211, 2020.

[29] S. -Y. Jeon *et al.*, "W-Band MIMO FMCW Radar System With Simultaneous Transmission of Orthogonal Waveforms for High-Resolution Imaging," *IEEE Transactions on Microwave Theory and Techniques*, vol. 66, no. 11, pp. 5051-5064, 2018.

[30] V. Jain, F. Tzeng, L. Zhou and P. Heydari, "A Single-Chip Dual-Band 22–29-GHz/77–81-GHz BiCMOS Transceiver for Automotive Radars," *IEEE Journal of Solid-State Circuits*, vol. 44, no. 12, pp. 3469-3485, 2009.

[31] S. Kim *et al.*, "Multichannel W-Band SAR System on a Multirotor UAV Platform With Real-Time Data Transmission Capabilities," *IEEE Access*, vol. 8, pp. 144413-144431, 2020.

[32] S. Gupta, P. K. Rai, A. Kumar, P. K. Yalavarthy and L. R. Cenkeramaddi, "Target Classification by mmWave FMCW Radars Using Machine Learning on Range-Angle Images," *IEEE Sensors Journal*, vol. 21, no. 18, pp. 19993-20001, 2021.

[33] C. Waldschmidt, J. Hasch and W. Menzel, "Automotive Radar — From First Efforts to Future Systems," *IEEE Journal of Microwaves*, vol. 1, no. 1, pp. 135-148, 2021.

[34] Z. Tong, R. Renter and M. Fujimoto, "Fast chirp FMCW radar in automotive applications," *IET International Radar Conference 2015*, pp. 1-4, 2015.

[35] S. Gogineni et al., "An ultra-wideband radar for measurements of snow thickness over sea ice," *IGARSS 2003. 2003 IEEE International Geoscience and Remote Sensing Symposium. Proceedings (IEEE Cat. No.03CH37477)*, 2003, pp. 2802-2804 vol. 4, doi: 10.1109/IGARSS.2003.1294591.

[36] Kanagaratnam, P., T. Markus, V. Lytle, B. Heavey, P. Jansen, G. Prescott, and S. Gogineni, "Ultra-wideband radar measurements of thickness of snow over sea ice, " *IEEE Transactions on Geoscience and Remote Sensing*, vol. 45, no. 9, September 2007.

[37] Yan, J-B et al. "Airborne Measurements of Snow Thickness Using ultrawide-band frequency-modulated-continuous-wave radar, " *IEEE GeoScience and Remote Sensing Magazine*, pp. 57-76, June 2017.

[38] Prajoy Podder, Tanvir Zaman Khan, Mamdudul Haque Khan, and M. Muktadir Rahman, " Comparative Performance Analysis of Hamming, Hanning and Blackman Window", *International Journal of Computer Applications*, vol. 96, pp. 1-7, 2014.

[39] F. Abushakra *et al*., "A Miniaturized Ultra-Wideband Radar for UAV Remote Sensing Applications," in *IEEE Microwave and Wireless Components Letters*, vol. 32, no. 3, pp. 198-201, March 2022, doi: 10.1109/LMWC.2021.3129153.

[40] R. K. Moore, "*Ground echo*," in Radar Handbook, M. I. Skolnik, Ed. New York: McGraw-Hill, 1970.

[41] K. Jin, T. Lai, Y. Wang, G. Li, and Y. Zhao, "Coherent Integration for Radar High-Speed Maneuvering Target Based on Frequency-Domain Second-Order Phase Difference," *Electronics*, vol. 8, no. 3, p. 287, 2019.

[42] Constantine A. Balanis, "*Antenna Theory Analysis and Design*," John Wiley & Sons, 2005.

[43] Marek Dvorsky, Harihara S. Ganesh, and S. Sadhish Prabhu, "Design and Validation of an Antipodal Vivaldi Antenna with Additional Slots, "*International Journal of Antennas and Propagation*, 2019.

[44] Satish K Sharma, Sudhakar Rao , Lotfollah Shafai, "*Handbook of Reflector Antennas and Feed Systems Volume I: Theory and Design of Reflectors*," Artech House, 2013.

[45] Hubregt J. Visser "*Array and Phased Array Antenna Basics*," John Wiley & Sons Ltd, 2005

[46] Robert J. Mailloux "*Phased Array Antenna Handbook 2nd-edition*, "Artech House antennas and propagation library, 2005.

[47] Wonbin Hong, N. Behdad and K. Sarabandi, "Size reduction of cavity-backed slot antennas," in *IEEE Transactions on Antennas and Propagation*, vol. 54, no. 5, pp. 1461-1466, 2006.

[48] A. Petosa and A. Ittipiboon, "Dielectric Resonator Antennas: A Historical Review and the Current State of the Art," in *IEEE Antennas and Propagation Magazine*, vol. 52, no. 5, pp. 91-116, Oct. 2010, doi: 10.1109/MAP.2010.5687510.

[49] A. A. Kishk, "Dielectric resonator antenna, a candidate for radar applications," *Proceedings of the 2003 IEEE Radar Conference (Cat. No. 03CH37474)*, 2003, pp. 258-264, doi: 10.1109/NRC.2003.1203411.

[50] J. Eichenberger, E. Yetisir and N. Ghalichechian, "High-Gain Antipodal Vivaldi Antenna With Pseudoelement and Notched Tapered Slot Operating at (2.5 to 57) GHz," *IEEE Transactions on Antennas and Propagation*, vol. 67, no. 7, pp. 4357-4366, 2019.

[51] J. Bai, S. Shi and D. W. Prather, "Modified Compact Antipodal Vivaldi Antenna for 4–50-GHz UWB Application," *IEEE Transactions on Microwave Theory and Techniques*, vol. 59, no. 4, pp. 1051-1057, 2011.

[52] Feras Z. Abushakra, Asem S. Al-Zoubi and Derar F. Hawatmeh, "Design and measurements of rectangular dielectric resonator antenna linear arrays," *Applied Computational Electromagnetics Society journal (ACES)*, vol. 33, no. 4, pp. 380-387, 2018.

[53] M. R. Nikkhah, A. A. Kishk, and J. Rashed-Mohassel, "Wideband DRA array placed on array of slot windows," *IEEE Transactions on Antenna and Propagation*, vol. 63, issue. 12, pp. 5382-5390, 2015.

[54] S. Tang, X. Wang, W. Yang and J. Chen, "Wideband Low-Profile Dielectric Patch Antenna and Array With Anisotropic Property," *IEEE Transactions on Antennas and Propagation*, vol. 68, no. 5, pp. 4091-4096, 2020.

[55] HFSS: High Frequency Structure Simulator Based on the Finite Element Method, version 19.2, ANSYS Corporation.

[56] Petosa, A. 2007. *Dielectric resonator antenna handbook*. Norwood, MA, USA: Artech House.

[57] L. Vegni, A. Toscano and F. Bilotti, "Tapered stripline embedded in inhomogeneous media as microwave matching line," *IEEE Transactions on Microwave Theory and Techniques*, vol. 49, no. 5, pp. 970-978, 2001.

[58] S. R. Best, "The Significance of Ground-Plane Size and Antenna Location in Establishing the Performance of Ground-Plane-Dependent Antennas," *IEEE Antennas and Propagation Magazine*, vol. 51, no. 6, pp. 29-43, 2009.

[59] M. A. Islam and N. C. Karmakar, "An 8×8 mm-Wave LP ACMPA Array for a Long-Range mm-Wave Chipless RFID Tag-Sensor Reader," *IEEE Journal of Radio Frequency Identification*, vol. 5, no. 1, pp. 53-63, 2021.

[60] J.D.S. Langley, P.S. Hall and P. Newham, "Novel ultrawide-bandwidth Vivaldi antenna with low cross polarisation," *Electronics Letters*, vol. 29, no. 23, 1993.

[61] J. Zhang et al. , "A compact high-gain Vivaldi antenna with improved radiation characteristics", *Progress In Electromagnetic Research Letters*, vol. 68, pp. 127-133, 2017.

[62] Lei Sang, Xiangxiang Li, Tao Chen and Guoqiang Lv, "Analysis and design of tapered slot antenna with high gain for ultra-wideband based on optimisation of the metamaterial unit layout", *IET Microwaves, Antennas & Propagation*, 11, pp. 907–914, 2017.

[63] H. Cheng, H. Yang, Y. Li and Y. Chen, "A Compact Vivaldi Antenna With Artificial Material Lens and Sidelobe Suppressor for GPR Applications," *IEEE Access*, vol. 8, pp. 64056-64063, 2020.

[64] J. Puskely, J. Lacik, Z. Raida and H. Arthaber, "High-Gain Dielectric-Loaded Vivaldi Antenna for Ka-Band Applications," *IEEE Antennas and Wireless Propagation Letters*, vol. 15, pp. 2004-2007, 2016.

[65] I. T. Nassar and T. M. Weller, "A Novel Method for Improving Antipodal Vivaldi Antenna Performance," *IEEE Transactions on Antennas and Propagation*, vol. 63, no. 7, pp. 3321-3324, 2015.

[66] S. Zhu, H. Liu and P. Wen, "A New Method for Achieving Miniaturization and Gain Enhancement of Vivaldi Antenna Array Based on Anisotropic Metasurface," *IEEE Transactions on Antennas and Propagation*, vol. 67, no. 3, pp. 1952-1956, 2019.

[67] H. Liu, W. Yang, A. Zhang, S. Zhu, Z. Wang and T. Huang, "A Miniaturized Gain-Enhanced Antipodal Vivaldi Antenna and Its Array for 5G Communication Applications," *IEEE Access*, vol. 6, pp. 76282-76288, 2018.

[68] P. Fei, Y. Jiao, W. Hu and F. Zhang, "A Miniaturized Antipodal Vivaldi Antenna With Improved Radiation Characteristics," *IEEE Antennas and Wireless Propagation Letters*, vol. 10, pp. 127-130, 2011.

[69] A. M. De Oliveira, M. B. Perotoni, S. T. Kofuji and J. F. Justo, "A Palm Tree Antipodal Vivaldi Antenna With Exponential Slot Edge for Improved Radiation Pattern," *IEEE Antennas and Wireless Propagation Letters*, vol. 14, pp. 1334-1337, 2015.

[70] Y. Liu, W. Zhou, S. Yang, W. Li, P. Li and S. Yang, "A Novel Miniaturized Vivaldi Antenna Using Tapered Slot Edge With Resonant Cavity Structure for Ultrawideband Applications," in *IEEE Antennas and Wireless Propagation Letters*, vol. 15, pp. 1881-1884, 2016.

[71] M. Abbak, M. N. Akıncı, M. Çayören and İ. Akduman, "Experimental Microwave Imaging With a Novel Corrugated Vivaldi Antenna," *IEEE Transactions on Antennas and Propagation*, vol. 65, no. 6, pp. 3302-3307, 2017.

[72] Nurhayati, G. Hendrantoro, T. Fukusako and E. Setijadi, "Mutual Coupling Reduction for a UWB Coplanar Vivaldi Array by a Truncated and Corrugated Slot," *IEEE Antennas and Wireless Propagation Letters*, vol. 17, no. 12, pp. 2284-2288, 2018.

[73] S. Zhu, H. Liu, Z. Chen and P. Wen, "A Compact Gain-Enhanced Vivaldi Antenna Array With Suppressed Mutual Coupling for 5G mm Wave Application," *IEEE Antennas and Wireless Propagation Letters*, vol. 17, no. 5, pp. 776-779, 2018.

[74] Krishna Kota and Lotfollah Shafai, "Gain and radiation pattern enhancement of balanced antipodal Vivaldi antenna," *Electronics Letters*, vol. 47, no. 5, 2011.

[75] A. Molaei and Mohsen Kaboli and S. A. Mirtaheri and M. S. Abrishamian "Dielectric lens balanced antipodal Vivaldi antenna with low cross-polarisation for ultra-wideband applications," *IET Microwaves Antennas & Propagation*, vol. 8, pp. 1137-1142, 2014.

[76] M. Moosazadeh and S. Kharkovsky and J. Case, "Microwave and millimetre wave antipodal Vivaldi antenna with trapezoid-shaped dielectric lens for imaging of construction materials," *IET Microwaves Antennas & Propagation*, vol. 10, pp. 301-309, 2016.

[77] J. Bourqui, M. Okoniewski and E. C. Fear, "Balanced Antipodal Vivaldi Antenna With Dielectric Director for Near-Field Microwave Imaging," *IEEE Transactions on Antennas and Propagation*, vol. 58, no. 7, pp. 2318-2326, 2010.

[78] Lei Juan and F. Guang and Y. Lin and F. Demin, "A modified balanced antipodal Vivaldi antenna with improved radiation characteristics," *Microwave and Optical Technology Letters*, vol. 55, pp. 1321-1325, 2013.

[79] M. Amiri, F. Tofigh, A. Ghafoorzadeh-Yazdi and M. Abolhasan, "Exponential Antipodal Vivaldi Antenna With Exponential Dielectric Lens," *IEEE Antennas and Wireless Propagation Letters*, vol. 16, pp. 1792-1795, 2017.

[80] Denghui Huang and Hu Yang and Yuqing Wu and Fei Zhao and Xiang Liu, "A high-gain antipodal Vivaldi antenna with multi-layer planar dielectric lens," *Journal of Electromagnetic Waves and Applications*, vol. 32, no. 4, pp. 403-412, 2018.

[81] M. Moosazadeh, "High-Gain Antipodal Vivaldi Antenna Surrounded by Dielectric for Wideband Applications," *IEEE Transactions on Antennas and Propagation*, vol. 66, no. 8, pp. 4349-4352, 2018.

[82] L. Sang, S. Wu, G. Liu, J. Wang and W. Huang, "High-Gain UWB Vivaldi Antenna Loaded With Reconfigurable 3-D Phase Adjusting Unit Lens," *IEEE Antennas and Wireless Propagation Letters*, vol. 19, no. 2, pp. 322-326, 2020.

[83] R. Cicchetti, V. Cicchetti, A. Faraone and O. Testa, "A Class of Lightweight Spherical-Axicon Dielectric Lenses for High Gain Wideband Antennas," *IEEE Access*, vol. 9, pp. 151873-151887, 2021.

[84] H. W. Lai, K. Luk and K. W. Leung, "Dense Dielectric Patch Antenna—A New Kind of Low-Profile Antenna Element for Wireless Communications," *IEEE Transactions on Antennas and Propagation*, vol. 61, no. 8, pp. 4239-4245, Aug. 2013.

[85] X. Wang, S. Tang, X. Shi and J. Chen, "A Low-Profile Filtering Antenna Using Slotted Dense Dielectric Patch," *IEEE Antennas and Wireless Propagation Letters*, vol. 18, no. 3, pp. 502-506, March 2019.

[86] F. Rodriguez-Morales *et al*., "An Improved UWB Microwave Radar for Very Long-Range Measurements of Snow Cover," in *IEEE Transactions on Instrumentation and Measurement*, vol. 69, no. 10, pp. 7761-7772, Oct. 2020, doi: 10.1109/TIM.2020.2982813.

[87] M. Moosazadeh and S. Kharkovsky, "A Compact High-Gain and Front-to-Back Ratio Elliptically Tapered Antipodal Vivaldi Antenna With Trapezoid-Shaped Dielectric Lens," *IEEE Antennas and Wireless Propagation Letters*, vol. 15, pp. 552-555, 2016.

[88] Yunqiang Yang, Y. Wang, and Aly Fathy, "Design of Compact Vivaldi Antenna Arrays for UWB See through Wall Applications," *Progress In Electromagnetics Research*, vol. 82, pp. 401-418, 2008.

[89] Denidni, T. A., & Weng, Z., "Rectangular dielectric resonator antenna for ultra-wideband applications," *Electronics Letters*, vol. 45, no. 24, pp. 1210–1212, 2009.

[90] M. Chiappe and G. L. Gragnani, "Vivaldi Antennas for Microwave Imaging: Theoretical Analysis and Design Considerations," *IEEE Transactions on Instrumentation and Measurement*, vol. 55, no. 6, pp. 1885-1891, 2006.

[91] J. T. Logan, R. W. Kindt and M. N. Vouvakis, "Low Cross-Polarization Vivaldi Arrays," *IEEE Transactions on Antennas and Propagation*, vol. 66, no. 4, pp. 1827-1837, April 2018.

[92] T. Liu, H. Yang, Y. He and J. Lu, "A $TE_{01\delta}$ Mode Omnidirectional Dielectric Resonator Antenna Excited by a Special Configuration," *IEEE Transactions on Antennas and Propagation*, vol. 66, no. 12, pp. 7339-7341, 2018.

[93] B. R. Motlhabane and D. Gray, "TE-monopole radiation pattern DRA for UAVs," *2012 International Symposium on Antennas and Propagation (ISAP)*, pp. 499-502, 2012.

[94] W. Li, K. W. Leung and N. Yang, "Omnidirectional Dielectric Resonator Antenna With a Planar Feed for Circular Polarization Diversity Design," in *IEEE Transactions on Antennas and Propagation*, vol. 66, no. 3, pp. 1189-1197, March 2018.

[95] X. Liu, K. W. Leung and N. Yang, "Wideband Horizontally Polarized Omnidirectional Cylindrical Dielectric Resonator Antenna for Polarization-Reconfigurable Design," *IEEE Transactions on Antennas and Propagation, doi: 10.1109/TAP.2021.3076458.*

[96] Y. M. Pan, K. W. Leung and K. Lu, "Study of Resonant Modes in Rectangular Dielectric Resonator Antenna Based on Radar Cross Section," *IEEE Transactions on Antennas and Propagation*, vol. 67, no. 6, pp. 4200-4205, 2019.

[97] C. Liu, M. T. A. Qaseer and R. Zoughi, "Influence of Antenna Pattern on Synthetic Aperture Radar Resolution for NDE Applications," *IEEE Transactions on Instrumentation and Measurement*, vol. 70, pp. 1-11, 2021.

[98] M. A. Elmansouri, G. R. Friedrichs, L. B. Boskovic and D. S. Filipovic, "An X-through Ka-band Thinned All-Metal Vivaldi Phased Array," *IEEE Transactions on Antennas and Propagation*, doi: 10.1109/TAP.2021.3076680.

[99] R. W. Kindt and W. R. Pickles, "Ultra-wideband All-Metal Flared-Notch Array Radiator," *IEEE Transactions on Antennas and Propagation*, vol. 58, no. 11, pp. 3568-3575, 2010.

[100] J. Yan, S. Gogineni, B. Camps-Raga and J. Brozena, "A Dual-Polarized 2–18 GHz Vivaldi Array for Airborne Radar Measurements of Snow," *IEEE Transactions on Antennas and Propagation*, vol. 64, no. 2, pp. 781-785, 2016.

[101] S. Zhu, H. Liu, P. Wen, Z. Chen and H. Xu, "Vivaldi Antenna Array Using Defected Ground Structure for Edge Effect Restraint and Back Radiation Suppression," *IEEE Antennas and Wireless Propagation Letters*, vol. 19, no. 1, pp. 84-88, 2020.

[102] S. Kolpuke *et al*., "Airborne UWB FMCW Radar for Snow Depth Measurements," in *IEEE Transactions on Geoscience and Remote Sensing*, vol. 60, pp. 1-15, 2022, Art no. 2008115, doi: 10.1109/TGRS.2022.3223989.

[103] Bajpai, Rakesh Kumar, et al. "Dual Band Microstrip Antennas for Wireless Applications," *International Journal of Advances in Applied Sciences (IJAAS)*, vol. 7, no. 2, pp. 143-151, 2018.

[104] **]** J. Liu *et al*., "A Low Profile, Dual-Band, Dual-Polarized Patch Antenna With Antenna-Filter Functions and Its Application in MIMO Systems," in *IEEE Access*, vol. 9, pp. 101164-101171, 2021, doi: 10.1109/ACCESS.2021.3096969.

[105] J. Hao, N. Yan, Y. Luo, H. Fu and K. Ma, "A Low-Cost Dual-Band Multimode High-Gain Stacked-Patch Antenna Based on SISL for 5G Applications," in *IEEE Antennas and Wireless Propagation Letters*, vol. 21, no. 1, pp. 4-8, Jan. 2022, doi: 10.1109/LAWP.2021.3112459.

[106] Y. Li, Z. Zhao, Z. Tang and Y. Yin, "Differentially Fed, Dual-Band Dual-Polarized Filtering Antenna With High Selectivity for 5G Sub-6 GHz Base Station Applications," in *IEEE Transactions on Antennas and Propagation*, vol. 68, no. 4, pp. 3231-3236, April 2020, doi: 10.1109/TAP.2019.2957720.

[107] C. D. Bui, N. Nguyen-Trong and T. K. Nguyen, "A Planar Dual-Band and Dual-Sense Circularly Polarized Microstrip Patch Leaky-Wave Antenna," in *IEEE Antennas and Wireless Propagation Letters*, vol. 19, no. 12, pp. 2162-2166, Dec. 2020, doi: 10.1109/LAWP.2020.3026067.

[108] Hsiao, H.-M., Wu, J.-W., Wang, Y.-D., Lu, J.-H. and Chang, S.-H. (2005), Novel dual-broadband rectangular-slot antenna for 2.4/5-GHz wireless communication. Microw. *Opt. Technol. Lett*., vol. 46, pp. 197-201. https://doi.org/10.1002/mop.20944

[109] M. H. Sharaf, A. I. Zaki, R. K. Hamad, and M. M. M. Omar, "A Novel Dual-Band (38/60 GHz) Patch Antenna for 5G Mobile Handsets, " *Sensors*, vol. 20, no. 9, p. 2541, Apr. 2020, doi: 10.3390/s20092541.

[110] Z. Luo, T. Su and K. -D. Xu, "A Single-Layer Low-Profile Dual-Wideband Monopolar Patch Antenna With Shorting Vias and Parasitic Annular Sectors," in *IEEE Antennas and Wireless Propagation Letters*, vol. 22, no. 2, pp. 432-436, Feb. 2023, doi: 10.1109/LAWP.2022.3215210.

[111] A. Khaleghi, "Dual Band Meander Line Antenna for Wireless LAN Communication," in *IEEE Transactions on Antennas and Propagation*, vol. 55, no. 3, pp. 1004-1009, March 2007, doi: 10.1109/TAP.2007.891873.

[112] Christopher David Simpson, "Airborne Ultra-Wideband Microwave Radar for the Remote Sensing of Soil Moisture", Ph.D. Dissertation, 2022, https://ir.ua.edu/handle/123456789/9870

[113] F. Abushakra *et al*., "Snow Depth Measurements with Ultra-Wideband Compact FMCW Radar on a small Unmanned Aircraft System," in *IEEE Journal of Radio Frequency Identification*, doi: 10.1109/JRFID.2023.3259240.

[114] Richards, Mark A. *Fundamentals of Radar Signal Processing*. US: McGraw-Hill Professional, 2005.

[115] R. K. Raney, "The delay/Doppler radar altimeter," in *IEEE Transactions on Geoscience and Remote Sensing*, vol. 36, no. 5, pp. 1578-1588, Sept. 1998, doi: 10.1109/36.718861.

[116] A. Meta, P. Hoogeboom and L. P. Ligthart, "Signal Processing for FMCW SAR," in *IEEE Transactions on Geoscience and Remote Sensing*, vol. 45, no. 11, pp. 3519-3532, Nov. 2007, doi: 10.1109/TGRS.2007.906140.

[117] J. J. M. de Wit, A. Meta and P. Hoogeboom, "Modified range-Doppler processing for FM-CW synthetic aperture radar," in *IEEE Geoscience and Remote Sensing Letters*, vol. 3, no. 1, pp. 83-87, Jan. 2006, doi: 10.1109/LGRS.2005.856700.

[118] K. Peek, "Estimation and compensation of frequency sweep nonlinearity in FMCW radar," M.S. thesis, Dept. Elect. Eng., Math. Comput. Sci., Univ. Twente, Enschede, The Netherlands, 2011.

[119] A. Meta, P. Hoogeboom, and L. Ligthart, "Range non-linearities correction in FMCW SAR," *in Proc. IEEE Int. Symp. Geosci. Remote Sens*., Denver, CO, USA, Jul. 2006, pp. 403–406.

[120] M. Tiuri, A. Sihvola, E. Nyfors and M. Hallikaiken, "The complex dielectric constant of snow at microwave frequencies," in *IEEE Journal of Oceanic Engineering*, vol. 9, no. 5, pp. 377-382, December 1984, doi: 10.1109/JOE.1984.1145645.